
Looking
Forward with
minimally
invasive
ultrasound
Jovana Janjic

Looking Forward with Minimally Invasive Ultrasound

Jovana Janjic

Financial support for the publication of this thesis was provided by:
Erasmus Medical Center
Philips Research
Oldelft Ultrasound

Financial support by the Dutch Heart Foundation for the publication of this thesis is gratefully acknowledged.

ISBN/EAN: 978-94-028-0956-5

Published by Ipskamp Printing
Layout by Legatron Electronic Publishing
Cover design by Irma Rademaker, Front creative experts

Looking Forward with Minimally Invasive Ultrasound

Vooruitkijken met minimaal-invasief ultrageluid

Thesis

to obtain the degree of Doctor from the
Erasmus University Rotterdam
by command of the
rector magnificus

Prof.dr. H.A.P. Pols

and in accordance with the decision of the Doctorate Board.

The public defence shall be held on

Tuesday 12th of June 2018 at 11:30

by

Jovana Janjic

born in Banja Luka, Bosnia and Herzegovina

Erasmus University Rotterdam

DOCTORAL COMMITTEE

Promotors: Prof.dr.ir. A. F. W. van der Steen
Prof.dr.ir. N. de Jong

Other members: Dr.ir. S. Klein
Prof.dr. S. Cochran
Prof.dr. J. Dankelman

Co-promotor: Dr. G. van Soest

NWO | Applied and Engineering Sciences

This work is part of the research programme interactive Multi-Interventional Tools (iMIT) with project number 12710, which is (partly) financed by the Netherlands Organisation for Scientific Research (NWO/AES).

The research described in this thesis has been carried out at the Department of Biomedical Engineering, Thorax Center, Erasmus MC in Rotterdam.

In memory of my grandfather Drago Janjic
who thought me that learning is a lifestyle

CONTENTS

Chapter 1

Introduction

1.1 MINIMALLY INVASIVE PROCEDURES

Surgical procedures have evolved over the centuries with the first successful open heart surgery using a heart-lung machine in 1953 by John H. Gibbon [1]. Since then surgery has become safer and more effective thanks to the continuous development of medical instrumentation and improved medical knowledge. A great step towards safer interventions has been achieved with the introduction of minimally invasive procedures, where small incisions are used to access the inside of the human body. Narrow surgical instruments such as trocars, needles and catheters are then advanced to examine and treat internal tissues. In the first half of the twentieth century biopsies of cancerous tissues in different organs were accomplished using fine needles [2]. In the same period minimally invasive procedures for cataracts, spine, knee, hip and brain surgery were developed and laparoscopic surgeries on the gall bladder were successfully accomplished [3,4]. Towards the end of the twentieth century, angioplasty was implemented to treat atherosclerotic lesions in the human arteries [5]. Angioplasty employs a tiny catheter that is commonly inserted through the femoral or radial artery and advanced towards the stenosis. The lesion is then opened inflating a balloon and stents are deployed to maintain the artery open. Angioplasty started with Charles Dotter, who inadvertently advanced an angiography catheter through an iliac plaque in 1963 and with Andreas Grüntzig, who performed the first balloon angioplasty in 1974 and the first coronary catheterization in 1977 [6].

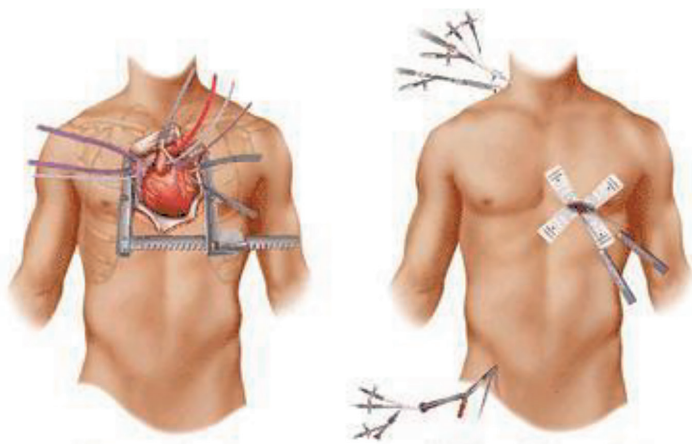

Figure 1.1 Artist's impression of open heart surgery (left) and minimally invasive techniques (right) for cardiac interventions requiring small incisions and less trauma. The image has been reproduced from: http://www.policymed.com

Beside the treatment of atherosclerosis, endovascular approaches have also been developed for other applications, such as cardiac valve replacement, treatment of congenital defects in the heart, catheter ablation to treat atrial fibrillation and the creation of shunts between the hepatic vein and the portal vein in the liver to treat portal hypertension (Transjugular intrahepatic portosystemic shunt or TIPS).

The wide spread of minimally invasive interventions in different medical fields demonstrates the success of this approach. With shorter recovery time and reduced patient trauma, minimally invasive procedures are the preferred treatment choice in many surgeries. Other advantages of minimally invasive procedures over open surgery are reduced risk of infection, shorter hospital stay, fewer complications, and less blood loss [7]. However, some disadvantages are also present, such as the need of specialized medical equipment and specialized training for the surgeons. The success of a minimally invasive procedure is highly dependent on the skills and experience of the surgeon in manipulating and guiding the devices towards the desired target. Certain minimally invasive procedures can take longer than the corresponding traditional open surgery. Therefore, there is a constant need to further improve minimally invasive techniques and develop new technologies to achieve better outcomes and shorten the procedure time.

An appropriate visual feedback regarding the location of the instrument in the body and the working field during minimally invasive procedures is fundamental for a successful intervention. Moreover, with appropriate image guidance, information on the effects of a specific interventions can be gained. In laparoscopic procedures, imaging of the inside of the abdomen is achieved with a video camera that is inserted through small incisions [4]. A related technique, named angioscopy, has been developed to investigate the inside of the coronary arteries [8], but clinical use remains limited due to practical limitations and the unclear added value. Angioscopy requires clearance of blood from the lumen using saline, employs large catheters that cannot reach distal vessels and cannot pass narrow areas. Moreover, angioscopy provides only surface imaging [9].

An imaging modality that is clinically employed in minimally invasive vascular procedures is angiography, an X-ray imaging technique that generates 2D projection images of the arterial lumen. Angiography shows vessel diameter, allowing an assessment of stenosis, but does not provide images of the vessel wall. Angiography is used as image guidance in percutaneous interventions of the coronary and peripheral arteries and to provide guidance during TIPS procedures. Overall, since imaging of the arteries is achieved from outside, angiography provides limited information on the vessel, the local working field, and often has limitations in visualizing interventional devices such as stents or balloon catheters which have limited radio-opacity.

A successful optics-based imaging technique that has been applied in intravascular applications is optical coherence tomography (OCT). OCT uses laser light to provides cross-sectional images of the arteries with a resolution of approx. 15 μm [10]. The high resolution and the possibility of integration into intravascular catheters, make OCT a very attractive technique. A limitation of OCT is the penetration depth, which is limited to 1–2 mm and does not allow to visualize the total thickness of the artery wall.

Ultrasound-based imaging modalities achieve better penetration depth than OCT, still retaining acceptable resolution. Ultrasound imaging is employed in many minimally invasive procedures and continuous research and investigations are performed to improve minimally invasive ultrasound in terms of device miniaturization, improved field of view and increased resolution and penetration depth.

1.2 ULTRASOUND FOR MINIMALLY INVASIVE PROCEDURES

Conventional ultrasound imaging employs a piezoelectric (PZT) transducer array and is based on transmitting high frequency sound waves (above 20 kHz). The small PZT elements of the array are the active part of the transducer. An electrical signal causes vibration of the elements, which then generate pressure waves that propagate through the medium and are reflected back from acoustic heterogeneities in the tissue. The reflected pressure waves that are received by the elements are then converted back in electrical signals and processed to generate an image based on the time of flight and the signal strength for different tissues. Most of the clinically available ultrasound scanners employ a linear transducer array and generate B-mode images of the underlying tissue. The image is formed by electronic switching, sweeping the ultrasound beam over the array elements [11]. The higher the frequency and the larger the bandwidth used in ultrasound imaging, the higher the resolution. However, due to the increased attenuation with increased frequency, there is always a compromise between the resolution and the penetration depth required for each specific application.

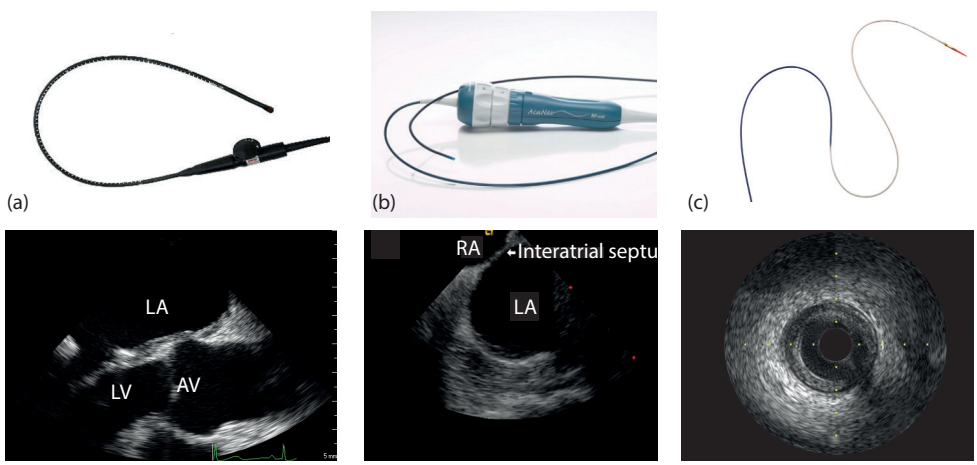

Figure 1.2 (a) TEE probe (Oldelft Ultrasound, Netherlands, 14 mm width), figure reproduced from http://www.oldelft.nl; (b) ICE catheter (Siemens AcuNav, 8-1-French), figure reproduced from http://www.kpiultrasound.com; (c) IVUS catheter (Philips Eagle Eye, 3 French), figure reproduced from https://www.usa.philips.com; (d) 2D TEE image (courtesy of Dr. C. Ren); (e) ICE image reproduced from earlier publication [12]; (f) IVUS image of a coronary artery (courtesy of E.M.J. Hartman). LA, left atrium; LV, left ventricle; AV, aortic valve; RA, right atrium.

Conventional non-invasive transthoracic echocardiography employs a transducer that is placed on the thorax and the ultrasound waves have to pass in between the ribs and the lungs before reaching the heart. Due to the quite long ultrasound travel distance, low frequencies (1–5 MHz) are usually the preferred choice. 2D Imaging of the heart from a closer distance can be achieved using transesophageal probes (TEE) that are placed in the esophagus, very close to the upper chambers of the heart. TEE has been successfully used during catheter ablation for atrial fibrillation [13] and treatment of atrial septal defects (ASD) [14].

Further developments led to the introduction of intracardiac echocardiography (ICE) [15,16], which is a catheter based technique that allows to advance the ultrasound transducer through the vasculature in the mid-right atrium. Conventional ICE catheters are one-dimensional arrays with a side-looking aperture, rendering imaging and interpretation of cardiac structures a task for experts. Moreover, the frequency used in ICE is approximately 7 MHz, close to the frequency used in TEE, hence limiting the imaging resolution [17].

A minimally invasive ultrasonic imaging technique that employs higher frequencies and is used to image the inside of the arteries, is intravascular ultrasound (IVUS). Coronary IVUS catheters (2.6–3.2 French) use frequencies in the range of 20–60 MHz and consist of either a single element mechanically rotated around the catheter axis or a circular array with the ultrasound beam electronically steered [15,18]. Both designs provide cross-sectional images of the arterial lumen, giving insights into atherosclerotic plaque morphology and aiding the treatment choice during coronary [19] and peripheral vasculature interventions. Since conventional IVUS provides side-looking imaging, it can only be used for lesions which are not highly stenotic and have a free lumen dimension compatible with IVUS catheters.

1.3 MINIATURIZED FORWARD-LOOKING 3D ULTRASOUND

Ultrasound imaging during minimally invasive procedures is mostly based on linear transducers that provide 2D images of 3D structures. Attempts have been made in the development of 2D matrix transducers that could be mounted on cardiac catheters to achieve volumetric imaging, but most of them are limited to side-looking approaches [20-22]. These design choices are primarily dictated by the limited dimensions of minimally invasive devices and the difficulties in integrating 2D matrix transducers at their tip.

To improve image guidance, miniaturized forward-looking (FL) transducers capable of generating 3D images of the tissue structures ahead of the device are required. This could be beneficial for applications such as monitoring during ASD corrections, valve replacement, TIPS, placement of stents, biopsy procedures and guidance during crossing of intravascular chronic total occlusions (CTO), which are atherosclerotic lesions that completely fill the vessel lumen and have a highly heterogeneous tissue composition, with variable mechanical properties [23].

First attempts in the development of forward-looking ultrasound imaging devices for minimally invasive procedures consisted of single-element transducers mounted at the tip of the catheter and mechanically scanned using wobbling and rotating mechanisms [24-28] making the whole assembly bulky and unstable. To avoid rotating mechanisms and achieve volumetric imaging, multi-element arrays have been investigated with each individual element directly connected to the external acquisition system [29-33]. Efforts towards reduction of coaxial cables have been taken by implementing integrated circuits with multiplexers to interface multiple PZT elements [34,35]. Moreover, a technology based on capacitive micromachined ultrasonic transducers (CMUT) has been explored, which allows fabrication of transducers with arbitrary geometry using standard micro-fabrication processes [36,37]. Employing this technology several forward-looking transducers providing 2D and 3D images have been investigated [38-44].

1.4 CHALLENGES IN MINIMALLY INVASIVE 3D FORWARD-LOOKING ULTRASOUND

Since intensive effort is ongoing in the development of 3D forward-looking ultrasound imaging for minimally invasive procedures, it is important to understand the associated challenges. These challenges can be separated in those related to hardware and technical implementations and those related to image formation.

1.4.1 Hardware challenges

The small dimensions of minimally invasive devices such as needles and catheters impose a major constraint on the effective aperture of the ultrasound transducer that can be mounted at the tip, limiting the total ultrasound dimensions to a few millimeters. Moreover, since minimally invasive devices can be placed very close to the imaging target, higher frequencies (>10 MHz) are preferred, which correspond to a very thin PZT layer (<150 μm). Beside the thickness, the materials and the overall geometry of the transducer array will affect the acoustic behavior. Fabrication of transducers that fulfill all the geometrical requirements and have small dimensions is not trivial and requires careful acoustic stack design to optimize the transducer performance. The same observation holds for CMUT transducers, which have an operating frequency inversely related to the radius of the capacitor.

Next to the acoustic optimization and the transducer stack fabrication, electrical interconnections pose additional challenges for the successful integration of miniaturized ultrasound transducers in catheter and needles. To achieve volumetric imaging ahead of the minimally invasive device without using bulky mechanisms, a 2D matrix transducer array should be considered. However, for these multi-element transducers, an electrical connection is required between each element and the external imaging system. which poses the problem of accommodating multiple cables in the device [29-33]. Many minimally invasive instruments are designed with a hollow lumen to allow insertion of additional instruments such as guidewires,

balloons and stents and sometimes they incorporate mechanical steering mechanisms to improve the device dexterity. This further reduces the available space that can be allocated for electrical cables. Integrated circuits have been developed in the effort of reducing the cable count [38-44], but careful circuit design and optimization is needed to interface all the elements.

An alternative approach could employ only a few elements, or even a single element, which sequentially scans the volume ahead of the catheter. Computational approaches are then needed to reconstruct a volumetric image from the acquired data. This method is similar to the circumferential scan in IVUS pullbacks, where serially acquired A-lines are spatially arranged to map out a volume. For forward-looking instruments, a transducer position tracking mechanism is required to make this work. The direct advantage of this concept is device simplicity, but image reconstruction is more complicated than with array sensors.

1.4.2 Imaging challenges

The constraints on the aperture size of the transducers that can be mounted at the tip of minimally invasive devices greatly limits the imaging capability. Optimally, to provide sufficient information over the working field, forward-looking ultrasound transducers should provide volumetric imaging with sufficient spatial coverage over the region of interest and with high resolution in all the dimensions. It is known that lateral image resolution depends on the transducer aperture [45]. A way to overcome the aperture limitation is to consider synthetic aperture techniques, where multiple acquisitions at different spatial locations are combined in an effectively wider aperture. Simple hand manipulation of minimally invasive devices could provide a mean to move the transducer over multiple spatial location. This could be achieved by mounting the transducer at the tip of steerable devices. However, to combine the different acquisitions, real time 3D spatial coordinates of the device tip should be recorded with an appropriate motion tracking system. Video and magnetic motion tracking systems have been investigated for 3D freehand ultrasound imaging using conventional linear arrays [46,47]. These systems are rather bulky and not easily scalable to the dimensions needed for minimally invasive approaches. A tracking technique that is showing great potential in the intravascular field is optical shape sensing (OSS) [48,49], which employs a thin optical fiber and a laser system to reconstruct the 3D coordinates of the device in which the fiber is inserted (see grey text box). This technique has been combined with preoperative CT imaging to provide a roadmap during peripheral vasculature interventions.

1.5 THESIS OUTLINE

In the effort of overcoming the previously described challenges, this thesis presents solutions for miniaturized 3D forward-looking ultrasound imaging suitable for minimally invasive interventions. The goal was to develop compact and smart systems that could provide

volumetric ultrasound imaging with high resolution and that could be integrated at the tip of interventional catheters.

This thesis focuses on mainly two approaches to achieve minimally invasive 3D forward-looking ultrasound imaging. In the effort of addressing the hardware challenges, the first approach consists in developing a 2D matrix piezoelectric transducer array with an optimized acoustic design and an appropriate interconnection scheme requiring a limited number of electrical cables (**Chapter 2** and **3**). The second approach consists in developing less complex ultrasound devices having only a single element transducer that is integrated in the device together with steering mechanisms and position tracking systems that are exploited to provide volumetric imaging ahead of the tip (**Chapters 4**, **5**, **6** and **8**).

Transducer geometry optimization is the focus of **Chapter 2** with a detailed analysis on the influence of subdicing on the radiation impedance, on the time and frequency response and on the directivity of high frequency linear array elements.

A miniaturized 2D matrix transducer with a front-end ASIC with reduced cable count, suitable for FL-IVUS imaging is presented in **Chapter 3**. Transducer design, fabrication and acoustic characterization are described and FL volumetric imaging is demonstrated.

FL imagining approaches based on single element transducers are investigated starting from **Chapter 4**. Here a novel tip design for minimally invasive steerable devices that accommodates a 14 MHz single element transducer and an OSS fiber is described. A prototype of the integrated device has been manufactured and, by combining ultrasound A-lines and OSS position information acquired while steering the tip device, feasibility of 3D FL reconstruction has been demonstrated on a phantom. To achieve FL volumetric imaging, a method to process the sparse information obtained by manually steering the catheter tip with the transducer element needs to be implemented. This has been achieved in **Chapter 5**, where a clinically available steerable intracardiac catheter has been modified to accommodate a 25 MHz single element transducer and the OSS fiber. An adaptive normalized convolution method has been implemented and successful sparse image reconstruction of the surface of a tissue-mimicking phantom and of a human *ex-vivo* carotid plaque have been achieved. These successful results have been extended to 3D image reconstructions using an innovative intracardiac steerable catheter in **Chapter 6**.

To improve the lateral image resolution achieved using a single element transducer, the spatial information of the ultrasound beam is exploited. A well-known phenomenon resulting from spatially structured ultrasound beam with phase variance is speckle. A theoretical overview of speckle in ultrasound is presented in **Chapter 7**, whereas **Chapter 8** introduces Structured Ultrasound Microscopy (SUM), a novel imaging technique that achieves wide-field, depth-independent microscopic resolution using a single element transducer and a coding mask

that scrambles the phase uniformity and allows volumetric image reconstruction by solving an inverse scattering problem.
Chapter 9 provides a discussion over the solutions presented for minimally invasive FL imaging together with a conclusion and future directions.

Optical Shape Sensing (OSS)

The optical shape sensing system that has been used in part of this thesis is a research prototype developed at Philips Research, Eindhoven, The Netherlands and it is based on the technology described in [48,49]. This system provides distributed sensing over a fiber and it could be beneficial for medical devices that are highly flexible, like catheters and guidewires.

The system consists of two major components: a multi-core optical fiber with an outer diameter of 200 μm and a scanning laser system. The fiber has one core running along the longitudinal axis and three cores located axially 120° apart from each other and arranged in a helical fashion around the central one. Fiber Bragg Gratings (FBG) are patterned into the cores along the entire length of the fiber (1.8 m) with a spacing of 50 μm. FBGs consist in periodic changes in refractive index that reflect a band of light with a wavelength that is related to the periodicity of the index variation. When the fiber is bent, stretching and compression induce local changes in the period of the FBG, hence varying the wavelength of the reflected light. It is through this mechanism that distributed strain measurements are obtained.

The Philips scanning laser system has a central wavelength set to 1545 nm and is swept over 17 nm. The laser system is used to interrogate the sensors along the fiber using an optical frequency domain reflectometry technique. The specific location of the FBG will result in a specific frequency modulation of the carrier signal received, hence enabling distributed measurements of the strain applied to each of the cores. By integrating along the fiber starting from the first sensing point (that is fixed in the reference frame) and considering that each sensing point consists of a triplet of values, the strain measurements can be processed to obtain the 3D shape of the fiber. Since the position of each sensing point is computed based on the previous one, the accuracy of the reconstruction is inversely proportional to the length considered.

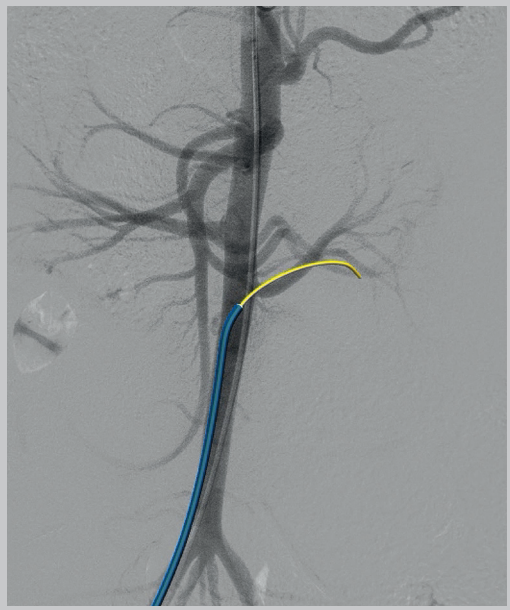

Figure 1.3 The picture shows an x-ray aortogram during a pre-clinical experiment, taken before navigating with shape sensed devices. In the aortagram contrast fluid is injected into the vessels to make the location of the vessels visible on x-ray. The contrast injection catheter is also clearly visible. This 2D roadmap of the vessels is registered with Philips shape sensed devices, and can be used to navigate the devices to a specific location without further use of x-ray. Yellow shows a guidewire, and blue shows a catheter. The devices are used for navigation inside the aorta, in this case to cannulate the left renal artery. Picture courtesy of Philips Research.

Chapter 2

Improving the Performance of a 1D Ultrasound Transducer Array by Subdicing

Based on:

Jovana Janjic, Maysam Shabanimotlagh, Martin D. Verweij, Gijs van Soest, Antonius F.W. van der Steen, Nico de Jong, Quantifying the effect of subdicing on element vibration in ultrasound transducers, *Proc. IEEE International Ultrasonics Symposium (IUS), Oct. 2015, pp 1-4.*

Jovana Janjic, Maysam Shabanimotlagh, Gijs van Soest, Antonius F.W. van der Steen, Nico de Jong, Martin D. Verweij, Improving the Performance of a 1-D Ultrasound Transducer Array by Subdicing, *IEEE Trans Ultrason Ferroelectr Freq Control. 2016 Aug; 63(8):1161-71.*

ABSTRACT

In medical ultrasound transducer design, the geometry of the individual elements is crucial since it affects the vibration mode of each element and its radiation impedance. For a fixed frequency, optimal vibration (i.e. uniform surface motion) can be achieved by designing elements with very small width-to-thickness ratios. However, for optimal radiation impedance (i.e. highest radiated power), the width should be as large as possible. This leads to a contradiction that can be solved by subdicing wide elements. To systematically examine the effect of subdicing on the performance of a 1D ultrasound transducer array, we applied finite-element simulations. We investigated the influence of subdicing on the radiation impedance, on the time and frequency response, and on the directivity of linear arrays with variable element widths. We also studied the effect of varying the depth of the subdicing cut. The results show that, for elements having a width greater than 0.6 times the wavelength, subdicing improves the performance compared to that of non-subdiced elements: the emitted pressure may be increased up to a factor of three, the ringing time may be reduced by up to 50%, the bandwidth increased by up to 77%, and the side lobes reduced by up to 13 dB. Moreover, this simulation study shows that all these improvements can already be achieved by subdicing the elements to a depth of 70% of the total element thickness. Thus subdicing can improve important transducer parameters and, therefore, help in achieving images with improved signal-to-noise ratio and improved resolution.

2.1 INTRODUCTION

Most of the clinically available ultrasound imaging probes are one-dimensional (1D) linear transducers. They consist of small piezoelectric (PZT) elements, which are the active components of the probe. An electrical excitation is used to induce vibration of the individual elements, which in turn generate pressure waves that propagate into the medium. The pressure waves reflected from different scatterers are subsequently received by the elements and converted back into electrical signals, which are processed in the ultrasound machines to yield echo images. To create images with high resolution and high signal-to-noise ratio, the geometry of the elements plays a crucial role in transducer design. This is because the geometry affects both the element vibration and the element radiation impedance.

Regarding the element vibration, it is known that if the width-to-thickness ratio is smaller than 0.7 [50], the element will mainly vibrate along the thickness direction. Knowing that the wavelength in PZT is almost twice the wavelength in water (λ), we can also say that thickness vibration is obtained when the width of the element is well below 0.7λ. Elements with a thickness vibration have a piston-like behavior; this behavior is considered optimal because all the surface points of the element, when excited, will have the same velocity amplitude and phase, which is favorable for the transmission efficiency.

The geometry also affects the radiation impedance, which describes the acoustic coupling of the vibrating element to the medium, and is usually defined for piston motion [51]. To obtain the highest radiated power, the radiation impedance should be real and equal to the acoustic impedance of the medium. For a wavelength λ and a circular element with diameter a, the complex radiation impedance is mainly imaginary for a<0.5λ [51,52]. This means that little or no energy is transmitted into the medium. Similar behavior is found for square elements with sides a and infinitely long strip elements with width a: the radiation resistance drops quickly when a assumes values below 0.7λ [53,54]. The strip geometry is representative of 1D ultrasound transducer arrays, where each element is many times longer than it is wide.

From what was stated in the previous paragraphs, it is clear that to design 1D transducer arrays with piston-like behavior, elements with very small widths are preferred. However, for optimal radiation impedance, the element should be as large as possible. This leads to a contradiction when trying to achieve both optimal vibration and optimal radiation impedance. The current approach is to consider elements having a width between 0.5λ and λ. This, however, might not be the optimal solution.

The geometrical requirements for optimal vibration and optimal radiation impedance are even more crucial for high frequency transducers. To better explain this, we can consider a linear array with center frequency of 15 MHz and wavelength λ=100 µm in water. If we assume a PZT speed of sound of approximately 3000 m/s, the element thickness has to be 100 µm. Therefore,

for optimal vibration and optimal radiation efficiency, the width of the element has to be about 70 μm. Such small dimensions, however, are difficult to achieve when manufacturing transducers, especially if we consider the difficulty of making electrical connections to these individual elements. A possible solution to this problem is to consider elements with a width greater than 0.7λ and perform subdicing.

Subdicing means cutting each transducer element in two or more sub-pillars while keeping the electrical connection between the elements intact [55]. Subdicing decreases the width-to-thickness ratio of the vibrating pillars and separates the lateral vibration from the thickness resonance [50,55-58]. The depth of the subdicing cut is also important, mainly because of fabrication issues; by partially subdicing the elements, damage of the electrodes can be prevented and mechanical stability can be ensured. To date, it seems that no systematic studies have been performed that quantitatively show the effect of subdicing in itself and the influence of the subdicing depth on the transducer performances. In our opinion, such systematic studies are important to further improve the efficiency of the transducer design process.

In this paper, we systematically present the effect of subdicing by showing Finite Element Analysis (FEA) simulations obtained with PZFlex software (Weidlinger Associates, Los Altos, CA). We focus on the performance of linear array elements with an operational frequency of approximately 14 MHz. We analyze the influence of subdicing on the radiation impedance, on the time and frequency response and on the directivity pattern. We also investigate the effect of the depth of the cut to understand if it is possible to partially subdice the elements and still achieve good transmission performance.

2.2 DEFINITION OF SIMULATION MODEL AND ROLE OF SUBDICING

In 1D arrays the length of the elements is much larger than the width and the thickness [59]. Therefore, in this paper the elements will be considered infinitely long, which reduces our simulations to two-dimensional (2D) problems.

The 2D simulation study is performed using the FEA software PZFlex, and the considered model is depicted in Figure 2.1. In this study, the thicknesses of all the layers are fixed, while the width of each of the elements is varied from 10 μm to 250 μm in steps of 10 μm. Only a portion of a realistic linear array is modeled, with a central active element and three neighboring passive elements on both sides. The space between the elements and in the subdicing cuts is approximately 8 μm wide and is taken to be void [60], while water is used as the medium in which the ultrasound is propagating. After subdicing, the width of the elements and the subdicing cuts may differ from the ideal values by at most ± 2 μm, i.e. one grid step, due to numerical rounding. To reduce the simulation time, we assume symmetry in the plane x=0. With this condition, only half of the model needs to be simulated. The domain is surrounded

by absorbing boundary conditions to avoid reflections from its edges. The thicknesses and material properties of each layer of the transducer are given in Table 2.1.

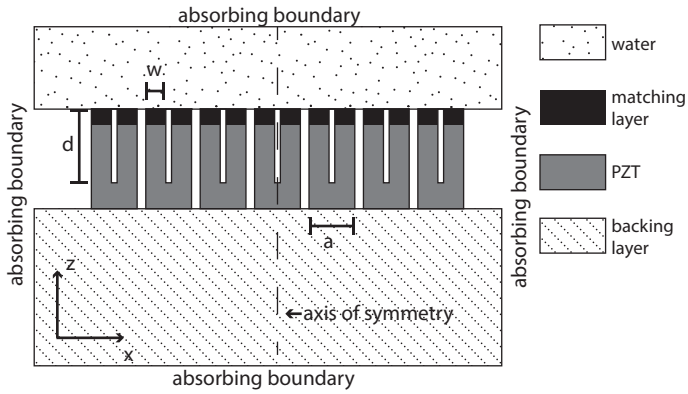

Figure 2.1 The 2D simulation model. Seven transducer elements are modeled and only the central element is electrically excited. The width of each of the elements is a, the width of the sub-pillars is w and the depth of the cuts is d.

Table 2.1 Thicknesses and Material Properties Used in the Simulations

Layer	Material	Thickness [μm]	Material Properties
PZT	Ceramic (PZT-5A)	100	ρ=7700 kg/m^3 c_{11}=147, c_{12}=105, c_{13}=93.7, c_{33}=113, c_{44}=23, c_{66}=21.2 MPa ε_{11}=10, ε_{33}=8.09x10^{-9} C/Vm e_{15}=11.64, e_{31}=-3.09, e_{33}=16 C/m^2
Matching	Conductive Epoxy	30	ρ=3350 kg/m^3, Z=6.7 MRayl c_{shear}=1050 m/s
Backing	Tungsten loaded epoxy	500	ρ=2975 kg/m^3, Z=5.8 MRayl c_{shear}=1960 m/s

To validate the PZFlex model, we have compared the simulation results for the radiation impedance and for the directivity to the analytical curves. Moreover, a numerical test has been performed with a twice denser numerical grid. The obtained results showed no significant differences with the results obtained for our standard grid. This ensures the numerical accuracy of our simulations.

The electrical impedance plot is the primary tool that we will employ to see whether an element has vibration modes with a non-uniform surface motion. To explain this, we show in Figure 2.2 and Figure 2.3 the electrical impedance versus frequency for elements in different situations. Figure 2.2 demonstrates how the electrical impedance plot for a narrow (a= 40 μm =0.4λ),

non-subdiced element with piston-only motion is formed. The magnitude of the electrical impedance for a bare PZT element with a piston-like behavior is shown in Figure 2.2(a). In the considered frequency band, a single minimum value of the electrical impedance occurs in this case at a frequency of 12.6 MHz. For this so called resonance frequency, the corresponding mode shape is shown, confirming that the element vibrates only along the thickness direction. When a matching layer is added on top of the PZT, the electrical impedance changes, as shown in Figure 2.2(b). It now has two minima and two resonance frequencies due to the presence of two different layers. For both resonance frequencies the indicated mode shapes are still showing the typical piston-like motion.

Figure 2.3 illustrates what happens to the electrical impedance for a wide element before and after subdicing. Figure 2.3(a) shows the electrical impedance of a wide element (a=120 µm =1.2λ) before subdicing. Multiple local minima are present, which correspond to different resonance modes. Two of the three resonance mode shapes are clearly showing an undesired non-uniform surface motion. The occurrence of the typical local minima in Figure 2.3(a) is an indication that subdicing will be opportune. Figure 2.3(b) shows the electrical impedance when the same element is provided with two subdicing cuts that extend to the bottom of the PZT layer. Doing so yields an electrical impedance plot with two minima and corresponding mode shapes with a piston-like behavior. For the wide element considered, subdicing has restored the desired situation of Figure 2.2(b).

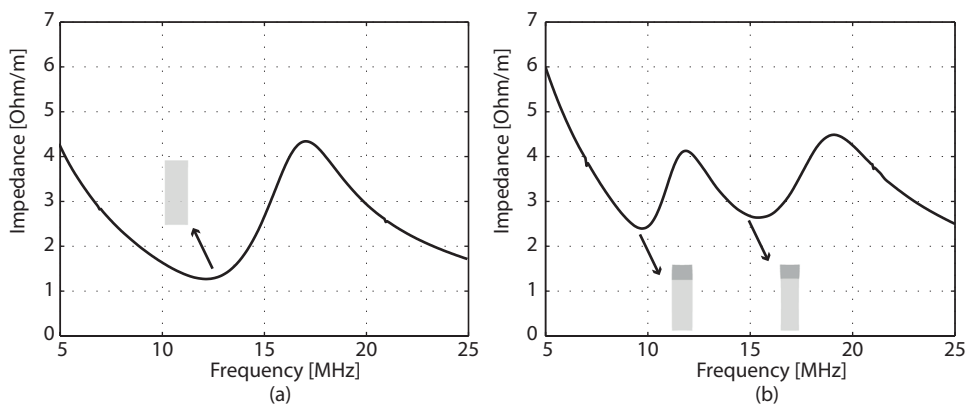

Figure 2.2 Plot of the electrical impedance per unit length for an element with a small width (a= 40 µm = 0.4λ) consisting of bare PZT (a) and PZT with a matching layer (b). The gray insets show the mode shapes for the resonance frequencies at each minimum (light gray=PZT; dark gray=matching layer).

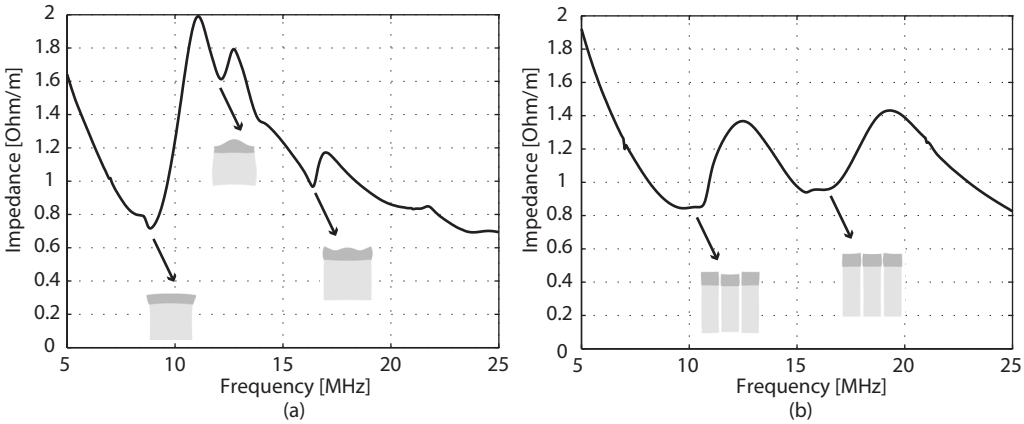

Figure 2.3 Plot of the electrical impedance per unit length for an element with a large width (a=120 μm =1.2λ) before subding (a) and after subdicing with 2 cuts that run through the entire PZT and matching layer (b). The gray insets show the mode shapes for the resonance frequencies at each minimum (light gray=PZT; dark gray=matching layer).

2.3 OPTIMAL NUMBER OF SUBDICING CUTS

We determined the optimal number of subdicing cuts for elements with widths a between 10 μm and 250 μm. We have defined the optimal number of cuts as the lowest n that yields $a/(n+1) \leq \lambda/2 = 50$ μm. We have numerically verified that this is the number of equidistant subdicing cuts that will exclude modes with non-uniform surface motion, i.e. for obtaining the situation in Figure 2.3(b). For the simulations, the central element was excited with a chirp pulse having a duration of 1 μs and a frequency sweep between 5 and 25 MHz. The chirp excitation was designed to have an even frequency content across the range of interest. The center frequency f_c of the subdiced element was obtained as the center of the -3 dB bandwidth of the average surface pressure.

In Table 2.2 the optimal number of subdicing cuts n and the corresponding center frequency f_c are shown for elements with different widths a. The table also shows the individual sub-pillar width w after subdicing as well as the products and $k_c a$ and $k_c w$, where:

$$k_c = \frac{2\pi f_c}{c} = \frac{2\pi}{\lambda_c}, \tag{2.1}$$

with c the speed of sound and λ_c the wavelength at f_c, both in water. The number of optimal subdicing cuts n varies from 0 to 4, while the sub-pillar width is ranging from 26 to almost 47 μm. After subdicing, the product k_c is always close to 2 and the frequency f_c is about 14 MHz for all the widths a. This confirms that after subdicing the dominant resonance frequency depends

mainly on the thickness of the element, which is kept constant. In all the remaining simulations, the resonant frequency f_c is used as the excitation frequency for each specific width a.

Table 2.2 The Optimal Number of Subdicing cuts , the Center Frequency f_c, the Sub-pillar Width w, and the Products $k_c a$ and $k_c w$, for Each Element Width a.

a	n	f_c [MHz]	w [μm]	$k_c a$	$k_c w$
10	0	17.9	10	0.75	0.75
20	0	15	20	1.26	1.26
30	0	14.5	30	1.83	1.83
40	0	13.5	40	2.27	2.27
50	0	12.8	50	2.69	2.69
60	1	14.6	26	3.68	1.59
70	1	14.3	32	4.20	1.92
80	1	14.2	36	4.77	2.15
90	1	13.4	42	5.07	2.36
100	1	13.1	46	5.50	2.53
110	2	14.7	33.3	6.79	2.06
120	2	14.5	36	7.31	2.19
130	2	14.3	40	7.81	2.40
140	2	13.9	42.7	8.17	2.49
150	2	13.5	46.7	8.50	2.65
160	3	14.4	35	9.68	2.12
170	3	14.3	38	10.21	2.28
180	3	14.1	40	10.66	2.37
190	3	13.6	38	10.85	2.17
200	3	13.5	45	11.34	2.55
210	4	14.3	37.6	12.61	2.26
220	4	14.2	39.2	13.12	2.34
230	4	14.1	41.6	13.62	2.46
240	4	13.8	43.2	13.91	2.50
250	4	13.6	45.6	14.28	2.60

2.4 RADIATION IMPEDANCE

For each width a and corresponding frequency f_c, two different types of excitations have been simulated: a 10-cycle sinusoid is used to simulate a quasi-continuous excitation, and a 2-cycle sinusoid is used to simulate an impulse like excitation, which is commonly employed in imaging systems. After driving the element with either type of excitation, the average pressure and the average velocity over its surface have been computed. In Figure 2.4(a) and Figure 2.4(b) the maximum of the envelope of the average pressure P_{max} and the maximum of the envelope of the average velocity v_{max} are plotted relative to $k_c a$, for both types of excitation and for both the non-subdiced and the optimally subdiced case.

The obtained values for P_{max} and v_{max} are also used to obtain the modulus of the radiation impedance Z. The latter quantity is defined for a piston moving in a perfectly rigid baffle as the average complex pressure amplitude divided by the real normal particle velocity amplitude [61].Therefore, $|Z|$ may be found from Figure 2.4(a) and Figure 2.4(b) as:

$$|Z| = \frac{P_{max}}{v_{max}} . \qquad 2.2$$

Figure 2.4(c) shows the relative radiation impedance $|Z_r|$, defined as:

$$|Z_r| = \frac{|Z|}{Z_{water}} , \qquad 2.3$$

where Z_{water}≅1.5 MRayl. Moreover, in Figure 2.4(c) the analytical curve for the radiation impedance of an infinitely long 2D strip with piston-like behavior in a rigid baffle is shown for comparison. This curve is the result of the numerical computation of the following equation (see Appendix for detailed derivation):

$$Z_r(\omega) = \frac{1}{K} \int_{-K/2}^{K/2} \int_{-K/2}^{y} H_0^{(2)}(y - y')dy'dy , \qquad 2.4$$

where $H_0^{(2)}$ is the Hankel function of the second kind and zero order, and K=$k_c a$.

For $k_c a$>3.5 (or a>0.55 λ_c), the pressure and velocity after subdicing are up to 3 times higher than those in the non-subdiced case for both types of excitations. This improvement in the transmit efficiency can be explained by two effects. The first effect of subdicing is the removal of modes with non-uniform surface motion, which causes an inefficient radiation into the acoustic medium. The second effect is a change in the electromechanical coupling factor of the PZT: when subdicing wide elements, the vibrational behavior of the PZT will change from plate mode to bar mode, which has a higher coupling factor [59,62,63].

In Figure 2.4(c), for $k_c a$<2 (or a<0.32 λ_c), the simulation results are in good agreement with the theoretical curve, confirming that for very small elements the radiation impedance drops quickly, impairing the energy radiation into the medium.

Without subdicing, the radiation impedance for the 10-cycle excitation shows an irregularity of 40% around $k_c a$=10, unlike the 2-cycle excitation. This difference in behavior may be explained by the bandwidth of the two excitation signals. For a quasi-continuous excitation with a narrow bandwidth, most of the energy is used to excite a specific frequency, which might correspond to a mode with non-uniform surface motion. The 2-cycle pulse simultaneously excites all occurring resonance frequencies, including the dominant thickness resonance. Therefore, simulations with narrow pulse excitation result in a radiation impedance that is in better agreement with the analytical derivation.

Disregarding the drop at $k_c a$=10 that is seen for the 10-cycle excitation in the absence of subdicing, the radiation impedances obtained from the simulations assume in general values higher than those expected from the analytical derivation. This may be caused by the fact that the analytical curve is derived for a piston in a rigid baffle, while the simulated model is more representative of a transducer in a baffle with a finite compliance. When a compliant baffle boundary condition is assumed, the pressure at the surface of the element is higher than that

for rigid baffle boundary condition [64]. Therefore, with a compliant baffle, a higher radiation impedance is expected.

Overall, for $k_c a$>5 (or a<0.48 λ_c) and an optimal number of subdicing cuts, a dominant thickness vibration is obtained for both types of excitation, which results in a relative radiation impedance close to 1. This means that the radiation impedance is almost equal to the acoustic impedance of the medium and, therefore, almost all the power is radiated into the far field.

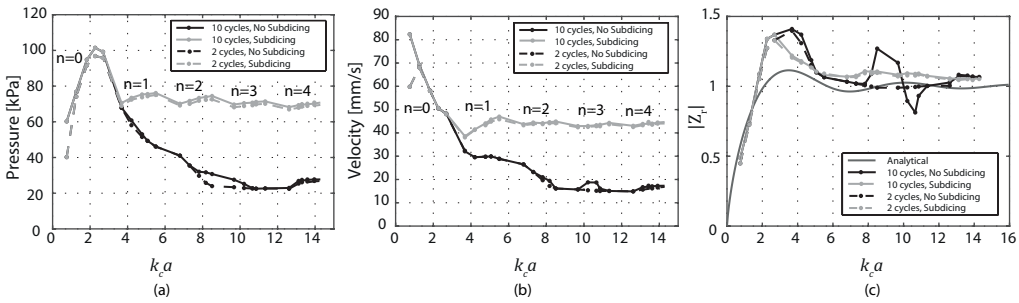

Figure 2.4 Maximum average pressure (a), maximum average velocity (b), and the relative radiation impedance (c) for both types of excitations, plotted against $k_c a$. The width a of the elements is varying from 10 μm to 250 μm. For the subdiced curves the optimal number of subdicing cuts n is indicated.

2.5 TIME AND FREQUENCY RESPONSE

In this section we consider the effect of subdicing on the time and frequency responses of the elements in transmit and receive. We consider four different element widths that require a different optimal number of subdicing cuts: a=60 μm ($k_c a \cong 3.7$), a=120 μm ($k_c a \cong 7.3$), a=180 μm ($k_c a \cong 10.7$), and a=240 μm ($k_c a \cong 13.9$). For the transmit response, a 2-cycle sinusoidal voltage excitation with 1 V amplitude is defined at the electrodes of the element, and the resulting emitted average pressure at the surface of the element is computed. For the receive response, a uniform 2-cycle sinusoidal pressure excitation with 1 Pa amplitude is defined close to the surface of the element, and the voltage at the electrodes of the element is computed.

For both the subdiced and the non-subdiced elements, the time trace of the transmitted pressures and the envelope of these signals are shown in Figure 2.5. For all but the smallest width, a relevant enhancement in the peak pressure amplitude is seen after subdicing, which is consistent with the results shown in Figure 2.4(a). For the non-subdiced case, Figures 2.5(b), (c) and (d) show multiple peaks in the envelopes and long ringing tails. Subdicing substantially reduces these adverse effects in the transmitted waveform.

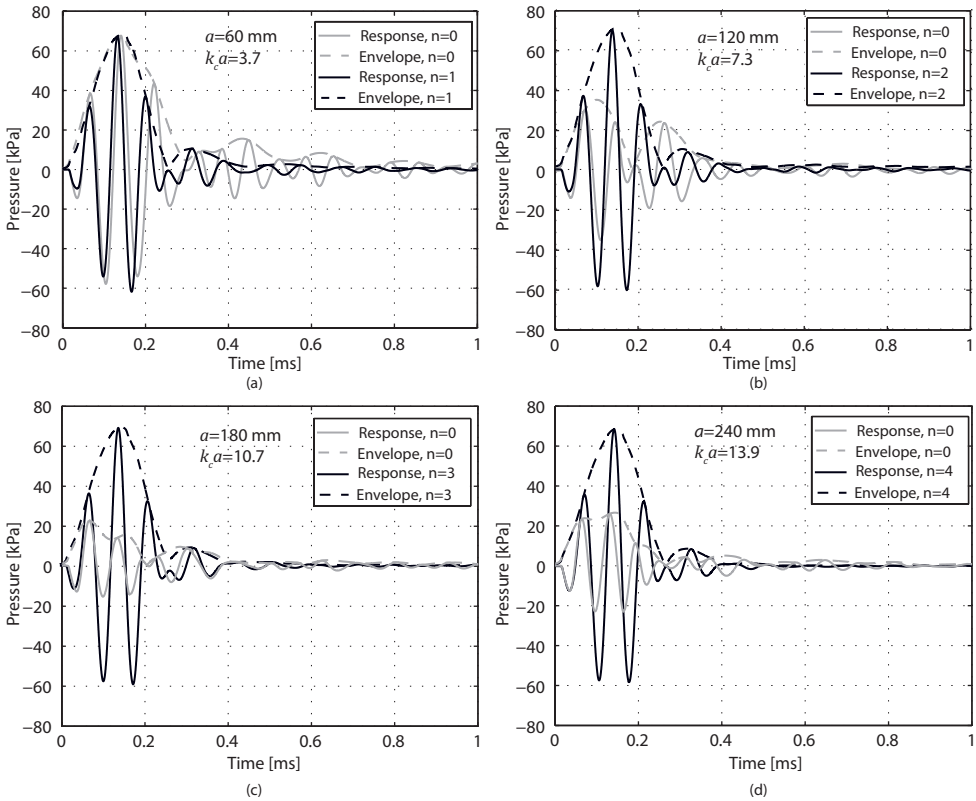

Figure 2.5 Average transmit pressure versus time for elements of size a=60 μm ($k_c a \cong 3.7$) (a), a=120 μm ($k_c a \cong 7.3$) (b), a=180 μm ($k_c a \cong 10.7$) (c), and a=240 μm ($k_c a \cong 13.9$) (d). Plots for both the non-subdiced (n=0) and the optimally subdiced ($n \neq 0$) case are given, with envelopes. Excitation occurs with a 2-cycle sinusoidal pulse with 1 V amplitude.

Figure 2.6 depicts the frequency responses of the subdiced and the non-subdiced elements, both for transmit and receive. The differences between subdiced and non-subdiced elements are also apparent in the frequency domain. For non-subdiced elements, Figure 2.6 shows strong spectral amplitude fluctuations in both transmit and receive spectra, which disappear after subdicing. In general, the frequency responses in transmit and receive have a similar shape after subdicing, although they are not exactly the same. The small differences are explained by the reciprocity equation [65], which relates the transmit function to the receive transfer function via the electrical impedance of the element. Another interesting observation from both the time responses and the frequency spectra is the similarity between the curves for all the different element widths after subdicing. This is because the final sub-pillar width is almost constant (see Table 2.2). This means that the time and frequency responses after subdicing have become dependent on the sub-pillar width rather than on the total element width. To further quantify the improvement of the time response of the transmitted pressure, we define the –6 dB and –20 dB ringing intervals $\Delta t_{-6\,dB}$ and $\Delta t_{-20\,dB}$, which are the time intervals over which

the amplitude of the envelope is greater than –6 dB and –20 dB of its corresponding maximum. In addition to that, we introduce the relative ringing amplitude, defined as the size of the second peak of the pressure envelope divided by the size of the first (main) peak. The frequency domain performance in transmit is further quantified by the relative –3 dB bandwidth ($BW_{-3\,dB}$), and the maximum dip within the band (in dB relative to the –3 dB level).

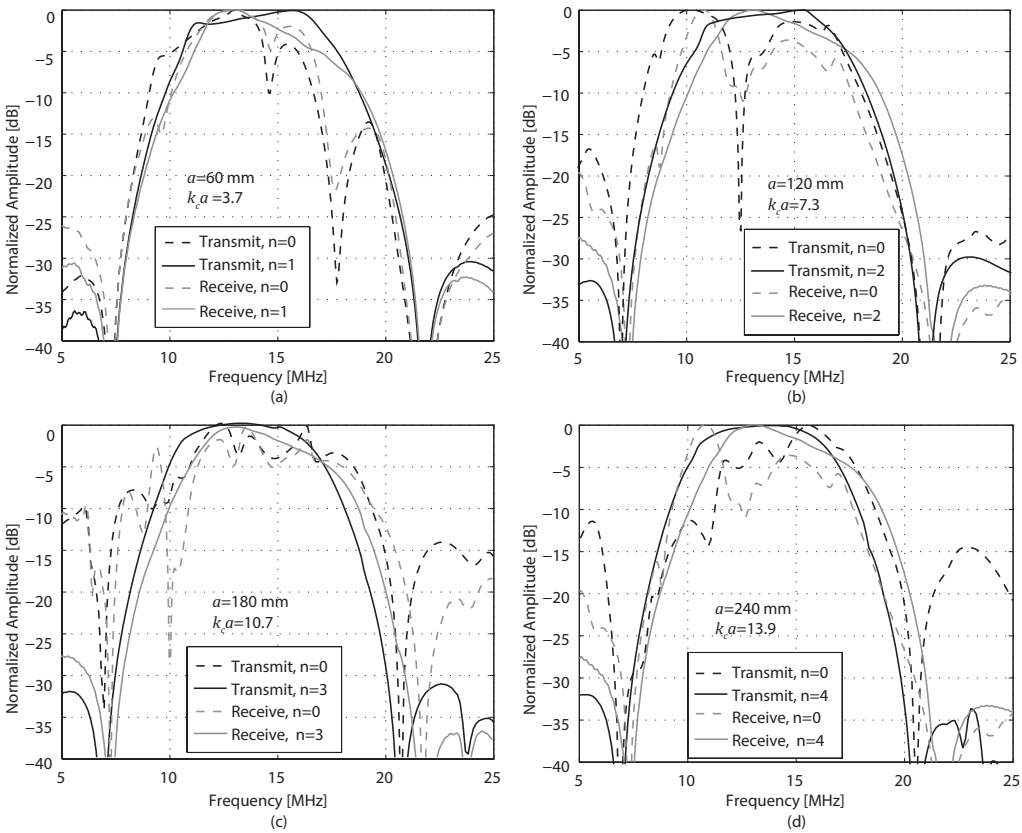

Figure 2.6 Frequency responses in transmit and receive for elements of size a=60 μm ($k_c a \cong 3.7$) (a), a=120 μm ($k_c a \cong 7.3$) (b), a=180 μm ($k_c a \cong 10.7$) (c), and a=240 μm ($k_c a \cong 13.9$) (d). Plots for both the non-subdiced (n=0) and the optimally subdiced ($n \neq 0$) case are given.

Table 2.3 lists these quantities for an element of size a=120 μm ($k_c a \cong 7.3$) and a number of subdicing cuts ranging from 0 to 4. For this particular element, two subdicing cuts remove the spurious modes from the electrical impedance (Figure 2.3). However, it is interesting to investigate if n=2 is also optimal in terms of time and frequency response. Table 2.3 shows that when is increased from 0 to 2 the ringing times are shortened and the relative ringing amplitude is decreased. For n=2, a –3 dB bandwidth of 43.2% without dips is obtained. However,

no further substantial improvement is obtained for n>2. Therefore, for optimal performance in both the time and the frequency domain, two subdicing cuts are sufficient.

The considerations for $k_c a \cong 7.3$ can be extended to the other element widths. In Table 2.4 the characteristic time and frequency domain quantities are shown for the non-subdiced and the optimally subdiced cases. The results demonstrate that the ringing time may be shortened by up to 50% ($\Delta t_{-20\ dB}$ for $k_c a \cong 13.9$) and the relative ringing amplitude may be decreased by up to 80% ($k_c a \cong 7.3$). Moreover, the maximum increase in bandwidth is 77% ($k_c a \cong 3.7$), while the maximum dip is reduced by up to around 24 dB ($k_c a \cong 7.3$).

Table 2.3 Characteristic Time Domain and Frequency Domain quantities for an element of size a=120 µm ($k_c a \cong 7.3$) and the number of subdicing cuts n ranging from 0 to 4.

	n	$\Delta t_{-6\ dB}$ [ms]	$\Delta t_{-20\ dB}$ [ms]	Ringing Amplitude (%)	$BW_{-3\ dB}$ (%)	Max. dip [dB]
a=120 µm $k_c a$=7.3	0	0.25	0.42	69.0	60.2	23.7
	1	0.17	0.58	13.2	29.8	8.4
	2	0.14	0.32	13.5	43.2	0
	3	0.14	0.33	15.4	44	0
	4	0.14	0.33	15.6	45	0

Table 2.4 Characteristic time domain and frequency domain quantities for elements of size a=60 µm ($k_c a \cong 3.7$), a=120 µm ($k_c a \cong 7.3$), a=180 µm ($k_c a \cong 10.7$), and a=240 µm ($k_c a \cong 13.9$). Data for both the non-subdiced (n=0) and the optimally subdiced ($n \neq 0$) case are given.

	n	$\Delta t_{-6\ dB}$ [ms]	$\Delta t_{-20\ dB}$ [ms]	Ringing Amplitude (%)	$BW_{-3\ dB}$ (%)	Max. dip [dB]
a=60 µm $k_c a$=3.7	0	0.18	0.64	23	25.5	0
	1	0.14	0.34	15.4	45.1	0
a=120 µm $k_c a$=7.3	0	0.25	0.42	69	60.2	23.7
	2	0.14	0.32	13.5	43.2	0
a=180 µm $k_c a$=10.7	0	0.14	0.32	41.8	37.4	1.2
	3	0.14	0.29	13.3	45.2	0
a=240 µm $k_c a$=13.9	0	0.15	0.65	19.1	27.2	1.3
	4	0.14	0.32	12.7	45.1	0

2.6 DIRECTIVITY PATTERN

Directivity can be calculated in PZFlex using the extrapolation toolkit, which enables the computation of the magnitude of the transmitted pressure in the far field, assuming linear propagation. The directivity patterns for both the non-subdiced and the optimally subdiced cases are shown in Figure 2.7. Additionally, in the same figure we show the analytical curve of the directivity $D(\theta)$, which follows from:

$$D(\theta) = \mathrm{sinc}\left(\frac{a\sin(\theta)}{\lambda}\right), \qquad 2.5$$

with θ the observation angle, a the transducer width and λ the wavelength [59]. This expression holds for an ideal piston in a rigid baffle.

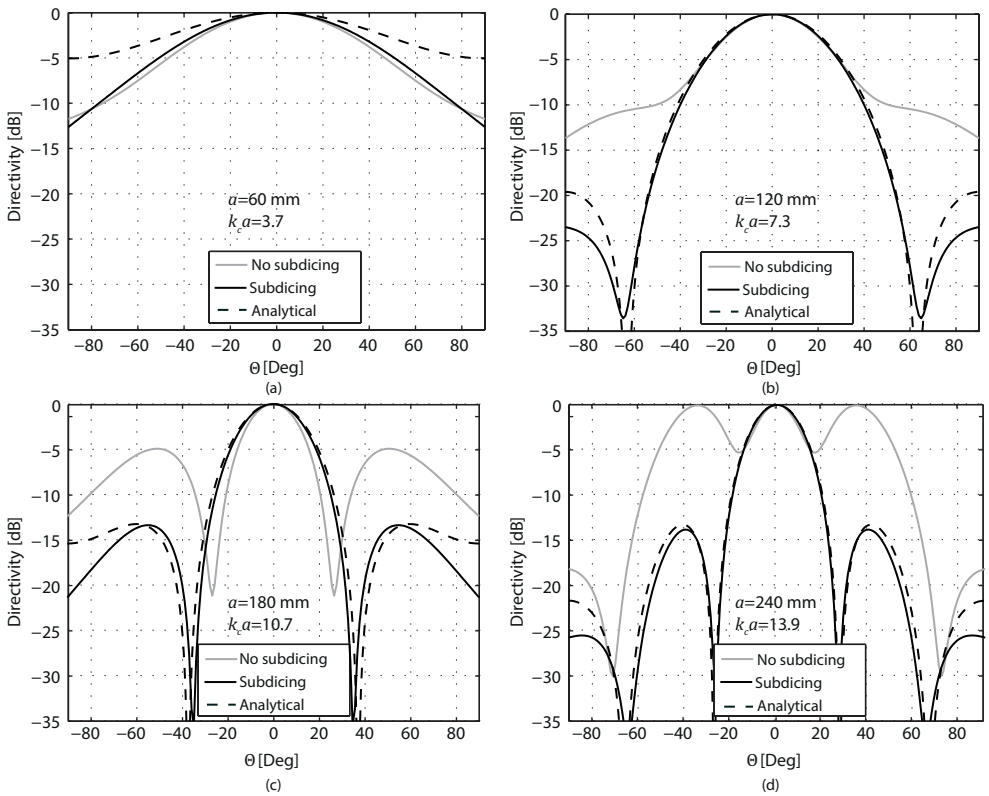

Figure 2.7 Directivity plots for elements of size a=60 μm ($k_c a \cong 3.7$), (a) a=120 μm ($k_c a \cong 7.3$), (b), a=180 μm ($k_c a \cong 10.7$) (c), and a=240 μm ($k_c a \cong 13.9$). (d) Plots for both the non-subdiced (n=0) and the optimally subdiced ($n \neq 0$) case are given, together with the analytical curve.

For the smallest element size a=60 μm ($k_c a \cong 3.7$) no side lobes are present and no substantial difference is seen between the non-subdiced and the subdiced cases. The other element sizes give rise to side lobes, which are reduced by subdicing. Moreover, the directivity patterns for the subdiced elements are in good agreement with the analytical curves. This agreement further demonstrates the benefits of subdicing in achieving the ideal piston-like behavior.

It is important to mention that the directivity and, hence the choice of the element width, will depend on the specific application [64].

2.7 SUBDICING DEPTH

Because the cutting depth is an important aspect in the construction of a transducer, in this section we consider the influence of using subdicing cuts that do not extend to the bottom of the PZT layer. The depth of the subdicing cut is varied from 0 to 100% of the total element thickness, i.e. the thickness of the PZT and the matching layer, in steps of 10%. Figure 2.8 shows the maximum of the average surface pressure, relative ringing amplitude, bandwidth, and maximum dip within the frequency band, as function of the depth of the subdicing cut.

For a=60 μm ($k_c a \cong 3.7$), both the maximum average surface pressure (Figure 2.8(a)) and the relative ringing amplitude (Figure 2.8(b)) are almost constant for increasing depth of cut because the element is so small that piston motion is predominant even in the non-subdiced case. This is in agreement with the results of the previous sections. For wider elements the increase in pressure and the decrease in relative ringing amplitude are appreciable when subdicing up to 70% of the total element thickness. The –3 dB bandwidth (Figure 2.8(c)) and the maximum dip within the band (Figure 2.8(d)) as function of the depth of the cut have a less clear trend for the different element widths. Nevertheless we can state that to have both a large bandwidth and avoid strong fluctuations within the band, the depth of the cut should be between 70 and 100%, irrespective of the width of the element. In this range also the emitted pressure and the relative ringing amplitude are about constant and assume the highest and lowest value, respectively.

Figure 2.9 shows the relative side lobe levels for single elements of size a=180 μm ($k_c a \cong 10.7$) and a=240 μm ($k_c a \cong 13.9$) as function of the depth of the cut. For increased subdicing depth, the side lobes are reduced and, similar to the other characteristic quantities, for a depth of cut between 70 and 100%, an almost constant minimum value is reached.

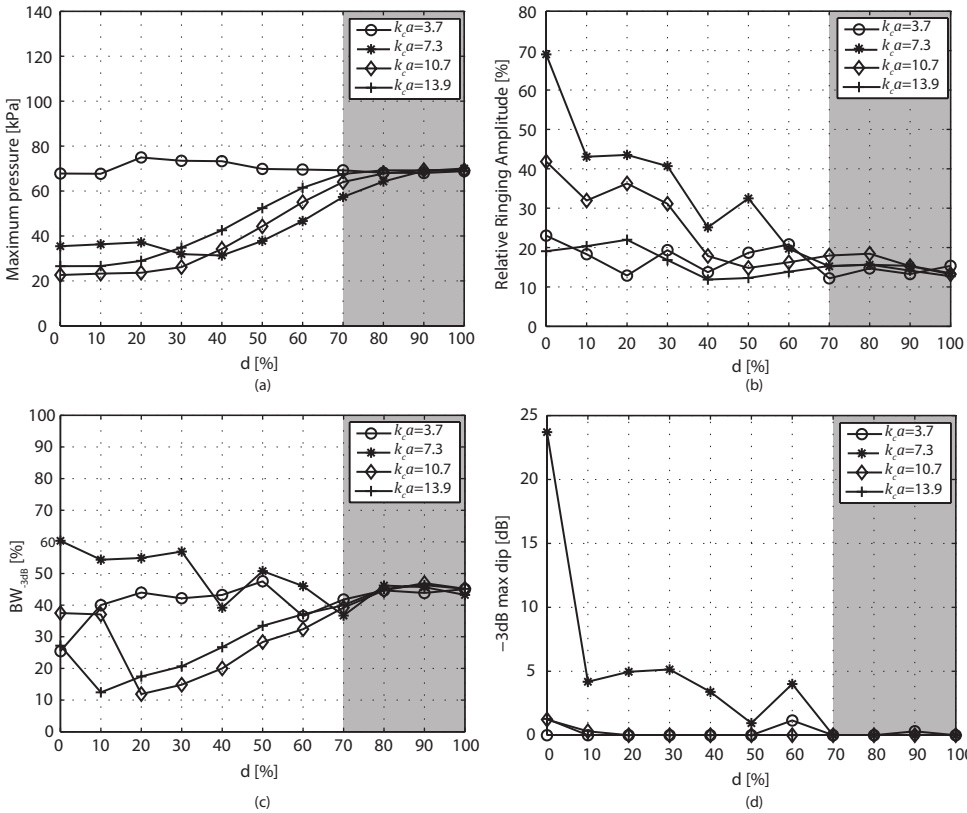

Figure 2.8 Influence of the relative depth of the subdicing cut *d*. Maximum average surface pressure (a), relative ringing amplitude (b), relative –3 dB bandwidth in % (c), maximum dip in the frequency band (d). Data are shown for elements of size a=60 µm ($k_c a \cong 3.7$), a=120 µm ($k_c a \cong 7.3$), a=180 µm ($k_c a \cong 10.7$), and a=240 µm ($k_c a \cong 13.9$). In each case, the optimal number of subdicing cuts is applied. In the shaded area, almost no further improvements are obtained.

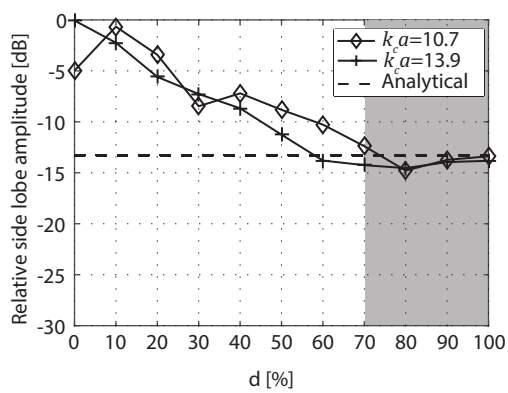

Figure 2.9 Relative side lobe level versus the relative depth of the subdicing cut. Data are shown for elements of size a=180 µm ($k_c a \cong 10.7$) and a=240 µm ($k_c a \cong 13.9$). In the shaded area, almost no further improvements are obtained. The dashed line is the analytical side lobe level.

2.8 CONCLUSION

In this study we have shown, through FEM simulations, that subdicing improves the performance of transducer elements having a width greater than 0.6 times the resonance wavelength in water. More precisely, subdicing improves the emitted pressure, the radiation impedance, the time response, the frequency response, and the directivity pattern.

The increase in the emitted pressure and in the radiation impedance after subdicing leads to an increase in the power radiated into the medium. High power is beneficial for improved signal-to-noise ratio during imaging. Regarding the time response, we showed that subdicing reduces the ringing time and the ringing amplitude. Ringing is an unwanted effect, which occurs when the radiation impedance of an element including a matching layer deviates from the impedance of the medium. This is the case when there is a non-uniform motion of the element surface. Subdicing restores the uniform motion at the surface and thus ringing will be avoided. A time response without ringing has a shorter pulse length, which in turn improves the axial imaging resolution. The frequency response also benefits from subdicing by obtaining a higher bandwidth and avoiding strong spectral dips.

Regarding the directivity pattern, low levels of side lobes are necessary to avoid imaging artifacts originating from off-axis ultrasound beams. We have shown that subdicing can also reduce the side lobe levels of wide elements. The depth of the subdicing cut may be crucial during the fabrication process. Cutting all the way through the element can lead to mechanical instability and cause damage to the electrodes. We have demonstrated by our simulations that it is possible to achieve the most significant improvements in transducer performances by cutting to only a depth of 70% of the total element thickness.

We expect that the presented quantitative knowledge about the effect of subdicing on the transducer performances may help to improve the design of high quality imaging transducers.

APPENDIX: RADIATION IMPEDANCE FOR A 2D STRIP

In order to derive the radiation impedance for a 2D strip of width a and uniform velocity $v_0\exp(j\omega t)$over the surface, we assume a rigid baffle boundary condition and we consider the two-dimensional frequency-domain Green's function [66]:

$$G(x,z,\omega)=-\frac{j}{4}H_0^{(2)}(kr)\ \ with\ r=\sqrt{x^2+z^2} \tag{2.6}$$

where x is the coordinate in the direction of the width of the strip, z is the coordinate in the direction perpendicular to the strip surface, $H_0^{(2)}$ is the Hankel function of the second kind and order zero, and k is the wave number. The Rayleigh integral for the pressure $p(x,z,\omega)$is then:

$$p(x,z,\omega)=j\omega\rho_0 v_0\int_{-a/2}^{a/2}-\frac{j}{2}H_0^{(2)}(kr)\,dx' \quad with\ r=\sqrt{(x-x')^2+z^2} \tag{2.7}$$

and at the surface, where z=0, we have:

$$p(x,\omega)=\frac{\omega\rho_0 v_0}{2}\int_{-a/2}^{a/2}H_0^{(2)}(k|x-x'|)\,dx' \tag{2.8}$$

The average pressure over the strip surface is then:

$$p^A(\omega)=\frac{\omega\rho_0 v_0}{2a}\int_{-a/2}^{a/2}\int_{-a/2}^{a/2}H_0^{(2)}(k|x-x'|)\,dx'dx \tag{2.9}$$

Because of the symmetry in the integration domain we may replace the integral in (2.9) by twice the integral over a triangle. Thus:

$$p^A(\omega)=\frac{\omega\rho_0 v_0}{a}\int_{-a/2}^{a/2}\int_{-a/2}^{x}H_0^{(2)}[k(x-x')]\,dx'dx \tag{2.10}$$

Therefore, the acoustic radiation impedance can be expressed as:

$$Z(\omega)^A=Z_0\frac{1}{K}\int_{-K/2}^{K/2}\int_{-K/2}^{y}H_0^{(2)}(y-y')\,dy'dy \tag{2.11}$$

where Z_0 is the acoustic impedance of the medium, K=ka, y=kx, and y'=kx'. This form can easily be evaluated by numerical means.

Chapter 3

A 2D Ultrasound Transducer with Front-End ASIC and Low Cable Count for 3D Forward-Looking Intravascular Imaging: Performance and Characterization

Jovana Janjic, Mingliang Tan, Verya Daeichin, Emile Noothout, Chao Chen, Zhao Chen, Zu-yao Chang, Robert H.S.H. Beurskens, Gijs van Soest, Antonius F. W. van der Steen, Martin Verweij, Michiel A. P. Pertijs, Nico de Jong, A 2D Ultrasound Transducer with Front-End ASIC and Low Cable Count for 3D Forward-Looking Intravascular Imaging: Performance and Characterization, *submitted to IEEE. Trans Ultrason Ferroelectr Freq Control.*

ABSTRACT

Intravascular ultrasound is an imaging modality used to visualize atherosclerosis from within the inner lumen of human arteries. Complex lesions like chronic total occlusions require forward-looking intravascular ultrasound (FL-IVUS), instead of the conventional side-looking geometry. Volumetric imaging can be achieved with 2D array transducers, which present major challenges in reducing cable count and device integration. In this work we present an 80-element lead zirconium titanate (PZT) matrix ultrasound transducer for FL-IVUS imaging with a front-end application-specific integrated circuit (ASIC) requiring only 4 cables. After investigating optimal transducer designs we fabricated the matrix transducer consisting of 16 transmit (TX) and 64 receive (RX) elements arranged on top of an ASIC having an outer diameter of 1.5 mm and a central hole of 0.5 mm for a guidewire. We modeled the transducer using finite element analysis and compared the simulation results to the values obtained through acoustic measurements. The TX elements showed uniform behavior with a center frequency of 14 MHz, a -3 dB bandwidth of 44% and a transmit sensitivity of 0.4 kPa/V at 6 mm. The RX elements showed center frequency and bandwidth similar to the TX elements, with an estimated receive sensitivity of 3.7 μV/Pa. We successfully acquired a 3D FL image of three spherical reflectors in water using delay-and-sum beamforming and the coherence factor method. Full synthetic aperture acquisition can be achieved with frame rates on the order of 100 Hz. The acoustic characterization and the initial imaging results show the potential of the proposed transducer to achieve 3D FL-IVUS imaging.

3.1 INTRODUCTION

Ischemic heart disease is the leading cause of morbidity and mortality worldwide [67], caused by reduced blood flow in the coronary arteries that supply the heart. The development of atherosclerotic plaques within the coronary arteries leads to either a gradual narrowing of the free lumen, or sudden blockage due to plaque rupture and subsequent thrombosis [68,69]. Intravascular ultrasound (IVUS) is nowadays employed to assess the pathophysiology of atherosclerosis from within the vessel lumen, and to guide minimally-invasive therapeutic interventions with stents [19]. IVUS is an imaging modality that uses a small catheter (approx. 1 mm diameter) with an integrated ultrasound transducer to visualize arteries from inside. Most commercially available IVUS catheters provide a cross-sectional view of the vessel. This is achieved by rotating a single-element transducer, mounted on the side of the catheter and transmitting ultrasound waves in the radial direction from the catheter. The ultrasound waves are then reflected back from the vessel wall to the transducer [70,71]. An electronically steered IVUS catheter also exists (Eagle Eye, Volcano Therapeutics) consisting of an array of 64 transducer elements mounted around the tip of the catheter and interfaced with integrated circuits requiring 7 coaxial cables [18,35].

Side-looking IVUS catheters are restricted to use in non-occlusive lesions by their imaging geometry, limiting their application in the treatment of very complex lesions, such as Chronic Total Occlusions (CTOs) [72]. CTOs are plaques that have grown to completely fill the vessel lumen. They typically have a highly heterogeneous tissue composition, with variable mechanical properties and presence of microchannels [23]. Treatment consists of passing the lesion with a thin (0.3 mm) guidewire and opening the vessel with a balloon and stent. Imaging the plaque with forward-looking (FL) ultrasound transducers, integrated into a steerable catheter may direct the physician to optimal locations for wire entry, providing imaging guidance during the crossing procedure and enhancing the device dexterity.

Early work in the development of forward-looking intravascular ultrasound (FL-IVUS) consisted of single-element transducers with a rotating mechanism that is either converted into a scanning motion of the FL element [24,25], or directly applied to rotate an element oriented at a 45° angle [27]. In the first case 2D FL scans can be achieved, whereas with the second approach a cone of visualization is created ahead of the catheter tip. Other approaches for single-element FL imaging include a rotating reflecting surface [28] that reflect the ultrasound beam with different angles ahead of the catheter tip and a mechanically wobbling transducer with shape-memory alloys [26]. These approaches require the need to develop complex mechanisms, making the whole catheter bulky.

Considerable effort has been put into the development of multi-element arrays, which do not need rotation. Miniaturized linear arrays that provide 2D FL ultrasound images [29,30,73] can achieve volumetric imaging by mechanically scanning the transducer and combining different

2D planes into a 3D volume data set. This procedure is complex and easily affected by motion artifacts. Two-dimensional matrix transducers can provide volumetric imaging without moving the probe. However, integration of multi-element transducers in intravascular catheters is challenging because of the complexity of wiring the many elements to a signal acquisition system. Matrix and ring arrays with approximately 100 individually connected elements have been pioneered for IVUS applications [32,33]. However, there is usually not enough space in the catheter for these large wire assemblies. Electronic circuits with pulsers and multiplexers, integrated with the 2D matrix transducer, can reduce the cable count. This approach has been used in the development of FL intravascular and intracardiac transducers based on Capacitive Micromachined Ultrasonic Transducers (CMUT) [36,39-44], which are fabricated using silicon-based technologies and can be co-integrated with front-end electronics to reduce the interconnection complexity [74,75]. FL CMUT-based transducers for intravascular and intracardiac applications requiring 13 coaxial cables have been proposed [42,43].

In an elegant combination of a side-looking and a forward looking array [34,76], the distal part of a 64 element circular side-looking array was cut and used to generate forward waves in the 3-1 mode. With the resulting annular array, the number of transceiver firings can be optimized to yield 3D FL imaging with reasonable side and grating lobe level (-20 dB side-lobe and almost -30 dB grating lobe level at a steering angle of 30°). Experimentally, a side lobe level of approximately -15 dB was realized, probably due to missing elements [34]. Moreover, since 3D FL imaging is achieved using only a narrow ring of elements, power dissipation and sensitivity remain a concern.

An intracardiac side-looking PZT-based array with an application specific integrated circuit (ASIC) has been integrated in a 10 Fr (3.3 mm) steerable catheter and tested in vivo [20]. This device consists of a 2D matrix transducer with an aperture of 2.5×6.6 mm^2, a pitch of 180 μm and a center frequency of 5.6 MHz. The element-matched connection with the ASIC was realized via a flexprint and a dematching layer between the ASIC and the PZT in order to minimize the acoustic energy transport into the backing.

Next to FL imaging, minimally invasive procedures could benefit from steerability of intravascular devices. Single-element FL imaging using a steerable catheter and an optical shape sensing system has been demonstrated in a previous publication by our group [77]. For each degree of freedom (DOF), two pulling wires are required. To accommodate multiple pulling wires, hence improving device dexterity, it is important to reduce the number of coaxial cables.

We propose here a PZT-based FL-IVUS matrix transducer built on a front-end ASIC, that requires only 4 micro-coaxial cables to address a 2D matrix array with a total of 80 elements. The micro-coaxial cables could easily fit in an intravascular catheter and leave space for a guidewire and up to 8 pulling wires, hence enabling steering with 4 DOF. The PZT has been mounted directly on the ASIC with gold ball contacts and conducting glue. The ASIC and transducer have been

designed in conjunction, as their mutual performance is tightly linked. The electronic design of the ASIC was reported previously [78]. In this paper we focus on the design, the fabrication process and the quantitative characterization of the FL-IVUS transducer built on top of the ASIC. We also performed FL volumetric imaging of three spherical reflectors in water.

In section 3.2 we investigate different transducer designs using Field II simulations [79-81]. Based on the simulation results we estimate the effects of a practical implementation and we present the final device design, the finite element analysis (FEA) model used to simulate the acoustic behavior and the experimental set-up for ultrasonic characterization in section 3.3. FEA and measurement results are presented in section 3.4 and the discussion and conclusions are given in section 3.5.

3.2 OPTIMAL TRANSDUCER LAYOUT ANALYSIS

Intracoronary ultrasound catheters have a maximum outer diameter of 1.5 mm and should accommodate a ~0.3 mm diameter flexible guidewire for accurate delivery. To meet these requirements, the most suitable approach is to build the transducer directly on top of an ASIC, similar to [40,42]. The envisioned block diagram of the ASIC is shown in Figure 3.1. The ASIC will employ high-voltage (HV) switches to connect one or multiple transmit (TX) elements to an external pulser, whereas a multiplexer will connect one of the receive (RX) elements to an analog front-end (AFE) that consists of a trans-impedance amplifier (TIA) with very small input impedance, a programmable gain amplifier (PGA) with three gain settings and a buffer which serves as a cable driver. The ASIC should enable synthetic aperture imaging where acoustic pulses are transmitted using one or multiple TX elements, and the reflected echoes are received by the RX elements one element at a time. Beside the described analog approach, the ASIC will also be capable of locally digitizing the received signals, providing more robust signal transmission [78]. However, since the main focus of this work is the acoustic characterization of the 2D matrix transducer on top of the ASIC, we considered the ASIC in analog mode only.

Considering the available area for the ASIC and the dimensions of each chip components, we estimated that the ASIC could address a maximum of approximately 100 receive elements. This number can only be achieved by minimizing the number of transmit elements since the high voltage switches are the largest components (approximately $100\times100\ \mu m^2$) occupying the ASIC area. Based on these considerations, the maximum number of transmit elements was set to 16.

The target center frequency is 14 MHz, which is lower than standard IVUS frequencies (20–40 MHz), but can provide more penetration depth suitable for FL imaging [43,76]. For reduced grating lobes, a pitch smaller than the wavelength λ is desirable. However, the available transducer fabrication process, which is described later, limits the pitch to a minimum

of 100 µm. We summarize the transducer requirements and the constraints due to the ASIC and the fabrication process in Table 3.1.

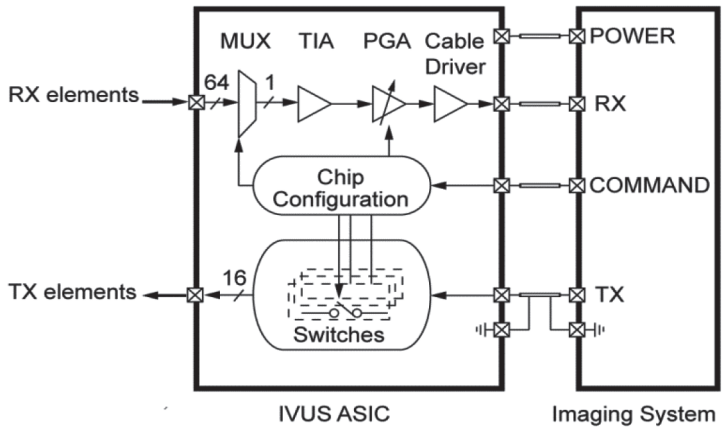

Figure 3.1 Block diagram of the ASIC. MUX: multiplexer, TIA: trans-impedance amplifier, PGA: programmable gain amplifier. The ASIC requires only 4 cables to connect the 2D matrix transducer to the external imaging system.

Table 3.1 FL-IVUS Transducer Requirements and Constraints

Requirements		Constraints	
center frequency	14 MHz		
pitch	< λ	min. pitch	100 µm
outer diameter	1.5 mm	max. num. of TX	16
inner hole diameter	0.5 mm	max. num. of RX	100

With these considerations in mind we investigated, through ultrasound field simulations in Field II, different 2D matrix designs. The investigated designs are described in Table 3.2. In the first three designs the TX and the RX elements were arranged on a regular grid with a pitch of 100 µm and a kerf of 20 µm. Transducers with these layouts can be manufactured using a diamond dicing saw. The last design consisted of TX and RX elements arranged in a non-gridded pattern. In particular, the receivers were placed according to a tapered spiral pattern [82] with variable pitch (≥ 100 µm). A transducer with this configuration can be manufactured with laser cutting technology.

Table 3.2 Investigated Transducer Designs

Design Type	Layout (TX in yellow, RX in red)	TX elements	RX elements
A	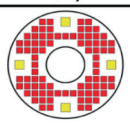	4 (100 X 100 µm)	84 (80 X 80 µm)
B	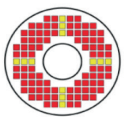	12 (80 X 80 µm)	88 (80 X 80 µm)
C	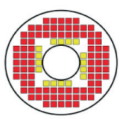	16 (80 X 80 µm)	88 (80 X 80 µm)
D	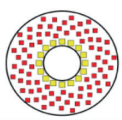	16 (60 X 60 µm)	77 (60 X 60 µm)

For each design, we computed the pulse-echo (PE) beam profile on a half spherical surface with a radius of 6 mm (Figure 3.2(a)) and we simulated the 3D synthetic aperture imaging of 3 point scatterers (Figure 3.2(b)). The transducer is simulated in the xy plane with z the propagation axis. For each PE beam profile, we also extracted the maximum side-lobe level at each elevation angle as shown in Figure 3.3.

In design **A**, where four TX elements are organized at the top, bottom, left and right side of the transducer aperture, the simulated PE field showed maximum side-lobe levels of -15 dB at approximately 10° as shown in Figure 3.3. Increasing the number of TX elements and positioning them in a cross-like pattern (design **B**) reduced the maximum side-lobe level to approximately -19 dB. However, the beam profile showed still a significant spread in the energy around the main beam as shown in Figure 3.2.

By positioning the TX elements around the inner hole (design **C** and **D**) both the side-lobe level and the beam spread were reduced. The non-gridded configuration of the RX elements in design **D** gave the narrowest beam spread and the smallest side-lobe level. Nevertheless, the improvement over design **C** was not as significant as compared to the other designs. Laser cutting transducer elements which are mounted on top of an ASIC is not trivial and requires accurate control of the cutting depth to avoid damage to the chip. On the other side, the cutting depth of the mechanical dicing saw can be more easily controlled. Therefore, in this work, we opted for design **C** to prove the concept of 3D FL-IVUS imaging using a 2D matrix transducer with a front-end ASIC and a low cable count.

A comparison of our approach with previous work is provided in Table 3.3. Our transducer with front-end ASIC requires the lowest number of cables and, using the highest number of firings (1024), results in grating lobes of approximately -30 dB when steering by 30°, retaining frame rates suitable for real time imaging (~100 Hz).

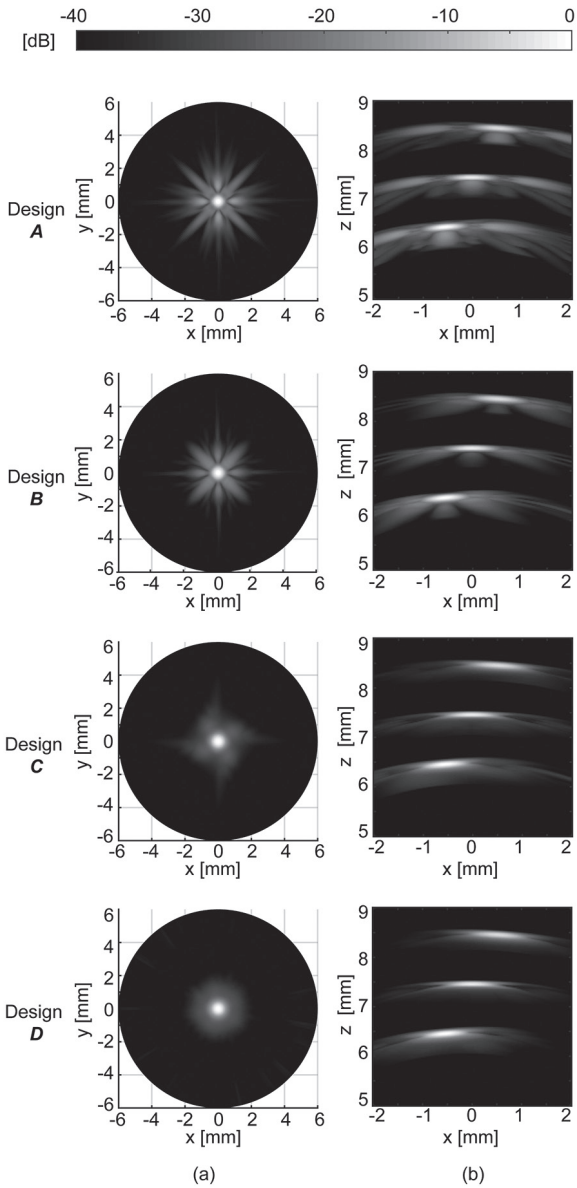

Figure 3.2 (a) Simulated pulse-echo (PE) profiles on a half spherical surface with radius 6 mm; (b) Maximum projections along y-axis of simulated synthetic aperture images of 3 point scatterers.

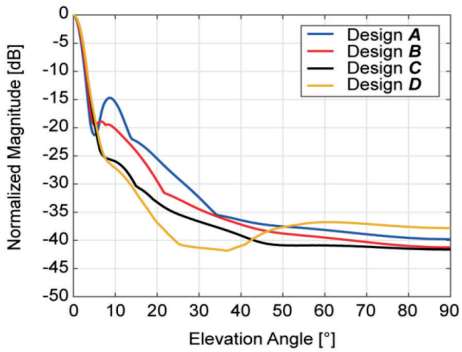

Figure 3.3 Maximum lobe level at each elevation angle. Curves are extracted from Figure 3.2(a).

Table 3.3 Comparison with prior work

	Design C	[34] and [76]	[32]	[42]	[20]
Frequency [MHz]	14	10	10	20	5.6
Diameter [mm]	1.5	1.3	1.6	1.4	3.3
Number of cables	4	7	97	13	88
Number of elements	82	64	97	104	-
Vibrating mode / relative sensitivity	d_{33} / 100%	d_{31} / 50%	d_{33} / 100%	-	d_{33} / 100%
Proposed number of firing	1024	210	-	672	-
Frame rate [Hz]	100	500	-	60	30
Grating lobe level at 30 deg steering [dB]	-30	-30	-	<-40	<-35
Construction	PZT on ASIC	PZT on flexprint	Coax	CMUT	PZT on ASIC

3.3 TRANSDUCER DESIGN AND CHARACTERIZATION

3.3.1 Final Transducer Layout

The final transducer design was further adjusted to accommodate the five bond pads for the ASIC connection to four micro-coaxial cables and to ground. Since these pads, in the current ASIC design, are located on the same side of the ASIC as the transducer array, transducer elements could not be placed at their location. Each pad has a size of 100 µm×100 µm and a safety distance of 70 µm from the transducer elements.

To integrate the five bond pads in the limited chip area, the number of RX elements was decreased to 64, leading to a design that had a total of 80 elements (16 TX and 64 RX elements) with an element size of 80×80 µm and a pitch of 100×100 µm. The layout is shown in Figure 3.4 together with the simulated PE beam profile and the maximum projection from a synthetic aperture image of three scatterers. The -6 dB lateral width of the point scatterer at 6.5 mm is 540 µm.

The changes in the layout due to the inclusion of the bond pads lead to a spread in energy around the main beam and an increase in the side lobe level compared to design ***C*** (Figure 3.2). However, the maximum side lobe level at 10° is below -20 dB (Figure 3.4(c)), which is still better than both design ***A*** and ***B***.

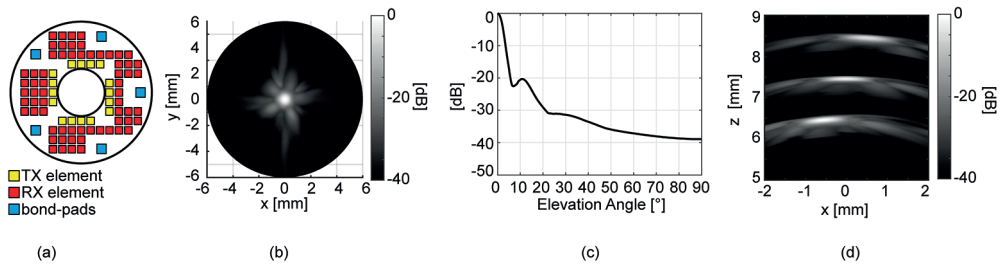

Figure 3.4 (a) Final design layout; (b) simulated PE beam profile over a half spherical surface with radius 6 mm; (c) extracted maximum side lobe level for each angle; (d) maximum projection of a simulated full synthetic aperture image of three point scatterers.

3.3.2 Finite Element Modelling

We modelled the transducer on top of the ASIC and simulated its acoustic performance using finite element analysis software (PZFlex LLC, Cupertino, CA, USA). The 3D model geometry consisted of three transducer elements where only the central one is active (Figure 3.5). The layer stack consists of, bottom to top, the silicon substrate containing the ASIC, a non-conductive epoxy filling the gaps between the electrical connections, a conductive adhesive backing, the PZT active layer, a conductive matching layer and a thin aluminium ground electrode. The kerfs between the elements were kept void and the overall transducer was loaded with water. The material properties and thicknesses of each layer are described in Table 3.4. The mesh used in PZFlex has a spatial resolution of 2 µm that was achieved by considering 15 grid elements per minimum wavelength for the lowest occurring speed of sound of 1482 m/s and a maximum frequency of 50 MHz. To reduce the simulation time, we assumed symmetry in the planes $x=0$ and $y=0$, hence only a quarter of the model needed to be simulated.

To study the transmit performance of the single element, a half-period sinusoidal pulse with a 28 Vpp amplitude and a pulse width of 25 ns is applied to the element. The -3 dB fractional bandwidth of the pulse is approximately 180%. Using the Kirchhoff extrapolation technique [83], the simulated pressure at the surface is propagated into water over 6 mm in the axial

direction. Using PZFlex, we also extrapolated the element impedance at resonance, which was used to design the AFE in the ASIC.

The receive behavior of the individual element is investigated through simulations by defining close to the transducer surface the same pressure load that was obtained from the measurements in transmission. For these simulations we also took into account the input impedance of the AFE in the ASIC. First, a SPICE-type simulator (Spectre Circuit simulator, Cadence Design Systems, Inc., San Jose, CA 95134, USA) was used to obtain the magnitude and phase of the AFE input impedance over different frequencies. Then, we fitted the resulting value to an RC equivalent circuit, which was modeled in PZFlex as connected in parallel to the element.

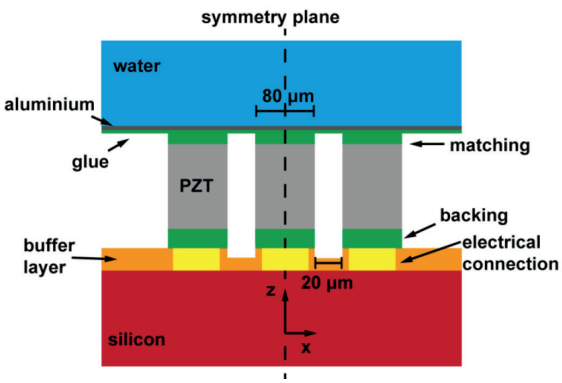

Figure 3.5 The 3D FEA model in the xz plane.

Material	Thickness	Properties
Silicon	300 µm	ρ=2330 kg/m^3, c_p=7526 m/s, c_s=4346 m/s
Gold (Electrical connection)	30 µm	ρ=19700 kg/m^3, c_p=3240 m/s, c_s=1200 m/s
Buffer epoxy	30 µm	ρ=2220 kg/m^3, c_p=2613 m/s, c_s=1289 m/s
Conductive glue	Backing: 40 µm Matching: 20 µm Top of Matching: 7 µm	ρ=3330 kg/m^3, c_p=1873 m/s, c_s=970 m/s
PZT CTS3203HD	100 µm	ρ=7820 kg/m^3 c_{11}=137, c_{12}=88, c_{13}=92, c_{33}=126, c_{44}=22, c_{66}=25 MPa ε_{11}=1306, ε_{33}=1200 C/Vm e_{15}=16, e_{31}= 9, e_{33}=22 C/m^2
Aluminium (ground connection)	7 µm	ρ=2690 kg/m^3, c_p=6306 m/s, c_s=3114 m/s

Table 3.4 Thicknesses and material properties used in the FEA simulations

3.3.3 Transducer Fabrication

The fabrication process of the 2D matrix on top of the ASIC was based on the PZT-on-CMOS integration described in [31]. Briefly, the bond pads on the ASIC that are used to electrically connect each individual element were arranged in the same configuration and with the same pitch as the transducer matrix layout (Figure 3.6(a)). Metal studs were applied on top of the bond pads and the gap in between was then filled with nonconductive epoxy (5.8 MRayl, Oldelft B.V., Delft, The Netherlands). The excess epoxy was grinded down to expose the metal and form electrical contacts. A next layer of conductive glue (6.2 MRayl, Oldelft B.V., Delft, The Netherlands) was used to electrically connect the back electrode of the PZT to the electrical connections on the ASIC. This procedure is very delicate since the conductive glue should not cover the five bond pads (red squares in Figure 3.6(b)) that will be wire bonded later on for electrical connection.

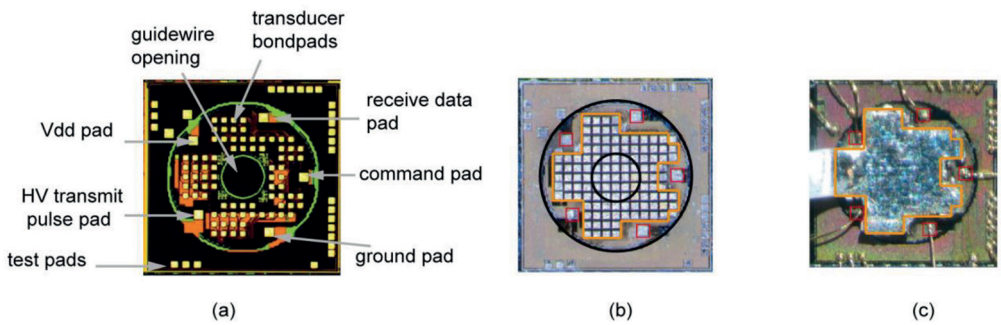

Figure 3.6 (a) ASIC micrograph, (b) matrix array on top of the ASIC after dicing; (c) matrix array after ground foil application and wire bonding. Bond pads for the cables are highlighted in red, whereas the transducer aperture is delimited by orange lines.

The individual PZT (CTS3203HD) elements were cut with a dicing saw until the buffer layer and the kerfs were left void. The entire matrix was then covered with a ground foil to create a common ground electrode for all the elements. Due to the fabrication process, diced transducer elements without electrical connection were also present in the inner hole reserved for the guidewire (Figure 3.6(b)). An extra step should be considered in the future to remove these elements when integrating the transducer in a catheter with a guidewire, ideally employing laser cutting techniques to minimize the damage to those elements located at the edge of the inner hole. The chip with the transducer was then mounted on a custom printed circuit board (PCB) for testing purposes and from the five bond pads on the ASIC, 18-µm-thick aluminium wire bonds were used to provide electrical connection to the PCB (Figure 3.6(c)).

3.3.4 Measurement Set-up

The measurement set-up is depicted in Figure 3.7. A small water bag made of acoustically transparent material was placed on top of the 2D FL-IVUS transducer, which was mounted on the PCB.

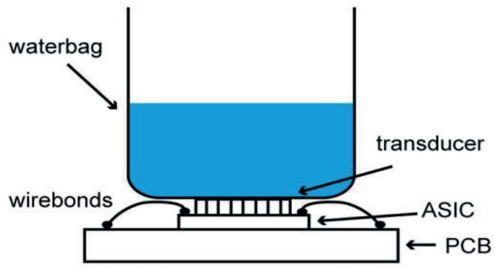

Figure 3.7 The measurement set-up.

To characterize the TX elements in terms of transmit sensitivity, bandwidth, center frequency and directivity a 75 μm needle hydrophone (SN1302, Precision Acoustics, Dorchester, U.K.) was placed in the water bag above the transducer using a positioning stage (Newport Corporation, Irvine, CA, USA) that allowed to place the hydrophone accurately 6 mm away from the transducer surface.

Each transducer element was excited with a pulser (AVIR-4D-B, Avtech Electrosystems Ltd, Ogdensburg, New York, USA) that was manually programmed to generate a unipolar pulse with a width of 25 ns and an amplitude of 28 V, as measured on the PCB. The external transmit pulse was then delivered to the specific transmit element through the HV switches on the ASIC. The acoustic pressure recorded by the hydrophone was amplified by a 58 dB amplifier (AU1519, Miteq, Long Island, New York, USA), recorded by a digital oscilloscope (DL9710L, Yokogawa, Tokyo, Japan) and transferred to a PC. To acoustically characterize the center frequency and bandwidth of the RX elements, the hydrophone was replaced by a tungsten wire (50 μm) that was mounted parallel to the surface of the transducer. Pulse echo measurements were performed with all the TX elements excited simultaneously, whereas the signals received from each RX element were recorded one by one. The transmit pulse was the same as in the hydrophone measurement except that the switches on the ASIC connected the external pulse to all the transmit elements simultaneously. The echo reflected back from the wire was converted by each element into an electrical signal that was transferred via a multiplexer to the AFE. The received signal was amplified by 18 dB through the PGA and stored on the PC. For both the TX and RX measurements, the signal stored on the PC was digitally filtered with a 5–30 MHz passband filter. To identify the functional elements, for each A-line, we computed the SNR as the ratio of the RMS amplitude value in a region including the transducer element signal over the RMS amplitude in a region without the element signal. The elements with an SNR more than

6 dB below the mean value were identified as not working, hence they were not considered further in the analysis.

To measure the receive sensitivity, a flat steel plate was placed in the water bag on top of the transducer and pulse echo measurements were performed transmitting with a single TX element and receiving with the neighboring RX element. The output signal V_{out} of the receive element can be expressed as:

$$V_{out}=P_{in}S_{rx}G$$

where P_{in} is the acoustic pressure at the element, S_{rx} is the element receive sensitivity and G is the electric circuit gain. To decouple the performance of the RX element from the performance of the receive electronics on the ASIC, we first computed the transfer function of the AFE using the response measured on one of the test inputs available on the ASIC (Figure 3.6(a)), while keeping the RX elements disconnected from the AFE. Using an arbitrary waveform generator (33522A, Agilent, Santa Rosa, CA, US) and a manual step attenuator (355D, Agilent, Santa Rosa, CA, US) set to 20 dB, we applied to the test input 3-cycle sinusoidal burst signals with a frequency varying from 10 to 20 MHz and with 4 different peak-to-peak amplitudes (50, 100, 200 and 500 mV). Since the LNA chosen for the ASIC was a trans-impedance amplifier, an on-chip resistor was implemented to convert the external test voltage signal into a current. Both the input and output voltages were recorded through the oscilloscope. The ratio between their amplitudes was used to compute the analog gain at different frequencies, obtaining the transfer function of the electric circuit chain. Based on that, we divided the pulse-echo signal recorded from the flat steel reflector by the AFE gain, yielding the current signal out of each transducer element. The measured current was then compared to the theoretical result computed through PZFlex simulations.

We also measured the input referred noise spectrum of the analog receive chain and we compared it to the simulated value from the SPICE-type simulator. Additionally, by sweeping the test input signal from 1 nA to 6 μA we computed the dynamic range under the three gain settings of the PGA available.

To test the imaging capabilities of the matrix transducer, three needles with steel spheres at the tip were placed in the water bag at different distances from the transducer surface and 3D FL imaging was performed with only 4 cables interfacing the 16 TX elements and the 64 RX elements. The synthetic aperture imaging scheme was as follows: each of the 16 TX element was excited individually and the echoes received by the 64 RX elements were acquired in 64 successive pulse-echo sequences. The resulting RF lines were beamformed resulting in a low resolution volume for each transmit element. The final volume was obtained by averaging the 16 low resolution volumes.

Images were created by beamforming the received echoes by the traditional delay-and-sum (DAS) approach and by coherence factor (CF) weighting [84] applied to the delayed lines before summation. We then compared the measured -6 dB lateral width to the values obtained from Field II simulations.

3.4 TRANSDUCER PERFORMANCE EVALUATION

3.4.1 Transmit Characterization

The simulated transmit acoustic pressure wave obtained in PZFlex is shown in Figure 3.8(a), whereas Fig. 3.8(b) shows the pressure wave measured with the hydrophone for a representative TX element. The measured SNR (Figure 3.9(a)) together with the center frequency and -3dB bandwidth of each TX element (Figure 3.9(b)) demonstrate the functionality and the low variation across the 16 TX elements. Figure 3.9(c) shows the measured directivity of five transmit elements together with the averaged directivity pattern. The -6 dB angle was measured to be approximately ±30°. Table 3.5 compares the average values from the measurements to the simulated values in terms of center frequency, bandwidth and peak-to-peak pressure at 6 mm, showing good agreement between the values. Based on the measured pressure and the input voltage amplitude, we estimate an average transmit sensitivity of 0.4 kPa/V at 6 mm. From the PZFlex simulations we estimated an output pressure of 50 kPa/V at the surface of one element, in agreement with previous works [38,85-87].

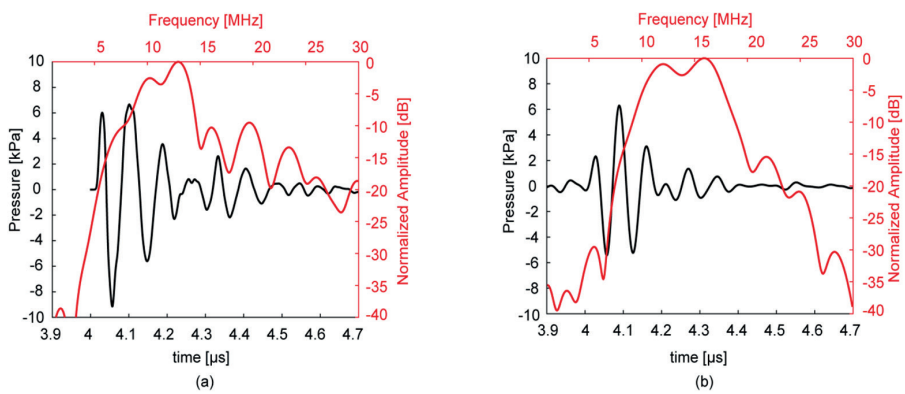

Figure 3.8 Transmit pressure at a depth of 6 mm and the corresponding spectra from FEM simulations (a) and from measurements of one TX element (b).

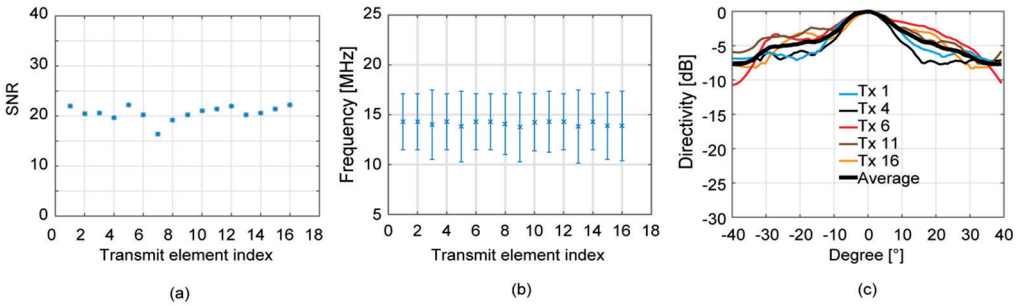

Figure 3.9 Measured SNR (a) and center frequency with -3 dB bandwidth (b) across the 16 TX elements. Directivity for five transmit elements and average directivity pattern (c).

Table 3.5 Transmit Performance

	Measurement		Simulation
	mean	STD	
f_c [MHz]	14	0.2	13
BW_{-3dB} [%]	44	5.4	38
Pressure peak-to-peak @ 6 mm [kPa]	11	1.6	17

3.4.2 Receive Characterization

Figure 3.10(a) shows the SNR for all the 64 RX elements as computed from the pulse-echo measurements using the tungsten wire. The four values marked in red correspond to the elements having an SNR more than 6 dB below the mean value. Figure 3.10(c) shows that these elements are located at the edges of the transducer aperture, which is the most critical area in terms of mechanical stability. The poor performance of these elements can be attributed to the fabrication process, which requires removal of any epoxy residue from the area of the five bond pads. This process is presently difficult to control and can easily lead to damages of the elements on the edges.

Figure 3.10(b) shows, for the remaining 60 RX elements, the center frequency and -6 dB bandwidth. The average center frequency is 14 MHz and the average -6 dB bandwidth is 42%, in agreement with the values obtained for the TX elements. RX elements with index 19 and 57, although having SNR values close to 20 dB, have quite narrow bandwidth (less than 20%), which could be caused by defects in the material layers, since also these elements are located at the edge (Figure 3.10(c)).

PZFlex simulation results showed an element impedance of approximately $5\ \mathrm{k}\Omega$ at resonance. For the AFE the SPICE-type simulator showed an input impedance of approximately $2\ \mathrm{k}\Omega$ at resonance. With these impedance values, more than 70% of the signal can be read-out by the

AFE, which is acceptable since the attenuation can be compensated by the PGA in the AFE. The RC equivalent circuit that was fitted to the simulated impedance of the AFE resulted in a resistance and capacitance value of $8.05\ \mathrm{k\Omega}$ and $6.45\ \mathrm{pF}$, respectively. These values were used in PZFlex for the receive sensitivity computation.

To compute the receive sensitivity we first characterize the gain of the receive signal chain with the PGA set to 18 dB (Figure 3.11(a)). The average gain at the center frequency (14 MHz) is 111.6 dBΩ. We then compute the pulse-echo peak-to-peak voltage amplitude obtained from the steel plate by transmitting with each TX element and receiving with the closest RX element. The voltage amplitude is then corrected for the electronic transfer function in receive giving the peak-to-peak current values shown in Figure 3.11(b), with an average value of 3 μA. The simulated current through the element for the same pressure load as in the measurements and with the element electrically loaded by the equivalent model of the front-end receiver input impedance is 2.9 μA. The simulated and measured current values are in a very good agreement. Therefore, we estimate the (electrically-unloaded) receive sensitivity based on simulation results, since PZFlex allows to model the element in unloaded condition and to compute the voltage over the element for a certain input pressure. The receive sensitivity value thus found is $3.7\ \mu\mathrm{V/Pa}$.

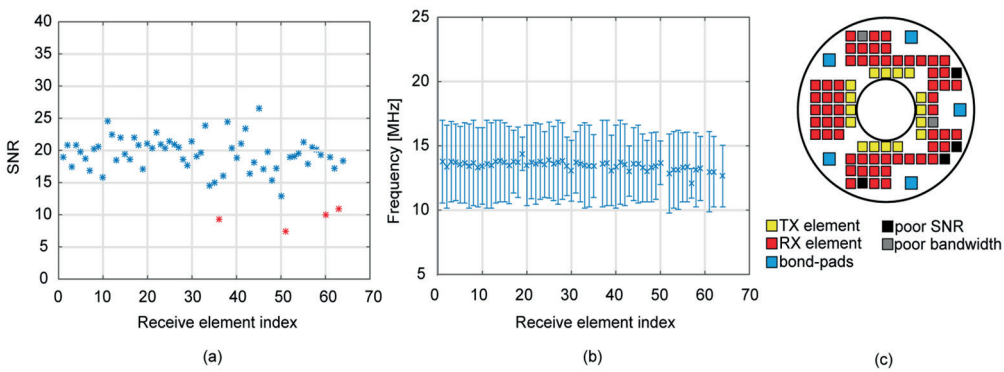

Figure 3.10 Receive pulse-echo measurements with a tungsten wire: (a) SNR values for each receive element with defective elements marked in red; (b) Center frequency and -6 dB bandwidth across the receive elements (excluding the elements with low SNR). (c) Location of the defective elements in the transducer layout.

We also simulated and measured the input referred noise of the analog receive signal chain (Figure 3.12(a)). The measured integrated noise within the bandwidth of 10 MHz to 16 MHz is around 2.53 nA, in good agreement with the simulated value of 2.3 nA. The transducer in-band rms noise is around 4.4 nA, hence dominating over the AFE, as desirable. The overall noise figure is approximately 1.2 dB. Considering the transducer element impedance at resonance (approx. $5\ \mathrm{k\Omega}$) and the element receive sensitivity, the expected minimum detectable pressure

is approx. 10 Pa. Figure 3.12(b) shows the dynamic range for the three gain settings of the PGA The minimum detectable signal can be obtained at the 0 dB cross point in the lowest gain setting and the maximum signal that the circuit can handle can be obtained at the SNR saturation cross point in the highest gain setting. Therefore, the dynamic range is approximately 55 dB.

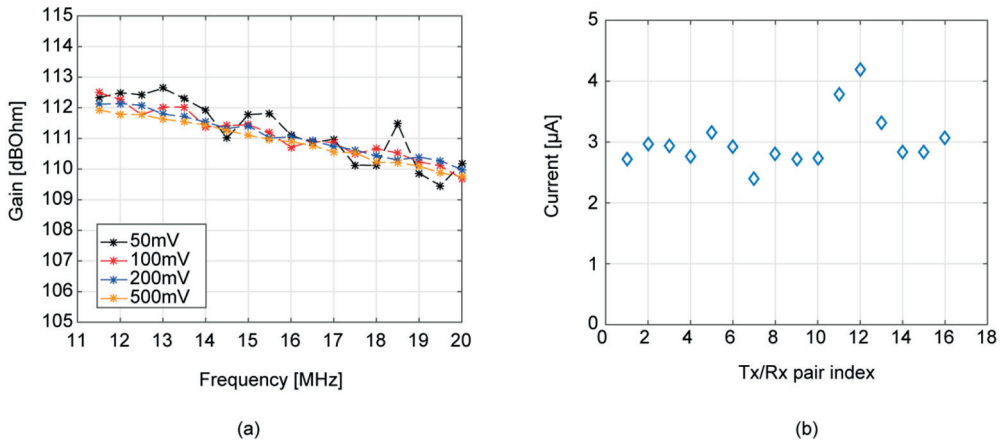

Figure 3.11 (a) The analog front-end gain of the receive chain over frequency for different amplitude settings with the programmable gain (PGA) set to 18 dB. (b) Peak-to-peak current amplitude over the elements for pulse-echo measurements where each of the TX elements transmits individually and the closest RX element is considered in receive.

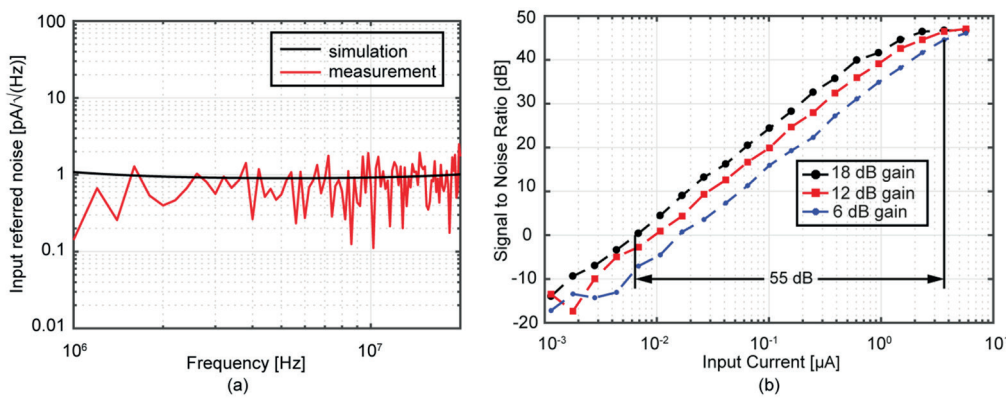

Figure 3.12 (a) Simulated and measured input referred noise over frequency of the AFE and (b) dynamic range for different gain settings of the PGA.

3.4.3 Imaging

Figure 3.13 (a) shows the maximum projections along y and x of the 3D image of the three spheres obtained using DAS, whereas Figure 3.13 (b) shows the maximum projections for the image obtained using the CF method.

For the scatterer at 6.5 mm the -6 dB lateral width is 560 µm using standard DAS, in agreement with the value obtained from the simulated Field II image (Figure 3.4(d)). By implementing the CF method, the -6 dB lateral width is reduced to $320\ \mu m$. Overall, the image obtained using the CF shows fewer artifacts and better resolution. The 3D rendering of the three spherical targets is shown in Figure 3.13 (c).

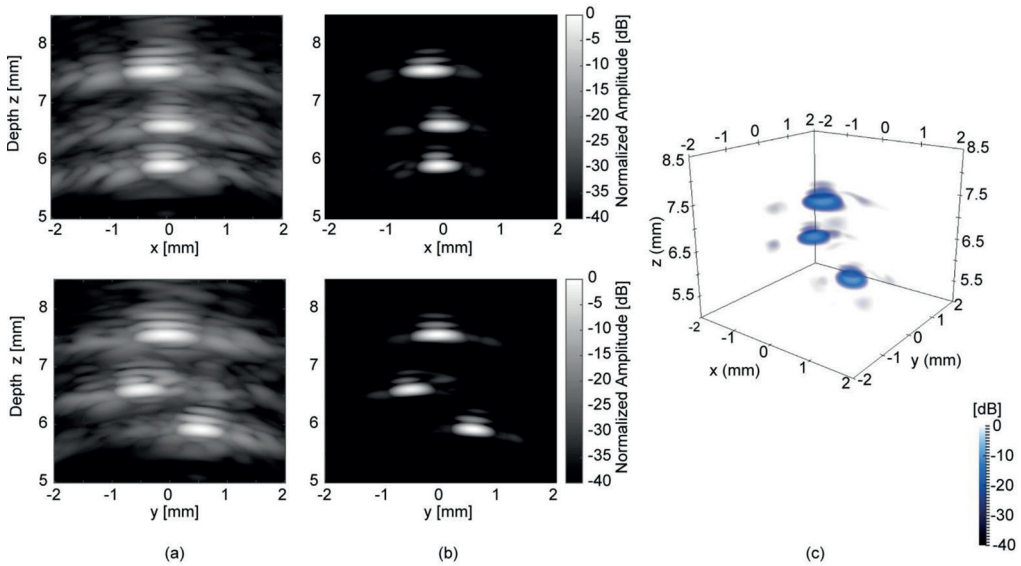

Figure 3.13 Maximum projections along y and x from 3D FL images using (a) DAS and (b) CF; (c) 3D rendering of the three spheres obtained with the CF method.

3.5 DISCUSSION AND CONCLUSION

In this work, we have presented a 14 MHz 2D matrix ultrasound transducer for FL-IVUS imaging that is integrated with a front-end ASIC requiring only four cables. We first investigated potential transducer designs using Field II. The design with the transmit elements around the inner hole and the receivers on a regular grid pattern (design **C**) shows good performances with low side-lobe levels. Since this design can be manufactured using well-established dicing technology, we opted for it and further adjusted it to accommodate the five bond pads required to connect four cables (with the fifth pad connected to the ground shield). The switches and multiplexer on the ASIC allow to transmit with one or multiple TX elements, whereas the received signal can be acquired with one RX at the time. Considering that the maximum imaging depth required for FL-IVUS is ~10 mm [72], a full synthetic- aperture scheme can be achieved with volume frame rates on the order of 100 Hz, which is adequate for real-time imaging of CTOs.

We have successfully manufactured the complete transducer on top of the ASIC and characterized it acoustically both in transmit and in receive. Fairly good agreement is present between the simulated and measured results for the transmit and receive behavior. Despite inaccuracies in the simulations, such as the material properties, the PZFlex model provided an acceptable estimate of the overall transducer behavior, allowing also to estimate the element receive sensitivity in unloaded conditions.

We performed imaging measurements using spherical steel reflectors, showing the capability of the device to generate 3D FL images. Artifacts behind the main signal of the sphere are visible in the images. The cause of these artifacts is the presence of the ASIC behind the transducer, which does not act as a standard backing and causes ringing. A proper dematching layer should be developed to reduce the ringing effect [88] similar to the approach in [20]. Moreover, some elements on the edges showed poor performance, resulting in low SNR and poor bandwidth. These elements are in general more prone to damage due to their peripheral location and proximity to the bondpads, which leads to mechanical instability.

The acoustic characterization and the initial imaging measurements showed promising results. In future parylene coating should be used to insulate the transducer. The thickness of this layer is of only 1-2 microns, therefore we do not expect significant changes in the acoustic properties.

Future work will also include the development of 2D matrix transducers using laser cutting technology. By laser cutting the individual transducer elements, non-gridded 2D matrix transducers with variable pitch can be achieved. This will lead to better imaging capability and reduced artifacts as shown in the simulation results for design **D** in Figure 3.2.

In conclusion, we have demonstrated the feasibility of 3D forward-looking imaging using a 2D matrix transducer with a front-end ASIC requiring only four cables. The limited ASIC dimensions and the low cable count make possible to integrate this transducer in an intravascular catheter suitable for forward-looking imaging of chronic total occlusions.

Acknowledgment

J. Janjic thanks Oldelft B.V. (Delft, The Netherlands), for providing materials for the transducer acoustic stack.

Chapter 4

Minimally Invasive Forward-Looking Ultrasound Imaging using a Novel Miniature Catheter Tip Design

Based on:

Jovana Janjic, Merel D. Leistikow, Aimee Sakes, Frits Mastik, Nico de Jong, Johan G. Bosch, Antonius F.W. van der Steen, Gijs van Soest, "3D Imaging with a single-element forward-looking steerable IVUS catheter: initial testing," *2016 IEEE International Ultrasonics Symposium (IUS)*, Tours, 2016, pp. 1-4.

Aimee Sakes, Awaz Ali**, Jovana Janjic**, Paul Breedveld, Novel Miniature Tip Design for Enhancing Dexterity in Minimally Invasive Surgery, *accepted for publication in Journal of Medical Devices*.

ABSTRACT

In the field of vascular interventions, forward-looking intravascular ultrasound transducers (FL-IVUS) are needed for better visualization of complex lesions, such as chronic total occlusions. In this work, we propose a strategy for 3D imaging using a single-element transducer and an optical shape sensing fiber (OSS) in a novel multisteerable catheter tip that has an outer diameter of 2 mm (Ø1 mm lumen) and it consists of 4 steerable segments with 2 degrees of freedom (DOF) each. We evaluate the performance of the integrated device by imaging a six-wire phantom submerged in water. While steering the catheter tip across the wires, ultrasound and OSS data are acquired continuously. We combine the distance information obtained from the ultrasound data with the tip position and direction obtained from the OSS data to reconstruct the wires in 3D space. We quantify the accuracy of the imaging technique by the distance between the wires, and find a mean relative error of 36%. We discuss how this estimate can be further improved by modifications of the probe. This proof-of-principle test demonstrates the feasibility of FL-IVUS imaging using a single-element transducer integrated in a steerable catheter together with an OSS fiber.

4.1 INTRODUCTION

Chronic total occlusions (CTOs) are complex intravascular lesions that occur throughout the arterial system and completely block the blood flow in the artery [23]. These lesions can be found in the relatively small coronary arteries, but also in the larger peripheral arteries. CTOs are challenging to treat percutaneously and the major reason for the low procedural success rate (70–75%) is the inability to cross the lesion with a guidewire. This is caused by the lack of accurate catheter steering and the lack of proper visualization of the occluded site [89]. In fact, conventional angiographic imaging and commercially available side-looking intravascular ultrasound transducers fail to provide adequate information about the best entry point or composition of the CTO.

To improve the CTO treatment and aid the crossing procedure, forward-looking intravascular ultrasound (FL-IVUS) catheters can provide useful information for intervention guidance. Intravascular imaging catheters need to be small, with practical upper limits on the diameter of 1 mm in coronary vessels and 2 mm for the larger and less tortuous peripheral arteries. Several FL transducers have been proposed and investigated in the past decades. Past designs have explored intravascular catheters with 2D beam scanning mechanisms, either by rotating a single element transducer [24,25], or by incorporation of a FL linear phased array [29,73]. However, the complex rotating mechanism makes the whole catheter bulky and unstable, and interconnection of multi-element transducers in the limited space of an imaging catheter is challenging to fabricate. Capacitive micromachined ultrasonic transducers (CMUT) have been investigated for FL-IVUS as well, offering flexibility in element shapes and layout, such as ring arrays [42,90,91]. This allows scanning of a different (more 3D-like) volume, but the devices are faced with much the same hurdles as linear arrays.

In this work, we consider an alternative strategy for 3D imaging in a FL approach. We developed a support catheter which integrates three components: a single-element ultrasound transducer mounted at the tip of the catheter, an optical shape sensing (OSS) fiber that reconstructs the 3D shape of the catheter, and a novel steering mechanism. While steering the catheter, ultrasound A-lines can be acquired and mapped to a specific position in 3D space using the information from the OSS data. To test the functionality of the integrated device, we performed a preliminary imaging test using a wire phantom submerged in water.

In the next sections, we first present the design of the multisteerable device followed by the description of the integration of the ultrasound transducer and the OSS fiber. We then present the imaging experiment and the results obtained.

4.2 THE MULTISTEERABLE TIP

4.2.1 Tip Design

The multisteerable instrument tip, named *Accura*, has been developed at Delft University of Technology based on the patented cable-ring mechanism [92,93] and an early mutlisteerable device named *Multiflex* [94]. Briefly, the cable-ring mechanism employs two concentric coil springs and a ring of cables in between to achieve tip deflection. This mechanism is suitable for steering multiple, stacked segments as demonstrated in the *Multiflex* device, where five segments with an outer diameter of 5 mm and an inner lumen of 1 mm enable 10-DOF motion. Moreover, in the *Multiflex* device, the spring coils are replaced with rigid incompressible components increasing the tip stiffness.

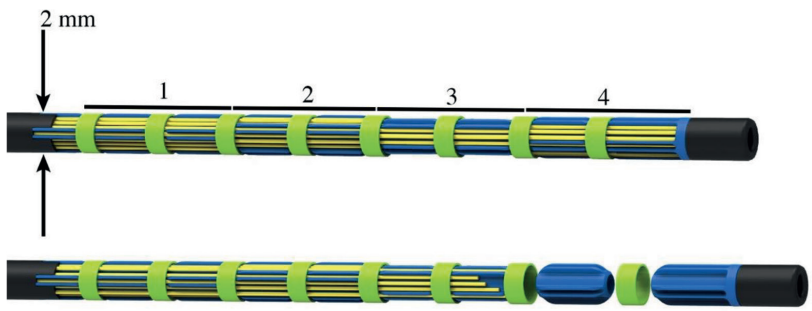

Figure 4.1 Schematic Illustration of the Multisteerable Tip of *Accura*. The tip of *Accura* has and outer diameter of Ø2 mm and consists of four 2-DOF steerable segments; giving a total of 8 DOF, allowing for forming complex shapes and single radius curves with a total curve angle of up to 90°. Each steerable segment consists of two rounded slotted cylinders (blue) and two rings (green) in which the rounded elements rotate; forming ball-and-socket type joints. The slots in the blue element allow for the attachment of four Ø0.2 mm stainless steel cables (yellow) using glue and provide cable guidance.

The novel multisteerable tip *Accura* has a smaller diameter (Ø2 mm, see Figures 4.1-4.2), reduced number of components and improved manufacturability compared to the *Multiflex* device. *Accura* contains four 2-DOF steerable segments, resulting in an 8-DOF multisteerable tip. Each steering element allows for 22.5° deflection, allowing for motions along complex curvatures and single radius curves with a total curve angle of 90°, which is comparable to currently available steerable instruments. Each steerable element (see Figure 4.1) consists of two rings (Ø2 mm, green in Figure 4.1) and two rounded slotted cylinders (Ø2mm, $Ø_{lumen}$ =1 mm, blue in Figure 4.1). Every other slotted cylinder is connected to four Ø0.2 mm stainless steel cables (yellow in Figure 4.1), giving a total of 4×4 = 16 steering cables. In Figure 4.1, *Accura* is illustrated forming a 90° single-radius curve, a complex S-curve in one plane, and a complex curve in 3D.

In comparison to *Multiflex*, the segmented structure in *Accura* has been simplified in three ways: 1) the pill-like structure, in the old design consisting out of three elements, is now made out of one single grooved part combining cable alignment with fixation, 2) the holes for cable alignment and the spherical recesses present in the *Multiflex* design are removed, and 3) the outer spring is removed as the relative stiffness of the used stainless steel cables, as compared to their free length, is in this miniaturized design so high that they will stay within the grooves even at the maximum deflection, requiring no need to cover them and limit their outward motion (see for example Figure 4.2). These simplifications allow for easier manufacturability at an extremely small size and a substantially higher aspect ratio between lumen and outer diameter: from 5:1 in *Multiflex* to 2:1 in *Accura*. As a result, *Accura* is to our knowledge world's thinnest multisteerable 8-DOF MIS instrument [95,96].

Figure 4.2 Multisteerable Tip of *Accura* illustrating different curvatures. Top: Complex single-plane curve side view. Middle: Single-plane 90° single-radius curve top view. Bottom: Complex 3D-curve side view. The match is illustrated for scale purposes.

4.2.2 Controlling the Multisteerable Tip

Enhancing the steerability of a multisteerable instrument increases its complexity, especially when multiple DOF need to be controlled simultaneously [97]. In order to explore the possibilities of the *Accura* mechanism, the multisteerable tip was combined with a rigid hollow shaft (Ø2 mm, L=200 mm) and an experimental steering unit (see Figure 4.3). The steering unit allows for precise and independent control of all the steering segments in the tip using four individual control elements (one for each element) and can be easily fastened to a standard metric breadboard or optical table. In each of the control elements four steering cables are connected using a dedicated clamping mechanism (red and green in Figure 4.4). Each control element independently controls the sideways and upwards/downwards motion of one segment using two "dials" (green and blue in Figure 4.4). The dials also incorporate a locking mechanism (purple in Figure 4.4) to lock the tip position in place.

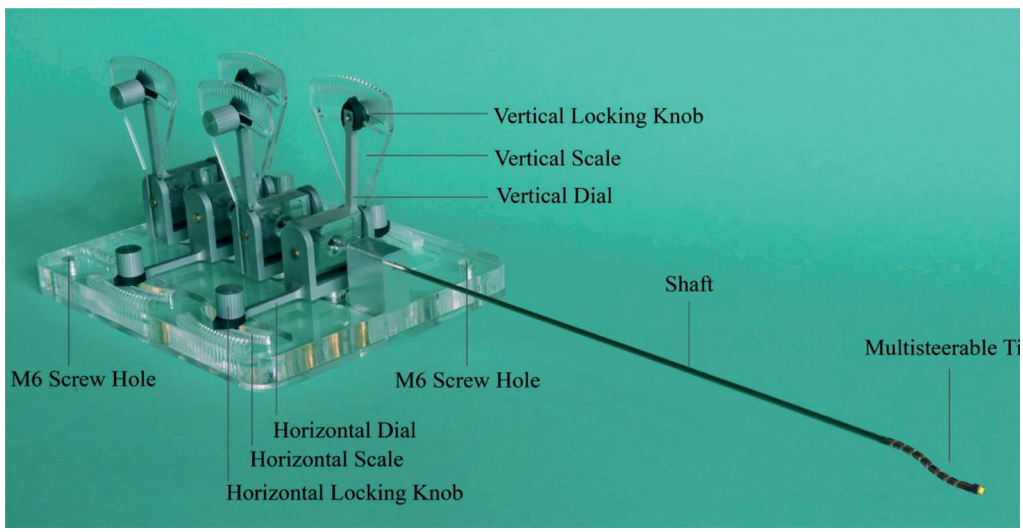

Figure 4.3 Total *Accura* Prototype. The *Accura* steering unit is designed to be easily attachable to a breadboard or optical table using two M6 screws. Each segment is controlled individually using 4 control elements. Each element can be locked individually to fixate the tip at any given shape or allow for a scanning motion. Amplification is minimized to allow for direct and precise control of the tip

4.2.3 Bending Stiffness Determination

While performing medical procedures, high bending stiffness is required to prevent parasitic tip movement by external forces and unwanted tip deflection. In order to determine the bending stiffness range of *Accura*, a proof-of-principle experiment was conducted with the cable tension set to 0 and 0.5 N (see Figure 4.5). A lateral force (F [N]) was applied to the tip using a mass of 2, 5, 10, and 15 grams. Subsequently, the lateral deflection (δ [mm]) was measured using a laser interferometer (*OptoNCDT 1402*, Micro-epsilon, maximum resolution 0.6 µm). Each measurement was performed 3 times. From this data, for each of the two cable pretensions (i.e., 0 N and 0.5 N), the overall bending stiffness was calculated by dividing the exerted force

F [N] by the deflection δ [mm] of the steerable tip. At the 0 N cable pretension, a bending stiffness of approximately $5.0 \cdot 10^{-3} \pm 0.6 \cdot 10^{-3}$ N/mm was measured. The bending stiffness could be increased to approximately 0.10 ± 0.01 N/mm at a cable tension of 0.5 N. Note that these are approximate calculations, as we did not account for internal friction in the tip.

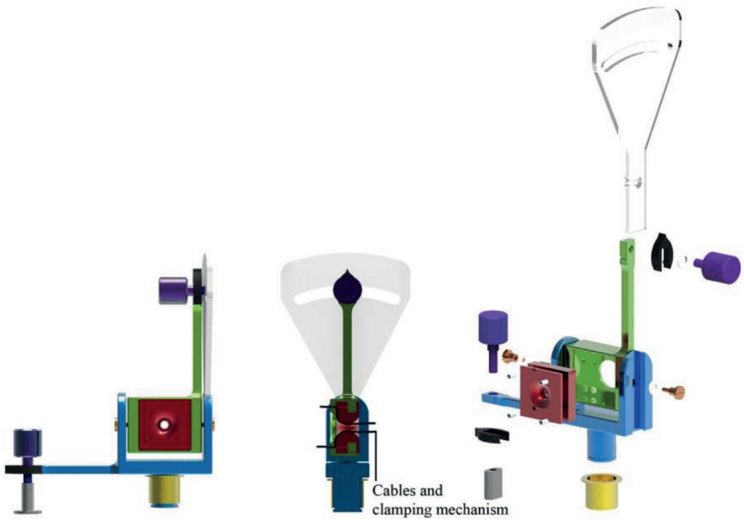

Figure 4.4 Exploded View of the Control Elements of the Handle. A control element consists of an: outer cardan part (blue; with a dial (black) controlling sideways motion), inner cardan (green; with a dial (black) controlling upwards/downwards motion), conus part (red; that guides the cables), two axles (orange), 4 screws (not indicated), and a scale (transparent). The tip position can be locked in place by tightening the knobs on the dials (purple). The cables are clamped between the inner cardan (green) and conus part (red). To allow for smooth movement of the control elements, a bearing (yellow) is placed over the main axis of the outer cardan part.

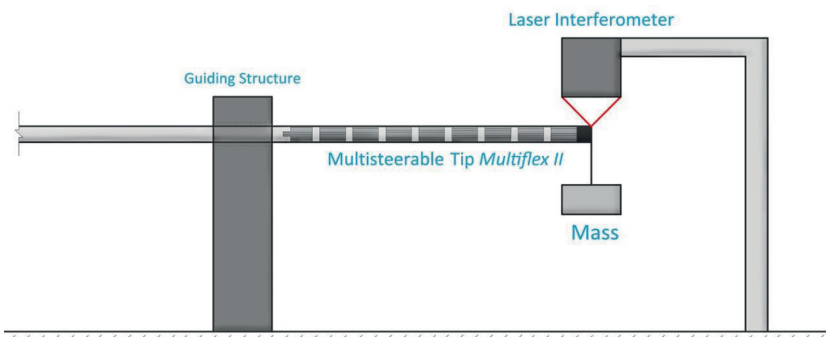

Figure 4.5 Bending Stiffness Measurement Facility. The measurement set up consisted of the multisteerable instrument, a guiding structure to prevent movement of the instrument shaft, a mass connected to the tip to exert a sideways external force on the multisteerable tip, and a laser interferometer *(OptoNCDT 1402*, Micro-epsilon) to measure the tip deflection.

4.3 ULTRASOUND AND OSS INTEGRATION

In the inner lumen of the catheter, we integrated the OSS fiber and the coaxial cable of the single-element transducer. The ultrasound transducer has a square aperture (1.4 mm side) and is embedded in a cylindrical housing mounted at the tip of the catheter (Figure 4.6) with the coaxial cable (Ø160 µm) guided through the inner lumen of the catheter. The OSS fiber (Philips Research, In-Body Systems, High Tech Campus Eindhoven) is 200 µm in diameter. To protect the fiber a hollow flexible tube (500 um in diameter) is guided all the way through the inner lumen of the catheter and its extremity is fixed at the back of the transducer housing. The fiber is then inserted in the tube and advanced manually until it reaches the back of the transducer. The fiber has 4 inner cores, with one core running along the center line and three cores wound around it in a helical fashion. Fiber Bragg gratings (FBG) are patterned along the whole length of the fiber. The fiber used in this study has 6535 sensing points, spaced by 96 µm, for a total length of approximately 63 cm. When bending the fiber, the deformation of the cores induces a variation in the refractive index of the FBG. Using optical frequency-domain reflectometry, the local strain can be measured and the 3D shape of the fiber can be reconstructed [98]. To obtain the 3D shape, the position of each sensor point is computed based on the preceding point. This means that the error in precision increases with the length of the fiber. To minimize this error, in our work we reconstruct only the last 30 mm of the fiber, which correspond to the steerable length of the catheter.

Figure 4.6 Catheter steerable tip and single-element transducer compared to a match.

4.4 IMAGING EXPERIMENT

The integrated device is tested by imaging a wire phantom submerged in a water tank. The wire phantom (Figure 4.7) consists of 6 parallel tungsten wires with a diameter of 40 µm. The catheter tip with the transducer is submerged in water and positioned relative to the phantom as shown in Figure 4.8.

To reconstruct the tungsten wires in 3D space, we stream the OSS and ultrasound data to the acquisition systems, while steering the catheter tip twice across the wires. The ultrasound excitation used is a 2 cycle sinusoidal pulse at 14 MHz with a pulse repetition frequency of 300 Hz, while the OSS system acquires shapes at 60 Hz and stores the data on a local computer. The total acquisition time is 60 s. We process the data in Matlab to combine the distance information from the ultrasound data and the tip position and orientation from the OSS data. First, we filter the RF ultrasound data with a bandpass filter (5–25 MHz) and average the OSS data to reduce the noise. Further, in each trace we search for the signal from the wires by computing the maximum of the correlation between the trace and the standard wire response. The wire response has been extracted from the first 2000 A-lines acquired with the transducer beam pointing at the wire, without moving the catheter. We further consider only the A-lines with a maximum correlation value above 0.5 and the corresponding lag is used to estimate the distance. We then plot the intensity values of the wires in 3D space based on their distance from the tip and the position and direction obtained from the OSS data. This leads to two clouds of points per wire, one for each crossing. Finally, the point with maximum intensity is selected from each cloud and a line is fitted through each pair.

To measure the distance between the estimated wires we define the mean direction of all the fitted lines and we compute, for each pair of points, the coordinates of the middle point. We then consider six parallel lines with direction equal to the mean direction, each passing through one of the middle points. We compute the mean average distance between the lines as an estimation of the wire distance and compare it to the expected distance based on Figure 4.7.

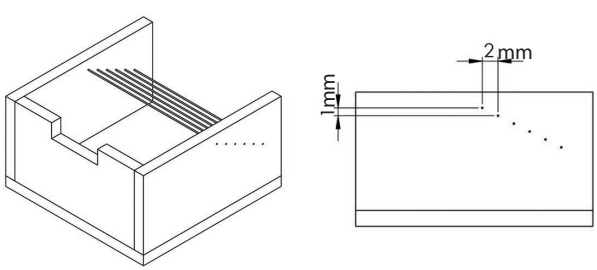

Figure 4.7 Drawing of the wire phantom with the relative wire distances.

Figure 4.9(a) shows the envelope signal for each A-line. Besides the signal from the wires, also the signal from the back plate of the phantom is visible at the beginning and at the end of the ultrasound acquisition. Figure 4.9(b) shows few example shapes of the last 30 mm of the catheter and the corresponding tip direction, while Figure 4.9(c) shows the amplitude of the signal from the wires plotted in 3D space based on the OSS data.

The reconstruction of the six wires is shown in Figure 4.10 together with the catheter tip position and direction. The estimated average distance between two wires is 1.4 mm, which compared to the distance expected from the phantom design leads to a mean relative error of 36%.

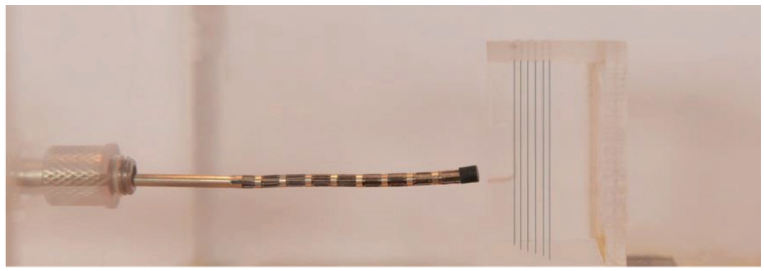

Figure 4.8 Imaging set up. The catheter tip is positioned such that the phantom is located in front of the single-element transducer.

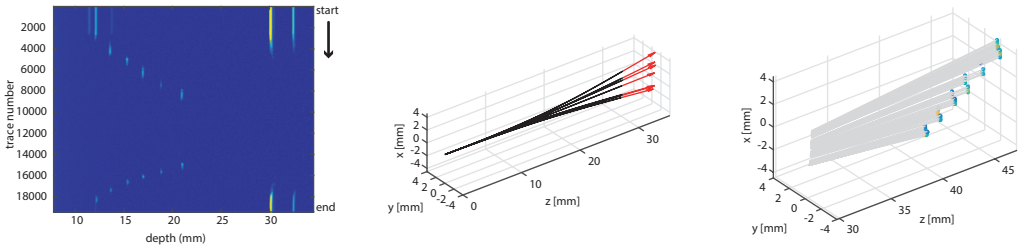

Figure 4.9 (a) Ultrasound A-line acquired while steering the catheter tip. The signal from the wires appears at depths between 10 and 20 mm, while the back plate of the phantom is visible at 30 mm at the beginning and at the end of the acquisition. (b) Examples of 3D shapes of the steerable tip (black) with direction (red arrows). (c) Intensity of the signals from the wires plotted in 3D as points together with the distance from the tip (light gray lines).

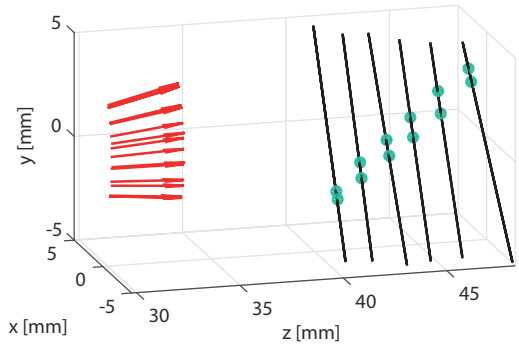

Figure 4.10 3D reconstruction of the six tungsten wires. The lines are fitted through the light green points identifying the location of the maximum intensity. The catheter tip direction, one every 20 shapes, is also shown (red arrow).

4.5 DISCUSSION

4.5.1 Intuitive Control of the Multisteerable Tip

For the clinical application of *Accura*, redesign of the steering unit is a necessity to allow for intuitive and single-handed control in a clinical setting. In a study of Chunman et al. [99], a number of control strategies are categorized into three main groups: *parallel single-segment control, serial single-segment control*, and *integrated single-segment control* (see Figure 4.11). In *parallel single-segment control*, each segment has its own controller, and each controller functions independently from the other controller. This type of control strategy was applied in the steering unit of *Accura*. In a *serial single-segment controller*, the motion of each controller depends closely on the motion of the adjacent ones, which is the case in *Multiflex's* handle. Finally, in the *integrated single-segment controller*, also called follow-the-leader controller, only the first (most distal) segment is steered, while the additional segments follow the "leader segment" passively. Even though *integrated single-segment control* may be preferred from an operator's perspective, it does not allow for actively controlling the full range of motion of the multisteerable tip. Therefore, in the future a combination of the *parallel single-segment control* and the *integrated single-segment control strategies* will be looked into, in which the surgeon only needs to steer the most distal segments while the rest of the segments remain in place, similar to the way in which a snake travels through a rocky terrain. This approach will give the surgeon the most freedom in steering the device, while at the same time not making it unnecessarily difficult by the need to control multiple segments simultaneously.

4.5.2 Multiple Functionalities in the Multisteerable Tip

As space is often limited, research should also be focused on the integration of multiple functionalities into one instrument. These functionalities should, in the authors' opinion, include: steerability, visualization, and the ability to guide a tip tool towards the operation site. First steps have been made in *Accura* to integrate multisteerability with a forward-looking ultrasound transducer and OSS fiber to visualize the operation area. The information from the forward-looking ultrasound transducer and OSS fiber can be used for navigational purposes but also for tissue characterization, which can be helpful to distinguish healthy from diseased tissues. Furthermore, since the 3D shape of the instrument's tip and shaft is reconstructed using OSS, the use of X-ray for visualization of difficult-to-reach operation areas or blood-filled spaces may be minimized, as the interventionists can obtain additional information from the combined forward-looking ultrasound and OSS data to image the surroundings and determine their position. Next to visualizing the operation area, the ability to guide a tip tool, such as a scalpel, grasper, or biopsy forceps, through the instrument, or fix one such a tool to the distal tip, will aid the surgeon in reaching the intended goal of the MIS, such as tumor removal or taking a biopsy, without the need for an additional instrument.

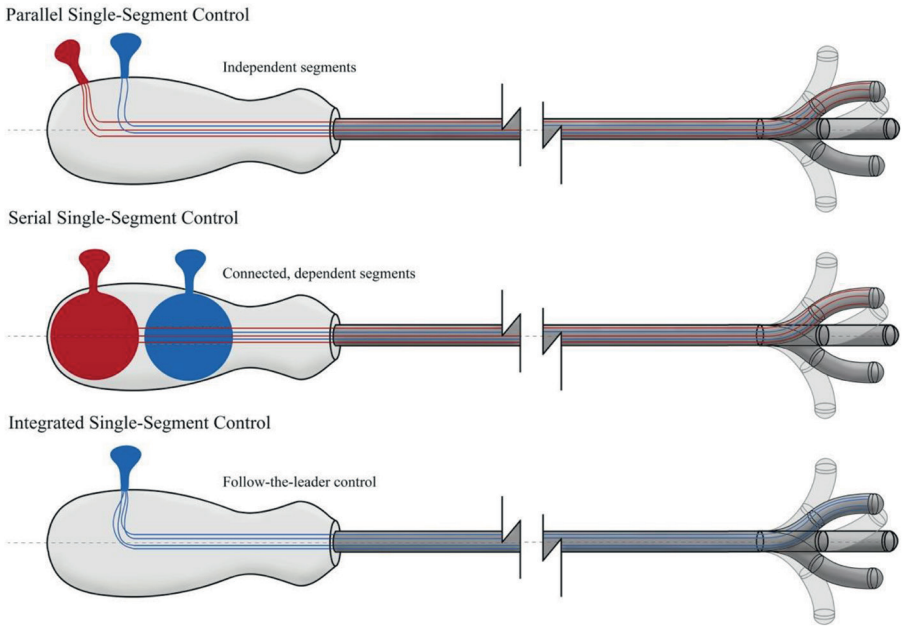

Figure 4.11 Multisteerable Control Strategies. Top: *parallel single-segment control*, in which each segment is controller by a separate controller. This way, each segment can be controlled independently. Middle: 2, in which each segment is controlled by a separate controller, but the motion of the controller (and thus the tip) is dependent on the position of the adjacent controllers. Bottom: *integrated single-segment control,* in which only the most distal segment is steered, while the other segments follow the "leader segment" passively

4.5.3 Forward-looking Imaging Limitations

We successfully reconstructed six tungsten wires using the ultrasound information from a single-element transducer combined with the 3D position information of the catheter tip obtained from the OSS data. The catheter is steered across the wires twice enabling to identify two points for each wire. By fitting a line through the points it is possible to reconstruct position and orientation of the wires.

We reconstruct only the last 30 mm of the fiber to minimize the error in shape reconstruction. Moreover, by averaging the shapes, we reduce the jittering error. However, the reconstructed wires are not all parallel. One reason for this is that the tungsten wires may not be mounted perfectly straight on the plastic support. Secondly, and more importantly, we were able only to access a limited scan pattern in this experiment, caused by difficulties in controlling the steering mechanism. The specific pattern described by the steerable catheter allowed us to cross the wires only twice with the imaging beam, without much lateral displacement. This lead to the identification of two points for each wire which are very close to each other, affecting the accuracy of the line fitting. In addition, the ultrasound transducer might insonify the wires under an angle leading to errors in the distance estimation.

Moreover, the exact position of the tip of the fiber in the catheter is very difficult to estimate and it might change during the measurement, causing errors in the position estimation of the wires in 3D space. Adjustment and improvement to the catheter tip and handle design are ongoing.

4.6 CONCLUSION

In conclusion, we have demonstrated the feasibility of performing 3D imaging with a single-element forward-looking steerable IVUS catheter using OSS. Future work will include optimization of the steering device and imaging of more complex structures like tissue mimicking phantoms. In an actual application for intra-arterial scanning, there will not be any discrete target. Rather, we will investigate how to best visualize the 3D data of complex mixed tissue by mechanically steering the ultrasound transducer across the target and integrating the ultrasound information with the OSS data. Proper visualization and mapping of heterogeneous tissue structures, such as CTOs, will aid the physician during the crossing procedure and improve the treatment success rate.

Acknowledgments
We would like to thank David de Jager, Menno Lageweg, Paul Henselmans, and Remi van Starkenburg for their help during the design process, the manufacturing, and assembly of the prototype. Additionally, we would like to thank Merel Leistikow for letting us use the OSS system at Philips and Jos van Driel for his help in setting up the bending stiffness experiment.

We also would like to thank Robert H. S. H. Beurskens and Geert Springeling for the ultrasound transducer fabrication and integration into the catheter.

Chapter 5

Sparse Ultrasound Image Reconstruction from a Shape-Sensing Single-Element Forward-Looking Catheter

Jovana Janjic, Frits Mastik, Merel D. Leistikow, Johan G. Bosch, Geert Springeling, Antonius F. W. van der Steen, Gijs van Soest, Sparse Ultrasound Image Reconstruction from a Shape-Sensing Single-Element Forward-Looking Catheter, *IEEE Trans. On Biomedical Engineering, in press*.

ABSTRACT

Objective: Minimally invasive procedures, such as intravascular and intracardiac interventions, may benefit from guidance with forward-looking (FL) ultrasound. In this work, we investigate FL ultrasound imaging using a single-element transducer integrated in a steerable catheter, together with an optical shape sensing (OSS) system.

Methods: We tested the feasibility of the proposed device by imaging the surface of a tissue-mimicking (TM) phantom and an ex vivo human carotid plaque. While manually steering the catheter tip, ultrasound A-lines are acquired at 60 Hz together with the catheter shape from the OSS system, resulting in a 2D sparse and irregularly sampled data set. We implemented an adaptive Normalized Convolution (NC) algorithm to interpolate the sparse data set by applying an anisotropic Gaussian kernel that is rotated according to the local direction of the catheter scanning pattern. To choose the Gaussian widths tangential (σ_t) and normal (σ_n) to the scanning pattern, an exhaustive search was implemented based on RMSE computation on simulated data.

Results: Simulations showed that the sparse data set contains only 5% of the original information. The chosen widths, σ_n=250 µm and σ_t=100 µm, are used to successfully reconstruct the surface of the phantom with a contrast ratio of 0.9. The same kernel is applied successfully to the carotid plaque data.

Conclusion: The proposed approach enables FL imaging with a single ultrasound element, mounted on a steerable device.

Significance: This principle may find application in a variety of image-guided interventions, such as chronic total occlusion (CTO) recanalization.

5.1 INTRODUCTION

Forward-looking (FL) ultrasound catheters can provide guidance during minimally invasive procedures, such as recanalization of arterial chronic total occlusion (CTO). In such cases, an atherosclerotic plaque has grown to completely block the vessel. Conventional intravascular ultrasound (IVUS) imaging in a side-looking geometry is of limited use. CTOs are complex lesions with heterogeneous tissue composition consisting of lipids, organized thrombus, calcium and collagen-rich fibrous tissue [23]. They can develop in the relatively small coronary arteries, but also in the larger peripheral arteries. In order to aid the CTO crossing procedure, FL ultrasound may provide useful information, such as the best entry point or local tissue composition [72, 100]. Forward-looking transducers may be beneficial for other applications as well, such as intracardiac echography for the diagnosis of cardiac arrhythmias [87,101], or guidance during transjugular intrahepatic portosystemic shunt (TIPS) procedures, where a shunt is created in the liver to decrease the high blood pressure in patients with portal hypertension [102,103] and the portal vein needs to be located under image guidance.

Catheter-based FL ultrasound technology is still in development and several concepts have been pursued in experimental settings. Early work explored single element transducers mounted on a rotating cam assembly [24,25]. This mechanism is rather complex and makes the whole catheter bulky and unstable. In other studies, linear transducer arrays have been investigated as a way to provide 2D imaging ahead of the catheter tip without mechanical scanning [29,73]. The major problems with this approach are the limited space available and the constraints in PZT fabrication that make the integration into catheters very challenging. Capacitive micromachined ultrasonic transducers (CMUT) offer a great advantage in terms of fabrication over PZT since very small dimensions and arbitrary geometries of the elements can be achieved using lithography techniques and micro-fabrication processes [37]. This technology has been used by several groups in the attempt of developing catheter-based FL ultrasound transducers [41,42,44,87,90,91]. However, integration and miniaturization of electronics remains the major problem.

In this work, we propose an alternative approach to achieve FL ultrasound imaging by integrating three components in one device: a single-element ultrasound transducer, an optical shape sensing (OSS) fiber and a catheter that can be steered along two directions in one plane. While steering the catheter, single ultrasound A-lines can be acquired at different locations together with the catheter 3D shape obtained from the OSS data. Having a single-element transducer reduces the complexity of integration, whereas the position and direction information from the OSS data allow to combine the individual A-lines in 3D space. This paper builds on an earlier initial work by our group to integrate a similar device with preliminary results on target reconstruction [104,105].

Since the steering is performed manually and is limited to specific patterns due to the catheter design, a sparse and irregularly sampled data set is obtained. To reconstruct FL images of the target from sparse data, an interpolation algorithm is required. In previous works different approaches to sparse image reconstruction have been proposed [106,107]. A method that has shown good performance is Normalized Convolution (NC) [108-110]. NC takes into account the certainty of the signal and applies a diffusion kernel to fill the empty spaces in the image. We implement an adaptive interpolation method based on NC, where the diffusion kernel changes orientation dynamically depending on the local scanning pattern of the catheter. A similar approach was used in [111] with the difference that there the diffusion kernel was adapting to the image gradient. We tested our adaptive NC method both on simulated and real data, focusing on the reconstruction of the front surface of a tissue mimicking (TM) phantom and of a carotid plaque obtained from endarterectomy.

5.2 METHODS

5.2.1 Experimental configuration

To perform FL ultrasound imaging with a single element transducer on a steerable catheter, we have developed a prototype device based on a commercially available bi-directional steerable guiding sheath (8.5 F, MobiCath, Biosense Webster). The dimensions of this sheath are suitable for peripheral vasculature applications, but exceed the allowable dimension for coronary artery access. By rotating the catheter handle (Figure 5.1(a)), the tip can be steered in two directions in one plane and by rotating the entire catheter, the steering plane can be chosen. At the tip of the catheter, which is free from steering cables, we place a single-element ultrasound transducer (Figure 5.1 (b)). The ultrasound transducer is a circular PZT element with a diameter of 1 mm and 25 MHz center frequency, mounted in a custom-made housing (Figure 5.1 (c)). The single element transducer can also be mounted on steerable catheters with smaller outer diameter. The transducer is electrically wired with a 160 μm coaxial cable that is guided through the inner lumen of the catheter. The OSS system (a research prototype developed at Philips Research, Eindhoven, NL) consists of an optical fiber with a diameter of 200 μm, connected to a scanning laser system [94,104]. The fiber has four inner cores, one along the longitudinal axis and three wound around it in a helical fashion. Fiber Bragg Gratings (FBG), which consist of periodic variation in refractive index, are patterned along the entire length of the fiber (1.8 m). Bends in the fiber induce local stretching and compression of the period of the FBG, allowing measurements of the local strain based on optical reflectometry in the frequency domain [48]. The central wavelength of the scanning laser is set to 1545 nm, and is swept over 17 nm. The spatial resolution along the sensor is 50 micrometer. The 3D shape is obtained by performing a distributed measurement of the applied strain to each of the four cores. By integrating forward along the fiber from the first sensing point, which is fixed in the reference frame, and combining the information from all four cores, the geometry of the sensor can be obtained. Since the position of each sensor point is estimated based on the previous one, the precision

of the estimation decreases with increasing length of reconstruction. Additional details about the working principle can be found in [48,49]. A helical hollow strand (HHS) tube (0.5 mm in diameter) protects the OSS fiber. The HHS tube is guided through the catheter lumen and one end is attached to the back of the transducer housing, whereas the other end is accessible to insert the fiber.

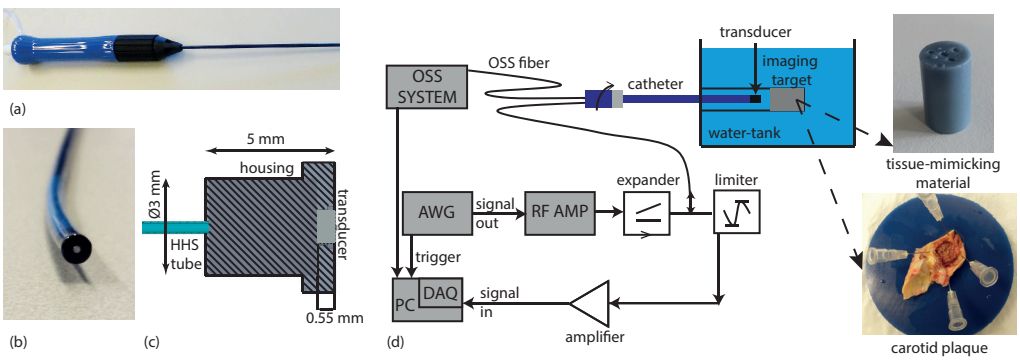

Figurre 5.1 (a) Handle of the steerable catheter (MobiCath, Biosense Webster) (b), tip of the steerable catheter with the single element transducer (inner gray circle) (c), schematic drawing of the transducer housing with the HHS tube for the OSS fiber, and (d) the measurement set-up, with TM phantom and carotid plaque.

We simultaneously acquire OSS data and US data while steering the catheter. A 2-cycle sinusoidal pulse at 40 Vpp with a center frequency of 25 MHz is sent to the transducer using a waveform generator (Tektronix, 3102) and an RF power amplifier (ENI, 310L), whereas the received signal is amplified by 40 dB (Hewlett-Packard, 461A) and digitized with a sampling frequency of 350 MHz (Acqiris, DP310). The OSS data are acquired at 60 Hz via the user interface developed by Philips, providing the total shape and curvature of the fiber. A Matlab script provides a real time feedback of the covered area by plotting the catheter tip coordinates in 2D and the corresponding ultrasound A-lines. Further signal processing and image reconstruction are performed off-line in Matlab (R2016a), using a personal computer with an Intel i7-3770, 3.4 GHz, 4-core processor. Figure 5.1(d) shows a schematic of the complete set-up used in our measurements. The imaging target is submerged in a water tank into which the steerable catheter is inserted from the side of the tank, clamped using an O-ring and guided into a plastic tube that confines and limits its movements.

As imaging target we used a tissue mimicking (TM) phantom and an ex vivo human carotid plaque (Figure 5.1(d)). The agar-based phantom has a cylindrical geometry with a diameter of 16 mm and has hollow channels running through the total length and steel spheres embedded at the surface. The *ex vivo* human carotid plaque is obtained following endarterectomy procedures, under a research protocol sanctioned by the Medical Ethics Committee of the Erasmus Medical

Center MC (MEC-2008-174). The human specimen was snap frozen in liquid nitrogen within 10–20 min following endarterectomy and stored at 80°. The tubular specimen was then thawed, cut open along the longitudinal axis, mounted on a rubber support and submerged in saline solution with the inner plaque layer facing the ultrasound probe. A 3D ultrasound image of the plaque was obtained as ground truth using a high frequency pre-clinical ultrasound scanner operated at 21 MHz (Vevo 2100 with MS250, VisualSonics Inc., Toronto, ON, Canada). In addition, we scanned the plaque with the 25 MHz single element transducer clamped to a positioning stage and mechanically scanned along a regular grid pattern with a step size of 100 μm in both x and y directions.

5.2.2 Ultrasound data processing

Each ultrasound A-line is filtered in Matlab using a Butterworth filter of order 5 with a bandwidth between 15 MHz and 45 MHz. After filtering, the envelope is computed using the Hilbert transform. We focus on the reconstruction of the surface of TM phantoms with high-intensity hard spots and low-intensity channels and on visualization of the surface of the carotid plaque. The surface is obtained from the ultrasound A-lines by intensity thresholding: for each A-line, if the signal is above the noise level, we consider the corresponding distance value as the surface location. The noise level was measured considering the average signal in the water region before the surface of the phantoms. For points where we do not find a distance value, like the phantom channels, we linearly interpolate between known neighbors. Next, we consider the envelope signal corresponding to a 400 μm thick slice of the imaged object starting from the surface and we project the envelope mean values on a 2D plane based on the tip position and direction obtained from the OSS system and based on the tip-to-target distance computed with ultrasound. At the same time, we also store the tip-to-target distance for each tip position. When computing the tip-to-target distance we apply an offset of 5 mm to take into account that the OSS fiber tip is not exactly at the same axial location as the transducer (see Figure 5.1(c)). The resulting 2D data sets form two sparse and irregularly sampled maps: one for the subsurface intensities and one for the tip-to-target distances.

5.2.3 Estimation of catheter tip position and direction

For each acquired data set, the 3D coordinates of the sensing points along the fiber and their curvature are provided by the OSS system. We use the curvature plot of each fiber shape to find the point that corresponds to the location where the catheter is clamped to the side of the water tank. At this location, a peak in the curvature is visible, due to the deformation applied by the clamping mechanism. Knowing that the clamping point is not moving, we can use it as a new reference point and reduce the reconstructed length of the fiber, thus decreasing the error in position estimation. Next, we compute the catheter tip position and direction relative to the new reference point. The obtained coordinates are further smoothed applying a spline fit in order to obtain a more regular scanning pattern and remove possible outliers.

5.2.4 Sparse data from simulated target

To simulate a sparsely sampled data test, we use a measured scanning pattern obtained from one of the OSS acquisitions and simulate an imaging target in a plane perpendicular to the mean direction of the catheter tip, at a distance of 4 mm. The simulated target consists of a regular grid of holes and strong reflectors (Figure 5.2(a)). To simulate a target that is sampled by an ultrasound transducer, we convolve the target image with the ultrasound transducer point spread function (PSF) at 4 mm (Figure 5.2(b)), which has a –3 dB diameter of approximately 500 µm. An image of the target after PSF application is shown in Figure 5.2(c). We sample the simulated target after PSF application by projecting the catheter tip position on the target plane.

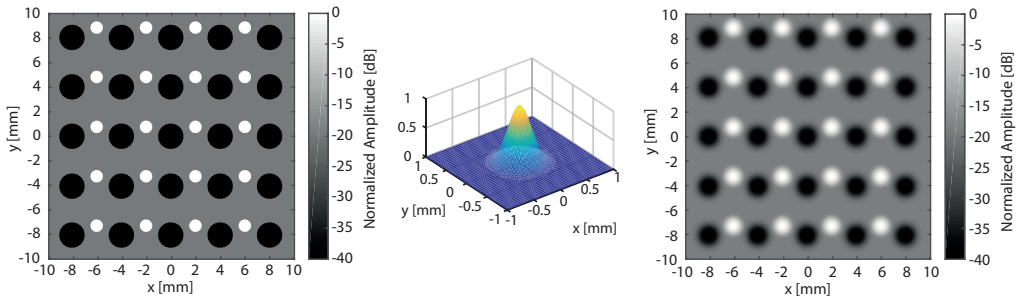

Figure 5.2 (a) Simulated imaging target consisting of a regular grid of holes and strong reflectors (b), ultrasound PSF at 4 mm (c), imaging target convolved with the ultrasound PSF at 4 mm.

5.2.5 Image reconstruction with adaptive Normalized Convolution (NC)

NC is a technique used for interpolation of sparse, irregularly sampled data based on their certainty by applying a predefined diffusion kernel [108-110]. More in detail, considering a sparse image S and its certainty map C, the normalized convolution result R is obtained as follows:

$$R = \frac{(S \cdot C) \otimes G}{C \otimes G} \tag{5.1}$$

where G is the diffusion kernel and $\otimes$ indicates convolution. The certainty map represents the certainty for the image samples, which is 1 for each sampled position and 0 everywhere else. The diffusion kernel is usually represented by the 2D Gaussian function

$$G(x,y) = \exp\left[-\left(\frac{x}{\sigma_x}\right)^2 - \left(\frac{y}{\sigma_y}\right)^2\right] \tag{5.2}$$

where the parameters σ_x and σ_y represent the width of the kernel in the x and y direction, respectively. In conventional NC the diffusion kernel is an isotropic Gaussian, with σ_x=σ_y.

In our study, the sparsely sampled data obtained from both the simulations and the real measurements are used to generate a sparse matrix image with a pixel size of 40 x 40 μm. In the simulations the sparse image contains the intensity values sampled using a measured scanning patterns obtained from one of the OSS acquisitions. For the real measurements, beside the intensity sparse map, we also define the sparse map of the tip-to-target distances. Therefore, during the scan, we accumulate the amplitude value per pixel in S_i and the distance values per pixel in S_d while keeping track of the number of measurements in each pixel of C. As diffusion kernel we apply an anisotropic Gaussian function that is rotated according to the local scanning pattern of the steerable catheter. The idea is to diffuse the sparse intensity map, the sparse distance map and the certainty map taking into account that we have a very dense sampling along the scanning path and a very sparse sampling in the other directions. The dense sampling along the scanning path is due to the high sampling rate (60 Hz) combined with the slow motion of the catheter (approximately 0.6 mm/s). More in detail, the adaptive diffusion kernel is defined as:

$$G(x_\theta, y_\theta) = \exp\left[-\left(\frac{x_\theta}{\sigma_t}\right)^2 - \left(\frac{y_\theta}{\sigma_n}\right)^2\right] \quad \text{with } (x_\theta, y_\theta) = (x,y) \bullet \begin{bmatrix} \cos\theta & \sin\theta \\ -\sin\theta & \cos\theta \end{bmatrix} \tag{5.3}$$

where σ_t represents the width of the kernel along the direction tangential to the path, σ_n represents the width of the kernel along the direction normal to the path and Θ is the angle between the direction normal to the path and the axis of the image. A schematic drawing is shown in Figure 5.3. Both the sparse map (intensities and distances) and the certainty map are locally convolved with the adaptive kernel following 5.5.1 and the resulting diffused maps are divided to obtain the adaptive NC result for both the intensities and the distances.

To find the optimal parameters for σ_t and σ_n we perform an exhaustive search using the simulated sparse intensity data. Both σ_t and σ_n are varied between 50 and 500 μm and, for each possible combination of parameters, the adaptive NC result is computed. The obtained image I_{aNC} is compared to the simulated ground truth image I_{truth} (Figure 5.2(a)) by computing the root-mean-square error on the linear intensities as:

$$RMSE = \sqrt{\frac{1}{N_{pixel}} \sum_{n=0}^{N_{pixel}-1} (I_{aNC}(n) - I_{truth}(n))^2} \tag{5.4}$$

The values of the parameters σ_t and σ_n for which we get a low RMSE, are then used in the adaptive NC to reconstruct the image of the simulated target, the TM phantom and the carotid plaque. For the TM phantom we apply adaptive NC with different combinations of parameters σ_t and σ_n, and we compute the contrast ratio CR, which is defined as [59]

$$CR = \frac{\mu_b - \mu_c}{\mu_b + \mu_c} \tag{5.5}$$

where μ_b is the average signal amplitude from the tissue-mimicking material and μ_c is the average signal amplitude in the hollow channel region.

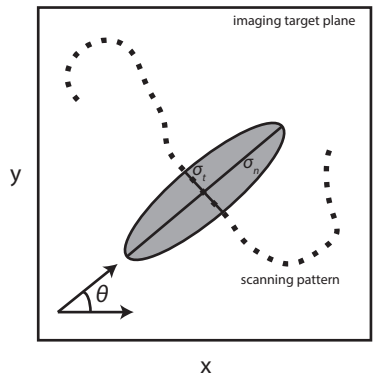

Figure 5.3 Schematic drawing of a scanning pattern (dotted line) on the imaging target plane with a rotated anisotropic kernel (gray area). Dotted line represents the scanning path, gray ellipsoid represents the diffusion kernel; σ_t=width of the kernel along the direction tangential to the path , σ_n=width of the kernel along the direction normal to the path, θ=angle between the direction normal to the path and the axis of the image.

5.3 RESULTS

Figure 5.4(a) shows a typical 3D reconstruction of the entire OSS fiber, including the portion integrated into the steerable catheter, which is clamped at the side of the water tank. The z-axis of the 3D shape reconstruction corresponds to the catheter long axis. Figure 5.4(b) shows the curvature of three different shapes acquired while manually scanning the catheter. The three curvature plots are representative of the initial, intermediate and final shape of the catheter during one acquisition. The curvature peaks around 0.9 m coincide with the catheter handle location, whereas the peak indicated by the red mark corresponds to the location at which the catheter has been clamped to the side of the water tank. Since only the tip of the catheter is steering, we use the catheter clamping point as a new reference point for the OSS reconstruction. Figure 5.4(c) shows the shapes of approximately the last 10 cm of the catheter during one acquisition, whereas Figure 5.4(d) shows the tip position and direction after spline filtering. The results presented in the following sections where achieved with a non-optimized algorithm that computes the adaptive kernel at a rate of 68 data points (tip positions with corresponding intensities) per second. Since each acquisition contains 15000 tip positions and relative ultrasound intensities, the final adaptive NC images were computed in 3 min and 40 sec.

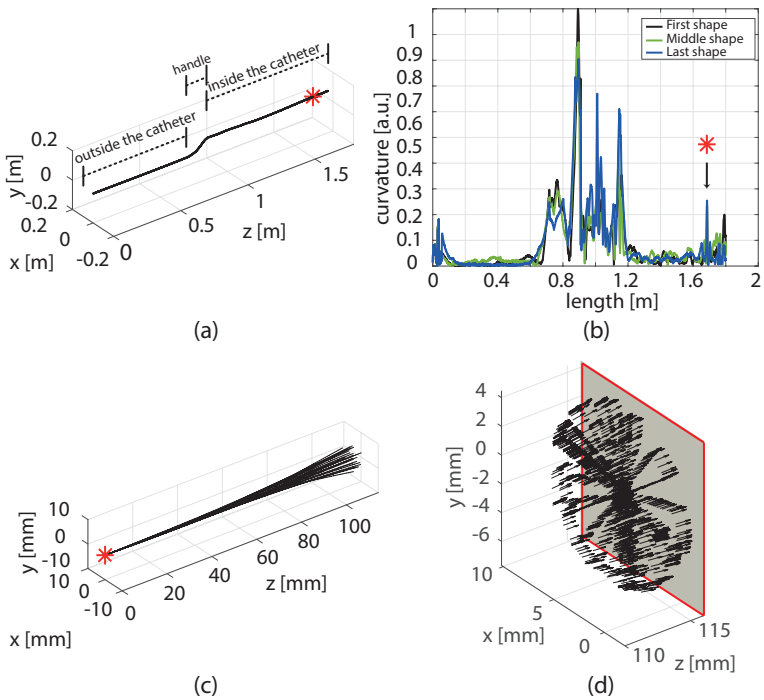

Figure 5.4 (a) A representative 3D shape of the fiber inserted into the steerable catheter (b), curvature plot for three different shapes: first, middle and last shape during one measurement (c), 3D shapes of the last 10 cm of the steerable catheter during one measurement (d), Catheter tip position and direction (black arrows) in 3D. The gray plane delineated by red lines indicates the imaging plane. The red asterisk indicates the location at which the catheter has been clamped to the side of the water tank.

5.3.1 Adaptive Normalized Convolution on simulated data: optimal parameter choice

The scanning pattern shown in Figure 5.4(d) is applied to the simulated target (Figure 5.2(c)) to obtain the sparse certainty and sparse intensity maps of Figure 5.5(a) and (b). In the resulting map, only 5% of the original image information is retained. Figure 5.5(d)-(f) show the conventional NC steps where an isotropic Gaussian kernel is applied with σ_x=σ_y=400 µm. The original simulated imaging target is also shown as a reference (Figure 5.5(c)). The optimal parameters and for the adaptive NC are found utilizing an exhaustive search. The RMSE for the different combination of parameters is shown in Figure 5.5(g). The chosen parameter combination is indicated by the white star and corresponds to σ_n=250 µm and σ_t=100 µm. The anisotropic kernel with the optimal parameters is applied to the sparse data resulting in the adaptive NC reconstruction shown in Figure 5.5(i).

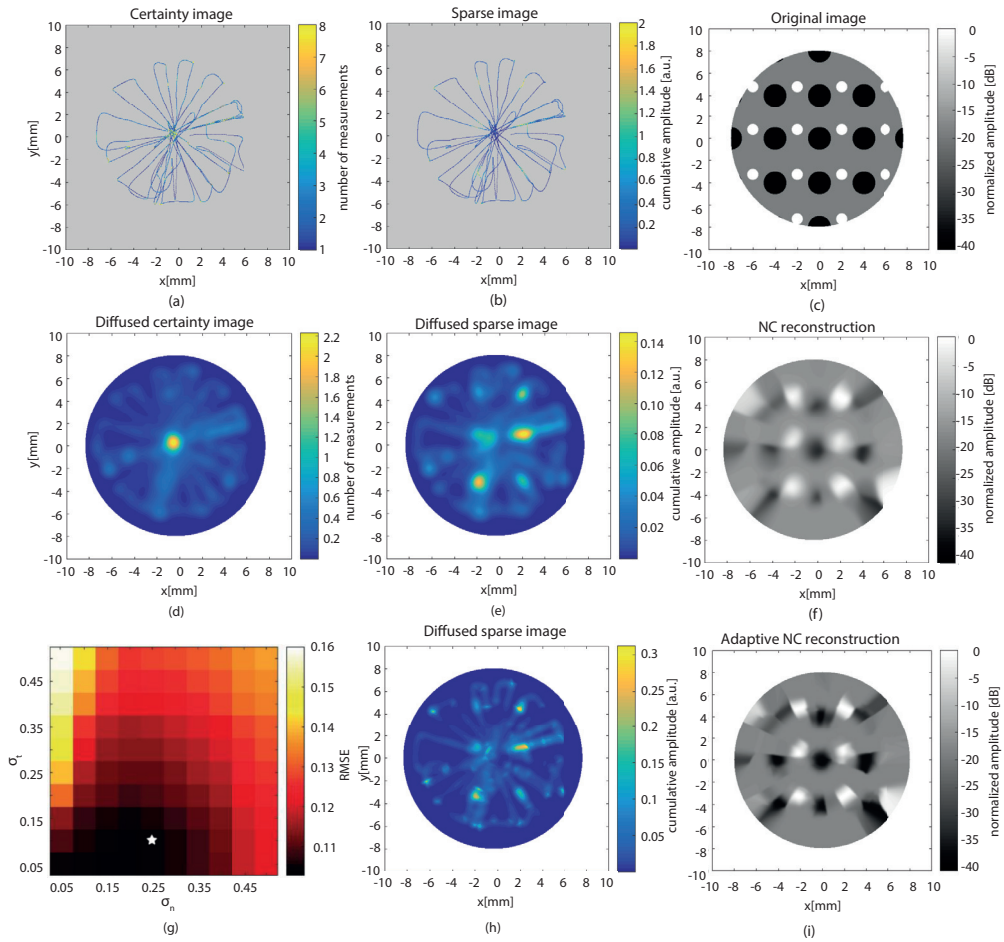

Figure 5.5 Standard NC: (a) simulated certainty image and (b) sparse intensity image, both with maximum value clipped for better visibility; (c) original image; (d) diffused certainty image and (e) diffused intensity image using an isotropic kernel with σ_x=σ_y=400 µm; (f) NC result; (g) RMSE based on linear intensities resulting from the exhaustive search for the NC parameters σ_n and σ_t. The white star indicates the chosen combination of parameters; (h) sparse intensity image diffused with the anisotropic kernel; (i) adaptive NC reconstruction.

5.3.2 Adaptive Normalized Convolution on phantom data

An example of ultrasound data obtained from the TM phantom during one measurement is shown in Figure 5.6. The data are shown after filtering and after envelope detection. The red line indicates the phantom surface. From the ultrasound A-lines shown in Figure 5.6 it is possible to see the gaps in the signal corresponding to the hollow channels (indicated by the yellow solid arrows) and strong reflections corresponding to the steel spheres embedded at the surface (indicated by the yellow dashed arrows).

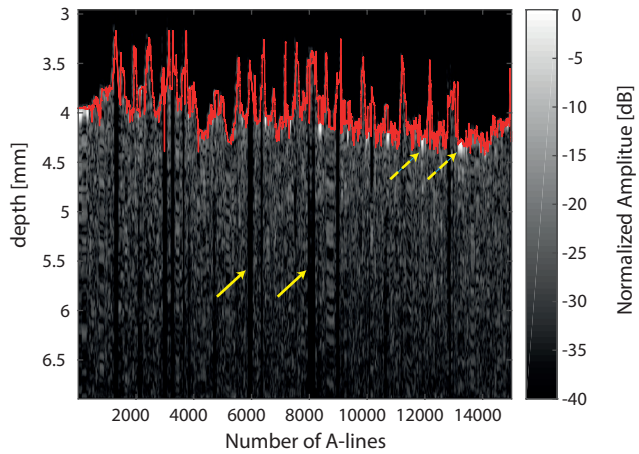

Figure 5.6 Ultrasound A-lines obtained by scanning the transducer across the surface of one of the TM phantoms. The red line indicates the phantom surface, the yellow solid arrows indicate some hollow channels and the yellow dashed arrows indicate some strong steel reflectors.

The average amplitude for each A-line over a depth of 400 μm from the phantom surface is mapped to a 2D plane representing the phantom surface, knowing the tip-to-target distance based on ultrasound and the tip position and direction in 3D based on the OSS data. The resulting average intensity image is shown in Figure 5.7(b). Figure 5.7(c) shows the corresponding adaptive NC result images with the chosen kernel parameters σ_n=250 μm and σ_t=100 μm. Both average intensity image and adaptive NC images are shown with a dynamic range of 40 dB. Next, we apply the adaptive NC reconstruction on the tip-to-target distance (Figure 5.7(d)) and, by combining the distance and intensity reconstructions, we obtain the surface plot shown in Figure 5.7(e), with most of the intensity values located in one plane, in agreement with the fact that the front surface of the phantom is flat.

To confirm the improved contrast obtained by applying adaptive NC with the chosen parameters over standard NC, we compute the contrast ratio for images obtained applying adaptive NC with different combinations of parameters and σ_n and σ_t. The result is shown in Figure 5.7(f), demonstrating that our choice of σ_n and σ_t lies in the region of highest contrast ratio. In fact, we achieved a contrast ratio equal to 0.9 by using an adaptive Gaussian kernel with σ_n=250 μm and σ_t=100 μm.

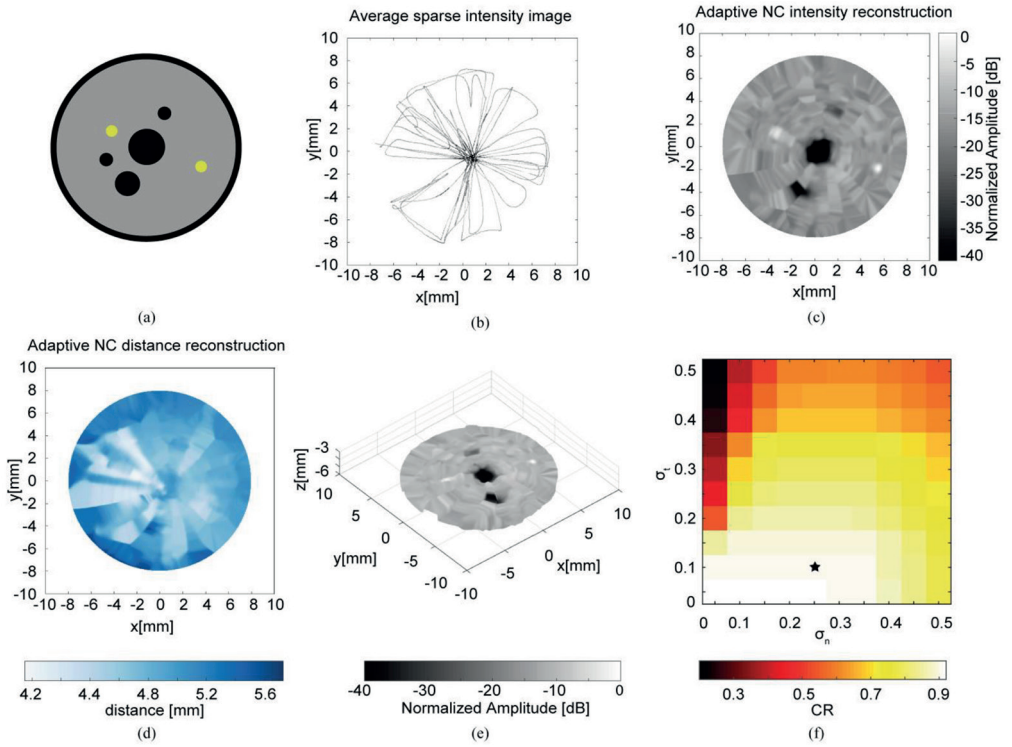

Figure 5.7 (a) Schematic drawing of the phantom surface; (b) average sparse intensity image; (c) adaptive NC reconstruction of the intensity; (d) adaptive NC result on the tip-to-target distances; (e) surface plot combining the intensity and distance information; (f) Image contrast ratio obtained using adaptive NC with different combinations of σ_n and σ_t for the TM phantom. The chosen combination of parameters is indicated with a black star.

5.3.3 Adaptive Normalized Convolution on carotid plaque data

Figure 5.8 (a) shows the area of the carotid plaque that was imaged and scanned. The yellow arrows indicate the location of calcified areas. The surface plot obtained with the Vevo 2100 pre-clinical ultrasound scanner is shown in Figure 5.8(b). Figure 5.8(c) shows the image obtained by scanning the 25 MHz single element transducer over a regular grid pattern mechanically translating the transducer. Figure 5.8(d) shows the sparse distance map, whereas Figure 5.8(e) shows the intensity sparse map. Both the sparse maps are obtained by manually steering the catheter with the 25 MHz transducer at the tip and acquiring OSS data, similarly to the TM phantom measurements. The result of applying the adaptive NC on both the tip-to-target distances and on the intensity values is shown in Figure 5.8(f).

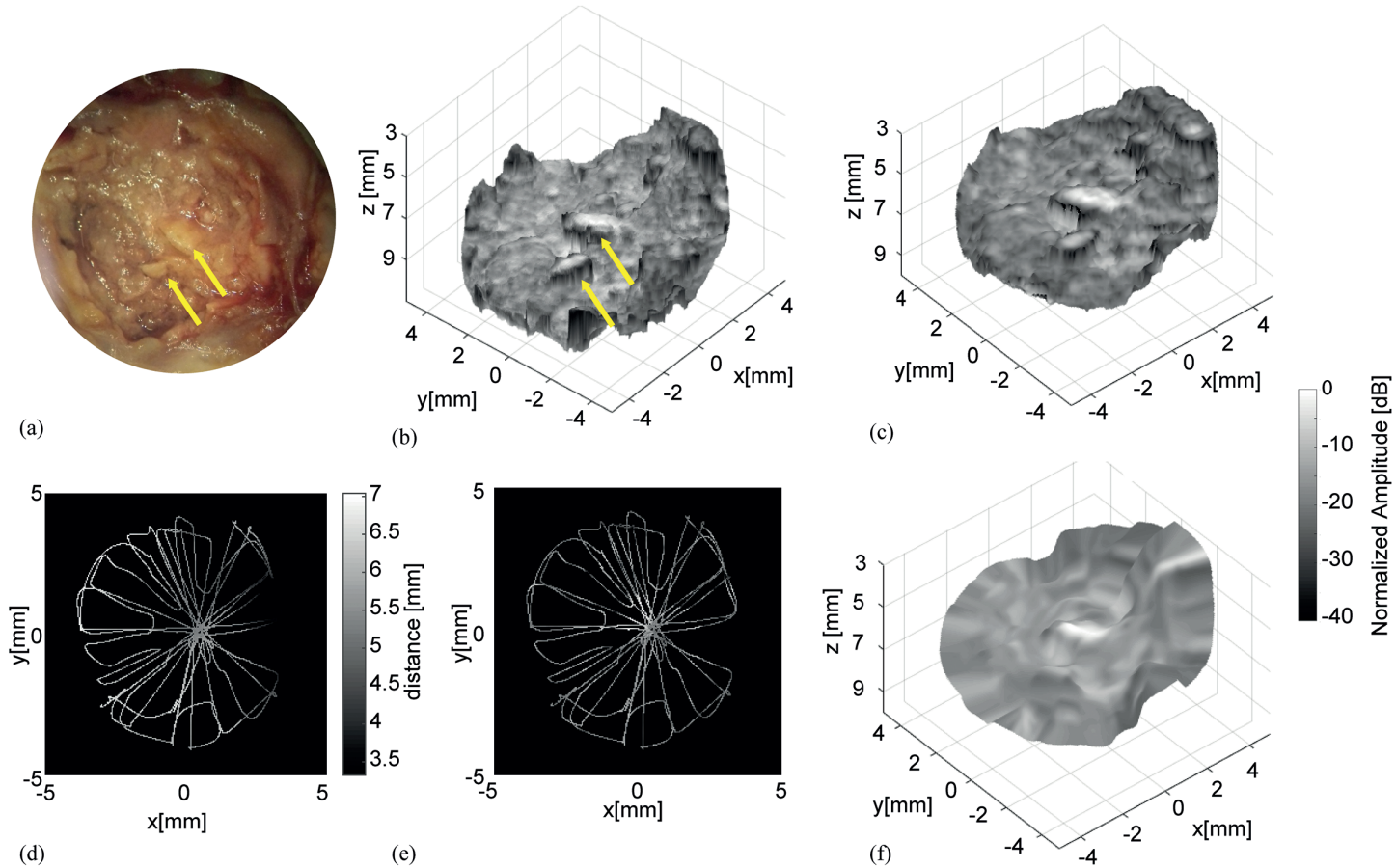

Figure 5.8 (a) picture of the imaged portion of the carotid plaque with yellow arrows indicating calcium; (b) surface reconstruction using the Vevo 2100 scanner with a 21 MHz linear array, (c) surface reconstruction obtained by mechanically scanning the 25 MHz single element transducer on a regular grid pattern; (d) sparse distance map and (e) sparse intensity map obtained by manually scanning the 25 MHz single element transducer mounted on the steerable catheter; (f) surface reconstruction of the after adaptive NC on both the sparse distance and the intensities values.

5.4 DISCUSSION

In this paper, we have introduced a novel approach to catheter-based FL ultrasound imaging using a single element transducer integrated into a clinically available steerable catheter together with an OSS system. We also have demonstrated that adaptive NC is successful in interpolating the sparse and irregularly sampled data obtained by manually scanning the catheter. A single element catheter is much simpler to build and use than a multi-element one, evidenced by [29,42,87,90,91]. The only additional component needed to combine the different A-lines is the OSS fiber, which fits easily in the catheter along the transducer coaxial cable, due to its small outer diameter.

The device used in this study has an outer diameter of 4 mm, which makes it suitable for peripheral vascular interventions, such as CTO recanalization. The localization of the channels relative to the calcified regions in the plaque is important during CTO revascularization, since it can point the physician towards the best entry point, shortening the procedure and reducing the risk of complications, such as vessel perforation. In principle, both the transducer and the OSS fiber can be integrated in smaller catheters, such as those used in coronary artery interventions. However, the realization of steerable coronary catheters remains a major challenge.

We combined lateral steering and rotation, resulting in a very high spatial sampling in the central region, but very sparse sampling elsewhere (Figure 5.4(d)). The catheter used in this study is a clinically available device. Since the proposed method should be readily applicable to real patient data, using a state of the art catheter ensures easier translation of this novel concept into the clinics. More agile steerable devices may produce sampling patterns with different characteristics. We applied our experimental scan pattern to the simulated image, retaining only 5% of the original image, which further proves the steering limitation of our device.

Despite the limited information available, NC with isotropic kernel reconstructs the major features of the image as shown in Figure 5.5(f). However, using an isotropic kernel does not take into account the large difference in sampling density along the path compared to the transverse direction, which results in muted image contrast. Using an adaptive anisotropic Gaussian kernel the major features of the simulated target and the TM phantom are reconstructed, preserving the edges and reducing the blurring along the scanning path, as shown in Figure 5.7(c). This is also confirmed by the CR map in Figure 5.7(f), showing that the chosen combination of parameters and lays in the region where the highest CR values are obtained. For the phantom and the carotid plaque specimen, we can reconstruct most of the features which are not recognizable in the sparse maps. A NC algorithm with adaptive kernel was also used in [111] where the anisotropic kernel was rotated according to the gradient angle of a randomly sampled image. However, in our case, due to the particular scanning pattern and the highly sparse nature of the data, the computation of the gradient is not a suitable choice.

In this work, we have focused on the reconstruction of the imaging target surface by combining the intensity signals and the tip-to-target distance information from ultrasound. For the phantom this results in flat surface reconstruction, whereas in the ex-vivo carotid plaque measurements the surface plot shows the differences in distances for the different structures. The same method can be extended to 3D to reconstruct volumetric images of the structures ahead of the catheter.

The FL ultrasound imaging approach presented in this paper has some limitations. If certain regions of the imaging target are not scanned at all, the reconstructed image will fail in providing information about those regions (see for instance the hole at 8 o'clock in the phantom image). This means that the ability to reconstruct FL images with the proposed device requires the scanning pattern to achieve a certain minimum coverage. Steerable catheters with more flexibility than the one used in this work, as well as random probe motion of which there usually is plenty in (cardiac) interventions, may help in optimizing the coverage of the region of interest. To reduce the reconstructed length of the fiber, hence decreasing the error in position estimation, we set the reference point to correspond to the clamping point on the side of the water tank. In a clinical setting this will result in moving the reference point within the human body. Since the OSS system provides strain and curvature information over time for each sensing point along the fiber, this information could be used to identify the stable clamping point within the body and set it as reference point.

5.5 CONCLUSION

In this work, we have successfully integrated a FL single-element ultrasound transducer in a steerable catheter together with an OSS fiber and we have demonstrated the feasibility of achieving FL imaging. The integrated device acquires ultrasound A-lines and OSS data simultaneously at 60 Hz, while manually steering the catheter tip. The manual scanning leads to a sparse and irregularly sampled data set, which requires interpolation to reconstruct the features at the front surface of the imaging target. We have shown that applying Normalized Convolution with an adaptive anisotropic Gaussian kernel on both the intensity and the distance data enables to generate surface plots of the imaging target. By applying adaptive NC on the phantom data, channels and strong reflectors can be identified, whereas in the carotid plaque image the strong calcified areas are successfully reconstructed.

We have shown that, with only 5 % of the original data, it is possible to reconstruct the salient features of the image, such as the location of the channels and the strong reflectors. The chosen combination of adaptive Gaussian parameters, σ_n=250 µm and σ_t=100 µm, leads to image reconstruction of the phantom surface with a contrast ratio of 0.9.

Acknowledgment

We would like to thank R. H. S. H. Beurskens and M. Manten for the help during the device assembly and integration and K. van Gaalen, F. Gijsen, A. Akyildiz and V. Daeichin for the help with the carotid plaque measurements.

Chapter 6

3D Forward-Looking Ultrasound Imaging from a Steerable Single-Element Intracardiac Catheter

Based on:

Jovana Janjic, Frits Mastik, Awaz Ali, Merel D. Leistikow, Johan G. Bosch, Antonius F. W. van der Steen, Gijs van Soest, 3D Forward-Looking Ultrasound Imaging from a Steerable Single-Element Intracardiac Catheter, *in preparation*.

ABSTRACT

In interventional cardiology catheters are routinely used to access and treat defects and diseases in the heart. Image guidance using forward-looking (FL) ultrasound transducers at the tip of the catheter could give the physician visual feedback during complex procedures such as valve replacement or transseptal puncture. In this work, we investigate FL 3D imaging by integrating a 7 MHz single-element ultrasound transducer at the tip of a novel multi-steerable intracardiac catheter together with an optical shape sensing fiber (OSS). We tested the imaging capability of the integrated device on an ex-vivo pig heart. By acquiring ultrasound A-lines at different locations while steering the catheter tip, a sparse 3D image is obtained. To reconstruct a volumetric image from the sparse data we implemented an adaptive Normalized Convolution (NC) algorithm were the dimension, orientation and angle of the 3D anisotropic kernel changes dynamically according to the scanning path. We acquired ultrasound A-lines of the tricuspid valve and we computed the 3D image using NC with both an isotropic kernel and an anisotropic kernel. We successfully interpolated the sparse data obtaining 3D volumes of the heart. By using an anisotropic kernel better 3D reconstruction is achieved with higher detail information compared to the reconstruction obtained using an isotropic kernel. This pilot experiment demonstrates the potential of FL image guidance during intracardiac procedures using a single-element transducer integrated in a steerable catheter with an OSS fiber.

6.1 INTRODUCTION

Minimally invasive intracardiac procedures allow treatment of cardiac rhythm disorders and structural heart diseases avoiding the need of open heart surgery [12]. Thin, flexible catheters are used to access the heart through a blood vessel by making a very small incision. Using these catheters, treatment devices such as stents, balloons, prosthetic valves and needles are advanced into the heart. Visual feedback of the working field within the heart is of great importance since it provides image guidance during complex procedures such as valve replacement or transseptal puncture.

Intracardiac echocardiography (ICE) is an ultrasound-based imaging modality that enables visualization from the inside of the heart. Clinically used ICE catheters consist of a 1D phased array transducer mounted longitudinally on the side of the catheter providing 2D side-looking images. Novel 2D transducer designs have been investigated [20-22], but they still provide side-looking views of the heart. A steerable 3D forward-looking (FL) catheter could provide new views of the heart, enabling easier image interpretation, hence improving treatment outcome [17]. However, FL catheters are not clinically available due to the technical challenge of integrating multi-element transducers at the tip of small catheters.

Several efforts have been taken towards the development of FL intracardiac catheters. Linear arrays providing 2D FL imaging have been proposed using both piezoelectric and capacitive micromachined ultrasound transducer (CMUT) technology [29]. Ring transducers providing FL volumetric imaging have also been investigated [34,42]. However, the major challenge remains integration and interconnection of each transducer element to the external imaging system.

Based on our previous work [77,104], we propose to achieve 3D FL intracardiac imaging using a single-element transducer integrated at the tip of a novel steerable catheter together with an optical shape sensing (OSS) system. By mapping ultrasound A-lines to specific positions in 3D space, while manually steering the catheter, we obtain sparse 3D images. To interpolate the sparse images, we consider Normalized Convolution [108-110] and we implement a 3D adaptive version of the algorithm. We tested the integrated device and the image reconstruction algorithm on data acquired from an ex-vivo pig heart.

6.2 METHODS

The multi-steerable intracardiac catheter has been designed and manufactured at Delft University of Technology (Biomechanical Engineering Dept.). The total length of the catheter is 100 cm with the steerable tip segment 4 cm long and an outer diameter of 3 mm with an inner lumen of 1.5 mm. The handle consists of two joysticks that drive two steerable tip segments

allowing to steer with 4 degrees of freedom (DOF). This novel catheter design enables complex shapes which are not possible with commercially available mechanically actuated devices.

The imaging set-up is shown in Figure 6.1(a). The ultrasound transducer (Blatek Industries, Inc, USA) is a 7 MHz circular element (1 mm in diameter) mounted at the tip of the catheter. The OSS fiber (Philips Research, In-Body Systems, High Tech Campus Eindhoven) is 200 μm in diameter and is guided through the inner lumen of the catheter, providing 3D shape reconstruction of the device using optical frequency-domain reflectometry [48,49]. Further details about the fiber used in this study can be found in [77,104].

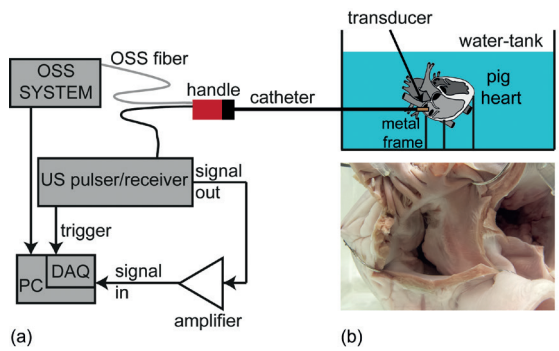

Figure 6.1 (a) Imaging set-up, (b) picture of the imaged area showing the tricuspid valve of the *ex-vivo* pig heart.

The integrated device is inserted from the side of a water tank in which an *ex-vivo* pig heart has been submerged. The pig heart was procured from a local butcher. We dissected the heart exposing the tricuspid valve (Figure 6.2(b)) and a metal frame is used to clamp the tissue using needles and hooks. While manually steering the catheter by manipulating the handle, we acquired simultaneously OSS and ultrasound data. We implemented a Matlab code to acquire OSS and ultrasound data providing a feedback of the area covered. Using this code we achieved an effective frame rate of 50 Hz. The transducer is excited with a 40 ns pulse with an amplitude of 60 V (Avtech Electrosystems Ltd, USA) and the received echoes are amplified with a 40 dB Amplifier (Hewlett-Packard, USA) and digitized using a 350 MHz, 12-bit resolution data acquisition card (Agilent Technologies, USA). Further processing is performed in Matlab 2016b (The MathWorks, USA).

The OSS system provides the 3D shape and curvature of the fiber at each time point. The clamping point on the side of the water tank corresponds to a peak in the curvature plot, hence, by localizing the peak we set the clamping point as a new reference point reducing the reconstruction length to the portion of the catheter that is submerged in water. We then compute the catheter tip position and direction relative to the new reference point and we

further smooth the data using a Savitzky–Golay filter with order 2. The ultrasound data are filtered in Matlab using a Butterworth filter of order 5 with a bandwidth between 5 MHz and 10 MHz. Next, the envelope is computed for each A-line and stored in a 3D volume based on the catheter tip position and direction obtained from the OSS data and the tip-to-target distance from ultrasound.

Due to the manual scanning of the catheter, a sparse and irregularly sampled volume is obtained. To interpolate the sparse data in the 3D volume we consider the adaptive Normalized Convolution (NC) algorithm that we developed in our previous work [77] and we extend it to 3D. We first compute the NC result using a 3D isotropic Gaussian kernel. To define the dimensions of the isotropic kernel we consider, for each sampling point on the scanning path, the distance to the consecutive point along the path and the mean of the 5 closest points off the path. We then take all the distances along the path and compute the third quartile. For the average distances off the path we compute the second quartile. We compute the maximum between the obtained values and set the size of the 3D isotropic kernel to half of it. We smooth the sparse intensity volume and the corresponding certainty volume with the obtained kernel and compute the NC result.

We then implement the 3D adaptive NC algorithm and compare the result to the interpolation obtained considering the isotropic kernel. In the adaptive NC case, the 3D kernel is anisotropic and its dimensions change dynamically according to the scanning path. For each sampling point the 3 dimensions of the kernel are defined considering the distance to the next sampling point on the path, the average distance of the 5 closest points off the path and the distance between two consecutive ultrasound intensity points along the A-line (ultrasound depth direction). Moreover, the orientation of the 3D kernel is defined based on the local direction of the scanning path and the catheter orientation. Therefore, the dimensions and orientation of the 3D anisotropic kernel change dynamically while steering the catheter.

6.3 RESULTS

Figure 6.2(a) shows the scanning pattern of the catheter tip obtained from the OSS data together with the tip direction in 3D, whereas Figure 6.2(b) shows the corresponding ultrasound A-lines. By combining the position information with the ultrasound data we obtain the sparse 3D volume in Figure 6.3(a), where the ultrasound A-lines are placed in the 3D volume based on the catheter tip orientation. Volumetric rendering is done using the free software ParaView. Figure 6.3(b) shows a 3D rendering of the sparse volume using a depth-coloring map obtained with the MeVisLab software (MeVis Medical Solutions, Germany).

Figure 6.4(a) shows the result of volumetric NC using the 3D isotropic kernel. The kernel dimensions is 400 µm in all the directions. Figure 6.4(b) shows the interpolation result

considering adaptive NC with the 3D anisotropic kernel dynamically changing dimensions and orientation based on the local scanning path direction and the tip orientation. Based on Figure 6.4(b), using Otsu's method [112], we extract the surface plot shown in Figure 6.4(c). The surface plot combines the average ultrasound intensity values over a depth of 200 µm starting from the reconstructed tissue surface with the corresponding distance information.

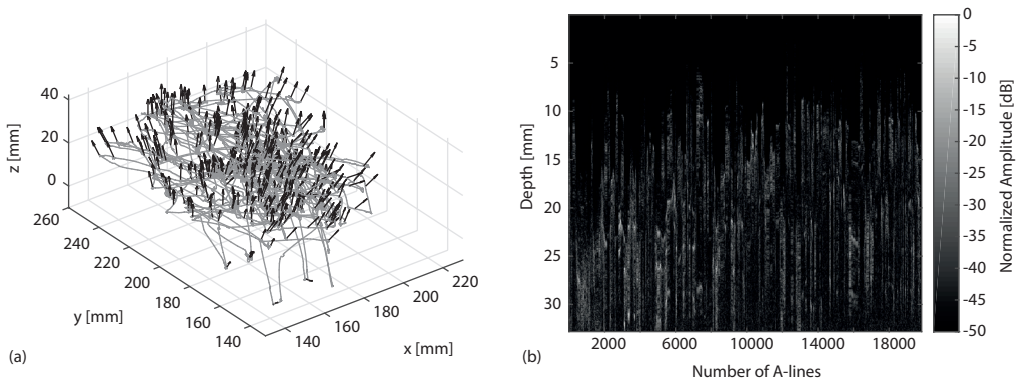

Figure 6.2 (a) Catheter tip scanning pattern (gray) and tip orientation (black arrows) every 50 data points along the path; (b) ultrasound A-lines acquired while scanning the catheter according to the path shown in (b).

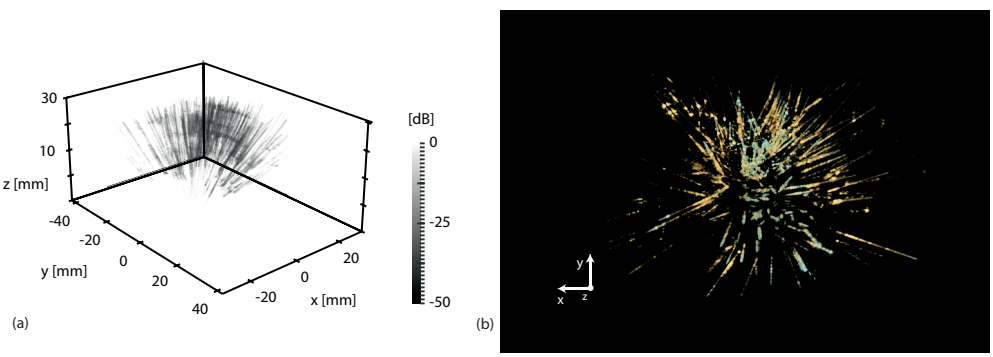

Figure 6.3 Sparse 3D volume obtained by combining the ultrasound A-lines with the catheter tip position information from OSS. (a) sparse intensity volume in gray scale and (b) depth-colored 3D rendering (dynamic range is the same as in (a)).

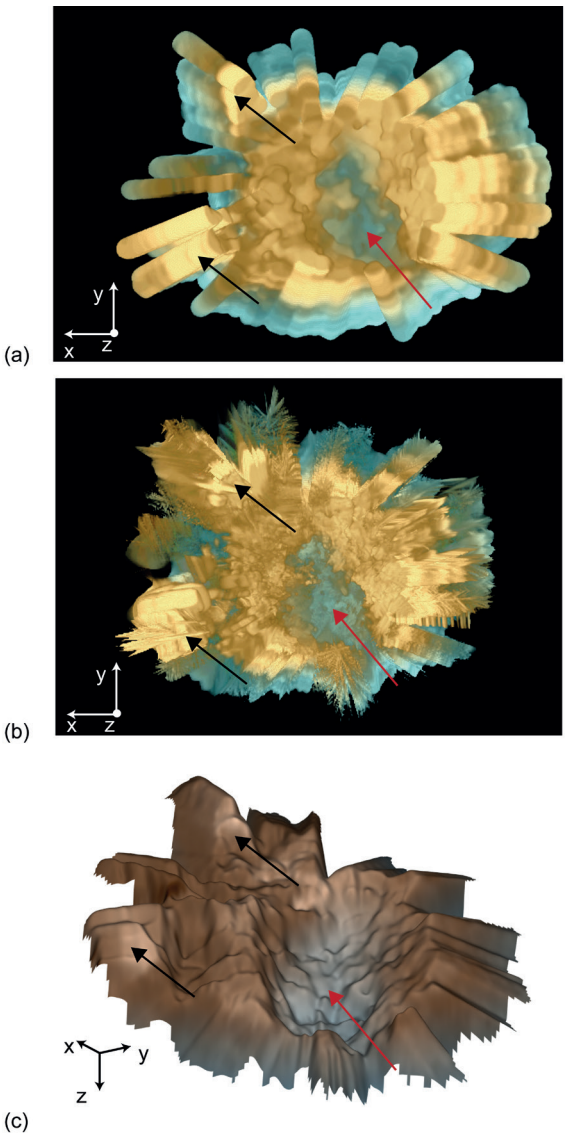

Figure 6.4 (a) 3D depth-colored rendering of the volume obtained using NC with isotropic kernel; (b) 3D depth-colored rendering of the volume obtained with adaptive NC with an anisotropic kernel; (c) surface rendering of volume in (b) with depth-coloring overlayed on grayscale intesity values. Red arrow indicates valve, black arrows indicate needles location. All images have a dynamic range of 50 dB.

6.4 DISCUSSION AND CONCLUSION

We have acquired sparse and irregularly sampled 3D data with a single-element FL steerable catheter manually steered across a dissected *ex-vivo* pig heart. By considering only the sparse data, it is hardly possible to recognize any feature in the 3D volume. NC enables to interpolate the data providing more insights into the structures of the imaging target, such as the location of the valve and the needles used to stabilize the tissue. Using an isotropic 3D kernel results in a volumetric reconstruction that does not take into account the overall spatial coverage and the different sampling densities along the path. This results in a 3D reconstruction with over-smoothing in densely sampled areas such as those corresponding to the valve location. The interpolation of the sparse data with an anisotropic kernel dynamically changing dimensions and orientation results in a volume reconstruction with reduced blurring along the scanning path and improved resolution in the densely sampled regions. It reproduces the 3D morphology of the imaged valve. We also computed the surface plot from the 3D volume obtained with adaptive 3D NC, which clearly shows the depression corresponding to the valve location and the brighter regions corresponding to the locations of the needles and hooks holding the tissue.

Although we fixated the heart on a metal frame, the anatomical features were not fully preserved. This can be noticed in Figure 6.1(b) where the 3 leaflets of the valve are not all fully visible with the bottom one partially collapsed. This issue together with the lack of heart motion limit the representativeness of the current set-up for in-vivo imaging. Future experiments should be performed in beating hearts without performing dissections and navigating the heart chambers and the blood vessels with the steerable and flexible catheter. Moreover, the transducer used in this work is an unfocused single-element with an estimated natural focus of approximately 300 µm at 1.2 mm distance. Beyond this distance the beam width becomes broader affecting the imaging resolution. Alternative ultrasound transducer designs and signal processing methods should be explored to improve imaging quality.

In conclusion, although further optimization and research is required, this work demonstrates that it is possible to acquire volumetric ultrasound images inside the heart from a very simple and potentially cheap interventional platform: a steerable intracardiac catheter on which a single-element ultrasound transducer is mounted. It extends our previous results demonstrating the feasibility of achieving 3D FL image guidance using a single-element transducer, combined with an OSS system for position tracking and sparse spatial sampling along random trajectories. 3D FL imaging during minimally invasive intracardiac interventions provides information over the working field increasing the success rate of complex procedures such as valve replacement or transseptal puncture.

Acknowledgment

This research is supported by the NWO Domain Applied and Engineering Sciences (AES) (grant number 12710 and 12704), which is part of the Netherlands Organisation for Scientific Research (NWO), and which is partly founded by the Ministry of Economic Affairs. We would like to thank Robert H. S. H. Beurskens and Geert Springeling, for the ultrasound transducer and OSS fiber integration into the catheter and Raja S. Bandaru for the support with the imaging software. In addition, we would like to thank Remi van Starkenburg from TU Delft for manufacturing the steerable catheter.

Chapter 7

Speckle in Ultrasound

Based on:

Jovana Janjic and Gijs van Soest, Speckle Physics, in *Handbook of Speckle Filtering and Tracking in Cardiovascular Ultrasound Imaging and Video*, Loizou, Christos P.; Pattichis, Constantinos S; D'hooge, Jan, The Institution of Engineering and Technology, London (UK), 2018, pp. 25-54.

ABSTRACT

Speckle is inherent to imaging with coherent waves. In this chapter, we introduce the basic concepts of speckle as it appears in randomly scattered wave fields. Using concepts from laser speckle originating in optics, we show how the Rayleigh distributed magnitude appears as a very general and robust result from a random phasor sum, with minimal assumptions on the statistics of amplitude and phase of the contributing phasors. Subsequently, the statistics of a scattered field with a constant background and non-uniform phase distributions are demonstrated.

By writing ultrasound scattering in a linear systems formalism, the relations that govern speckle appear straightforwardly in the field scattered by a random structure. We computed the second-order statistics to relate speckle spot size to ultrasound imaging parameters and found that the speckle size is similar, but not identical to the resolution cell dimensions. We outline the case of a small number of contributing waves, leading to the K-distribution, which is one of several heuristic models that have been implemented to descirbe various speckle scenarios. Finally, we discusse the impact of dynamic range compression on speckle statistics, which is important to describe the signal distribution in practical imaging applications.

7.1 INTRODUCTION

Ultrasonic B-mode imaging is fundamentally grayscale imaging: it forms an image based only on the amplitude of the detected echo. It processes the available information in the recorded echoes, which arise from scattering of the transmitted wave by acoustic discontinuities or heterogeneities in the imaged object. The translation from object features to image features is subject to the physics of the wave propagation, scattering, and detection processes that carry the information from object to the imaging system. The imaging physics introduces familiar imaging concepts like image resolution, related to system bandwidth, imaging contrast and penetration depth, related to the acoustic properties of the medium, object, and system parameters like sensitivity and noise. Image interpretation is principally an inversion of these steps: what can we infer about the object from the received echo, combined with some prior knowledge of the imaged object and the imaging system.

Speckle is one of the image features arising in the translation of object structure to an ultrasound image. It manifests itself as "spotty" variations in image intensity, giving rise to a granular appearance instead of homogeneous, flat shades of gray, as is visible in Figure 7.1. As such, speckle can severely compromise interpretation of ultrasound images, particularly in discrimination of small structures. As we will see in this chapter, it is fundamentally impossible to separate the "true" image information from speckle corrupting it. For this reason, the common term "speckle noise" is a misnomer, as there is no way to discriminate the speckle as a "noise" source from the "signal", that we are actually interested in. We will therefore not adopt the notion of "speckle as short-range correlated multiplicative noise" which is frequently applied, but does not adequately represent the complex nature of the resulting scattered field, nor does it encapsulate the statistical properties of amplitude and phase of physical speckle. The concept of speckle as noise also forgoes its use in detection of time varying phenomena: blood vessels, for instance, can be identified by their large speckle variance or short speckle decorrelation time. Nevertheless, quoting the optical physicist Joseph Goodman, to whom many of the concepts we present in this chapter are due: "Although a number of beneficial uses can be made of speckle, it usually is more of a hindrance than a help" [113].

In this chapter, we will discuss the basic physical origins of speckle and present different, but related, mathematical descriptions of speckle in simple model systems. We will start from a general description of scattered waves as phasors, deriving first order statistics applicable to both laser speckle and ultrasound speckle. Subsequently we discuss the correspondences and differences between laser speckle and ultrasound speckle, before presenting higher-order statistics and imaging implications in an ultrasound context. We also introduce the impact of the imaging system characteristics on speckle appearance and statistics.

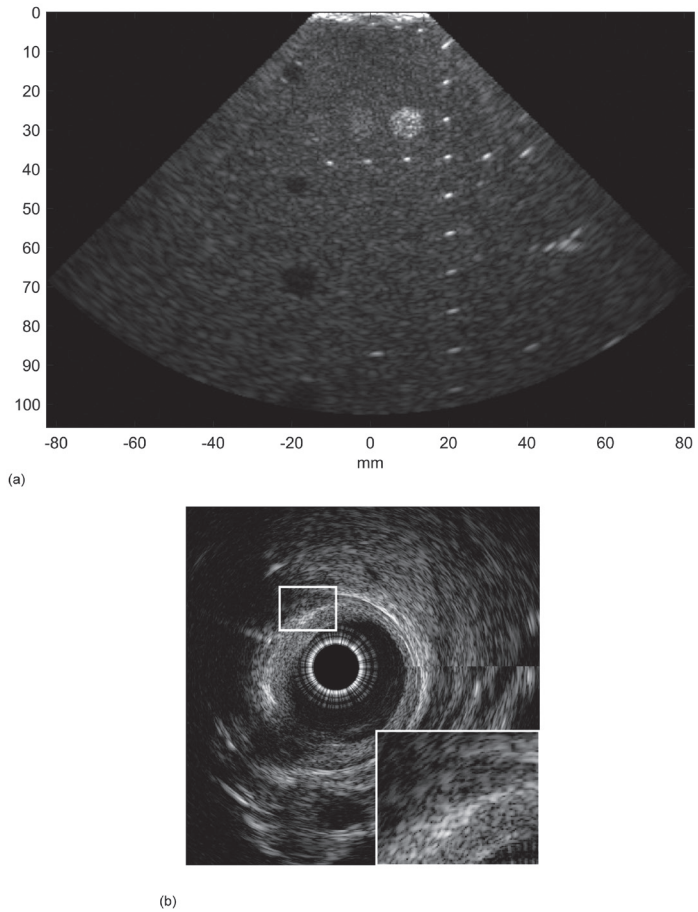

Figure 7.1 Ultrasound speckle. (a) Image of a CIRS ultrasound phantom, obtained with a phased array transducer with an element pitch of 295 μm and a frequency bandwidth of 1–4 MHz. It shows speckle instead of homogeneous gray areas. (b) IVUS image of a human coronary artery specimen ex vivo, rotating single element with a bandwidth of 20–38 MHz.

7.2 SPECKLE OBSERVATIONS

7.2.1 Speckle in optics

Speckle arises from interference of many component waves with random phase, summed to a resultant vector with a stochastic distribution of amplitude and phase. This phenomenon was first described in the scintillation of stars in the late 19th century [114] caused by atmospheric disturbance of the planar wavefront arriving from point sources. The term "speckle" was first coined after the invention of the laser, where it is readily observable as the grainy appearance of laser light scattered off a rough surface [115], as shown in Figure 7.2.

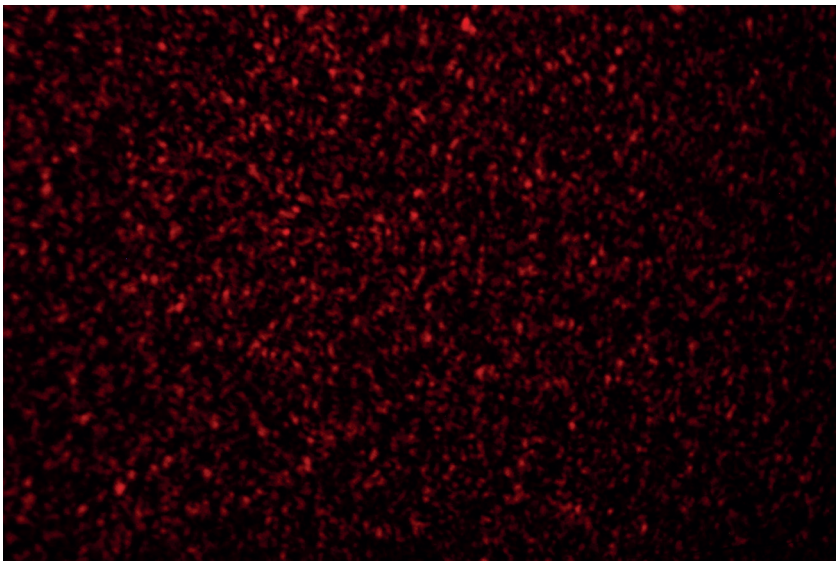

Figure 7.2 Speckle generated by a Helium-Neon laser transmitted through a diffuser.

These observations illustrate that optical speckle arises in two situations: the first is when coherent light illuminates an irregular surface, with a roughness on scale of the optical wavelength; the second situation is when coherent light travels through a medium with variable refractive index [115]. In both cases, the coherence of the illuminating source is a condition for the observation of speckle. A wave's degree of coherence expresses the degree of correlation in amplitude fluctuations in space (spatial coherence) or time (temporal coherence) [116]: within the coherence time or coherence length, the phase relations between different points in the wave field are fixed. The coherence of a wave determines the ability to generate interference effects. Partial coherence refers to a situation where the observation time or area is larger than the coherence domain. By sampling multiple coherence windows in space or time, some of the interference is washed out.

When coherent light illuminates a rough surface, the returning optical wave is the result of the interference of coherent wavelets with random phase that are scattered from the microscopic structures of the surface. If the interference is constructive, a bright spot will characterize the image, whereas, if the interference is destructive, the spot will appear dark [117]. The combination of constructive and destructive interferences leads to the speckle granularity in the image. Speckle appears from a set of many coherent wavelets with random phase. Random scattering of a coherent wavefront creates this system quite readily, as we will see. Complete randomization by heterogeneity in the propagation medium requires a long interaction length, such as occurs when starlight traverses a turbulent atmosphere. In practice, random scattering of coherent waves explains most observations of speckle in ultrasound, and we will focus our

discussion on that situation. It is important to realize that, although the scattering randomizes the phase, this is a deterministic process: as long as the incident wave and the realization of the random scattering structure do not change, the observed speckle remains constant.

7.2.2 Mapping optical speckle concepts to ultrasonic imaging

Optical speckle is usually observed as intensity variations due to far-field interference in a wavefront with random spatial phase disturbances. Ultrasound transducers are sensitive to the amplitude of the incident wave, and derive their contrast from temporal variations in the signal. Speckle manifests as amplitude variations due to temporal phase disturbances. These differences have to be accounted for in the application of speckle concepts from optics to ultrasonic imaging. Figure 7.3 illustrates that, both in the laser and in the acoustic case, speckle is caused by the superposition of wavelets having a random phase.

In classical laser speckle imaging, one can think of the wavelets as being positioned on a plane perpendicular to the direction of wave propagation. Invoking Huygens' principle, the resultant field on an observation screen is the sum of the propagated fields originating from wavelets within a coherence area of the incident field. For separations greater than the (transverse) coherence length of the field, the phase relations between the wavelets are not deterministic, and the interference pattern is washed out. In a ranging technique like ultrasonic imaging, the contributing wavelets are positioned at different, random, distance on the axis of propagation. The resultant amplitude now is the superposition of the waves along the time dimension, and interference results from waves separated in time by less than the coherence time of the field. In ultrasound, the coherence time is equal to the pulse duration: if the pulse spatial length is greater than the distance between two scatterers, the phase is correlated and the pulse can be considered as coherent [117]. These two realizations of speckle are mathematically equivalent, and many results obtained in the rich literature on optical speckle can be applied to ultrasound imaging.

Optical detectors are sensitive to the energy of the incident field, which is proportional to the amplitude squared, unlike ultrasound transducers, which record the incident amplitude itself [64]. This means that in optical speckle the phase is generally not available for analysis. It has to be inferred from auxiliary measurements, which are outside of the scope of this chapter; see [118] for an extensive review. The probability density functions and other statistics for the speckle field are identical for light and sound, but need to be converted into intensity statistics to describe measurements of optical speckle.

Optical coherence tomography (OCT) [119] is often introduced as the "optical analogue of ultrasonic imaging", and as such deserves special mention. In optical coherence tomography, a depth-resolved image of scattering tissue is formed by interferometry. A light source with a short coherence time is used to achieve high axial resolution, much like short pulse in ultrasound imaging. Indeed, the speckle that manifests in OCT, shown in Figure 7.4, is very

similar to that observed in ultrasound, and we have used concepts and results from the OCT literature in this chapter [120-122]. The main difference between OCT and ultrasound speckle is not in the physics, but in the beam "optics" (aperture, lenses) used to transmit and receive the sampling wave.

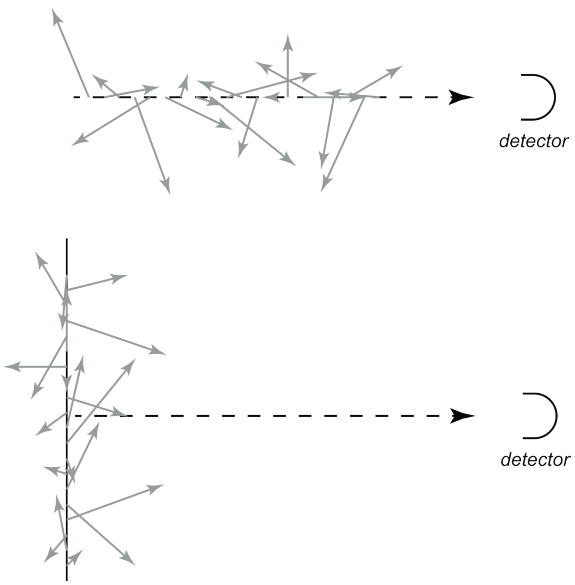

Figure 7.3 The detected field is the result of interference of Huygens wavelets with random amplitude and phase within one resolution. Top: the contributing wavelets are on the line of sight at slightly different delays, as in the case of ultrasound and OCT. Bottom: the contributing wavelets are distributed on a screen perpendicular to the wave propagation direction, as in the case of laser speckle.

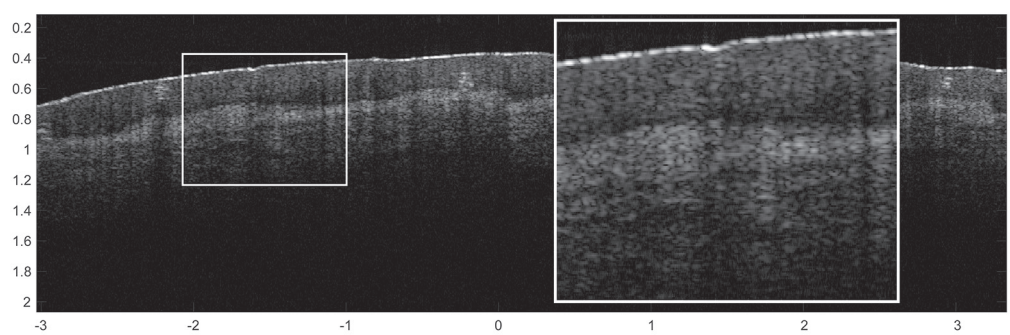

Figure 7.4 OCT image of a finger tip, showing speckle both the darker epidermis and bright dermis layer. Axes in mm.

7.3 SPECKLE AS A 2D RANDOM WALK

The classical explanation for speckle is to conceive the sum of wavelets with random phase as a two-dimensional random walk [115]. For this discussion, we will adopt the conventional term of "phasor", which is a vector $\alpha_n e^{i(\omega_0 t+\varphi_n)}$ that rotates at an angular frequency ω_0, where $\omega_0=2\pi f_0$ and f_0 is the frequency of the incident wave. Its initial phase φ_n is a random variable and t is the propagation delay from its origin to the detector. The amplitude a_n is a positive random variable that reflects the scattering strength. In the simplest case, we assume that φ_n is uniformly distributed on $[-\pi,\pi>$ and that there are sufficient contributing phasors to adequately sample the phase distribution [64]. The variation in t is only due to non-random, slowly varying geometric factors (we are not considering phase randomness due to variations in the medium, which affect t). Both α_n and φ_n are uncorrelated.

If there are N scatterers within a coherence volume of the incident wave, each projecting a wavelet, the resulting complex field S at the detector can be written as the sum of N phasors:

$$S = Ae^{i\Phi} = \frac{1}{\sqrt{N}}\sum_{n=1}^{N} a_n e^{i\varphi_n} \qquad 7.1$$

The random amplitudes $\alpha_n=a_n/\sqrt{N}$ have been normalized for energy conservation, and the propagation delay $e^{i\omega_0 t}$ has been suppressed. Figure 7.5 illustrates analogy between the vector sum of a few phasors and a 2D random walk in the complex plane. This representation of the field, combined with the simple assumptions on φ_n and α_n, allows us to derive some of its statistical properties. Note that in the following derivation, we do not need any information on the distribution of a_n, which makes the resulting speckle statistics robust in homogeneous random media and independent of the details of the scattering structure.

7.3.1 First order statistics

In order to compute statistics for amplitude and phase of the resultant vector, it is convenient to first decompose it into real and imaginary parts. These are given by:

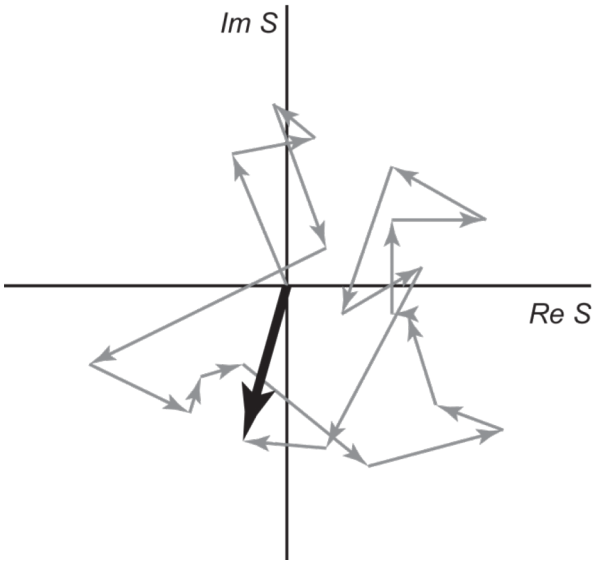

Figure 7.5 Phasor sum as a random walk. The resultant field **S** (black arrow) is the sum of many phasors (smaller gray arrows), each with random amplitude and uniformly distributed random phase .

$$S_r = Re(S) = \frac{1}{\sqrt{N}} \sum_{n=1}^{N} a_n \cos \varphi_n \tag{7.2}$$

$$S_i = Im(S) = \frac{1}{\sqrt{N}} \sum_{n=1}^{N} a_n \sin \varphi_n \tag{7.3}$$

Since both the real and imaginary parts are the sum of independent random components, the central limit theorem enables us to conclude that they are, for large *N*, Gaussian random variables. The $\overline{S_r}$ mean and $\overline{S_i}$ are:

$$\overline{S_r} = \frac{1}{\sqrt{N}} \sum_{n=1}^{N} \overline{a_n \cos \varphi_n} \tag{7.4}$$

$$\overline{S_\iota} = \frac{1}{\sqrt{N}} \sum_{n=1}^{N} \overline{a_n \sin \varphi_n} \tag{7.5}$$

and, since the phases are uniformly distributed over [-π,π>, $\overline{S_r} = \overline{S_i}$=0. The variances σ_R^2 and σ_I^2 can be then calculated as the second moments S_R^2 and S_I^2, which are given by:

$$\overline{S_r^2} = \frac{1}{N} \sum_{n=1}^{N} \sum_{k=1}^{N} \overline{a_n a_k}\ \overline{\cos\varphi_n \cos\varphi_k} \tag{7.6}$$

$$\overline{S_\iota^2} = \frac{1}{N} \sum_{n=1}^{N} \sum_{k=1}^{N} \overline{a_n a_k}\ \overline{\sin\varphi_n \sin\varphi_k} \tag{7.7}$$

and again due to the uniform distribution of the phases over [-π,π>, we have:

$$\overline{\cos\varphi_n \cos\varphi_k} = \overline{\sin\varphi_n \sin\varphi_k} = \begin{cases} 0 & k \neq n \\ \frac{1}{2} & k = n \end{cases} \quad 7.8$$

Therefore,

$$\sigma_R^2 = \sigma_I^2 = \overline{S_r^2} = \overline{S_i^2} = \frac{1}{2N}\sum_{n=1}^{N} a_n^2 = \frac{\bar{A}^2}{2} \quad 7.9$$

The correlation between S_r and S_i is defined as:

$$R_{S_r S_i} = \overline{S_r S_i} = \frac{1}{N}\sum_{k=1}^{N}\sum_{n=1}^{N} \overline{a_k a_n}\ \overline{\cos\varphi_k}\ \overline{\sin\varphi_n} \quad 7.10$$

Terms with $k \neq n$ vanish because of the uncorrelated amplitudes and phases in the sum, while, since sin 2φ=2 sinφ cosφ, we get:

$$\overline{\cos\varphi_k}\ \overline{\sin\varphi_n} = 0 \quad 7.11$$

Therefore, S_r and S_i are uncorrelated.

To summarize, the real and imaginary parts of the resultant vector sum *S* are uncorrelated Gaussian random variables. They have identical variance and zero mean, as expected from the circular geometry of the problem.

To find the probability density function of the magnitude $A=|S|=\sqrt{(S_r^2+S_i^2)}$ and phase Φ of the sum of the phasors, we need to define the joint probability density function of the real and imaginary parts $p_{S_r S_i}$. Again using the central limit theorem, and applying the first and second moments of S_r and S_i computed above, we can write for the joint probability density function

$$p_{S_r S_i}(S_r, S_i) = \frac{1}{2\pi\sigma^2}\exp\left(-\frac{S_r^2 + S_i^2}{2\sigma^2}\right) \quad 7.12$$

with $\sigma^2=\sigma_r^2=\sigma_i^2$. The circular symmetry in $p_{S_r S_i}$, following from the uniform phase distribution, leads to the term "circular complex Gaussian" variate for the phasor sum *S*. From $p_{S_r S_i}$ we can indeed compute the joint probability function of the magnitude and phase by making the appropriate variable transformations [115]. We then derive the marginal distributions of A and Φ. First we define and as follows:

$$A = \sqrt{S_r^2 + S_i^2} \quad 7.13$$

$$\Phi = \tan^{-1}\left(\frac{S_i}{S_r}\right) \quad 7.14$$

S_r and S_i follow accordingly:

$$S_r = A\cos\Phi \tag{7.15}$$
$$S_i = A\sin\Phi \tag{7.16}$$

then we calculate the Jacobian of the transformation

$$\|J\| = \left\| \begin{matrix} \frac{\delta S_r}{\delta A} & \frac{\delta S_r}{\delta \Phi} \\ \frac{\delta S_i}{\delta A} & \frac{\delta S_i}{\delta \Phi} \end{matrix} \right\| = \left\| \begin{matrix} \cos\Phi & -A\sin\Phi \\ \sin\Phi & A\cos\Phi \end{matrix} \right\| = A \tag{7.17}$$

where || ... || denotes the modulus of the determinant.
The joint density function for A and Φ is:

$$p_{A,\Phi} = p_{S_r,S_i}(S_r = A\cos\Phi\,, S_i = A\sin\Phi)\cdot A \tag{7.18}$$

and if we use 7.12 , we obtain

$$p_{A,\Phi} = \begin{cases} \frac{A}{2\pi\sigma^2}\exp\left(-\frac{A^2}{2\sigma^2}\right) & A \geq 0, -\pi \leq \Phi < \pi \\ 0 & \text{otherwise} \end{cases} \tag{7.19}$$

We compute the marginal density for the magnitude A by integration over Φ to get

$$p_A = \begin{cases} \frac{A}{\sigma^2}\exp\left(-\frac{A^2}{2\sigma^2}\right) & A \geq 0 \\ 0 & \text{otherwise} \end{cases} \tag{7.20}$$

This function is known as the Rayleigh density function, displayed in Figure 7.6. Note that the probability of A=0 vanishes. Similarly, we can compute the marginal density for the phase Φ as follows

$$p_\Phi = \begin{cases} \frac{1}{2\pi}\int_0^\infty \frac{A}{\sigma^2}\exp\left(-\frac{A^2}{2\sigma^2}\right)dA & -\pi \leq \Phi < \pi \\ 0 & \text{otherwise} \end{cases} \tag{7.21}$$

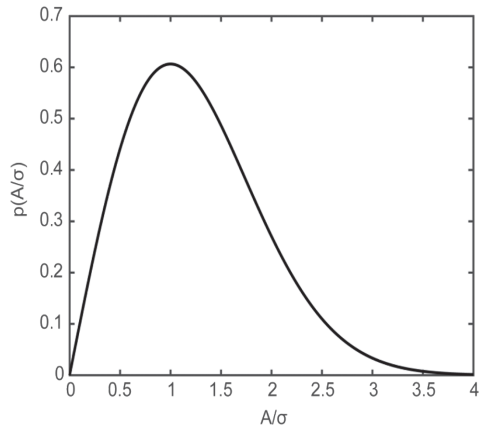

Figure 7.6 The Rayleigh distribution, describing the amplitude statistics of fully-developed speckle.

We can see that the integral argument is the Rayleigh probability density function. Therefore, the integral must be equal to 1. Thus, we obtain

$$p_{\Phi} = \begin{cases} \dfrac{1}{2\pi} & -\pi \le \Phi < \pi \\ 0 & \text{otherwise} \end{cases} \tag{7.22}$$

Clearly, $p_{A,\Phi}=p_A\, p_{\Phi}$, as it should be for independent variables.

With these distributions at our disposal, we can compute the mean and variance of the scattered amplitude:

$$\bar{A} = \sqrt{\frac{\pi}{2}}\sigma \tag{7.23}$$

$$\sigma_A^2 = \Big[2 - \frac{\pi}{2}\Big]\sigma^2 \tag{7.24}$$

If we divide the standard deviation by the mean, we obtain the speckle contrast κ, the inverse of which is often loosely referred to as signal-to-noise ratio SNR [117,123].

$$\kappa = \frac{\sigma_A}{\bar{A}} = \sqrt{\frac{4-\pi}{\pi}} \approx 0.52; SNR = \frac{1}{\kappa} \approx 1.91 \tag{7.25}$$

Figure 7.7 displays the result of an imaging experiment on a tissue-mimicking phantom, scanning a single element transducer along the phantom. The experiment was repeated 15 times, each at a slightly different location, to sample a different realization of the randomness that generates the speckle pattern. Each image has an SNR close to the theoretical value of 1.91.

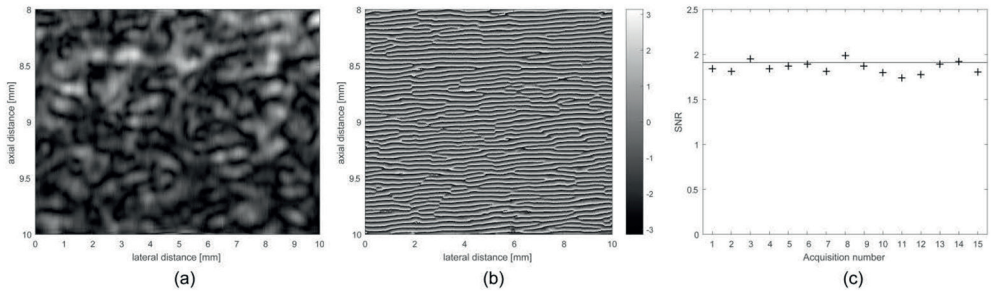

Figure 7.7 Scanning probe measurement: amplitude signal of one acquisition (a), corresponding phase (b) and SNR for all 15 acquisitions (c).

For ultrasound speckle, the statistics of the amplitude is the most relevant quantity. For completeness, allowing the same approach used for the amplitude, we also compute the probability density function of the intensity $I=A^2$. First we relate the intensity and phase to the real and imaginary part by

$$S_r = \sqrt{I}\cos\Phi \tag{7.26}$$

$$S_i = \sqrt{I}\sin\Phi \tag{7.27}$$

The Jacobian of the transformation is:

$$\|J\| = \left\| \begin{matrix} \frac{\delta S_r}{\delta I} & \frac{\delta S_r}{\delta \Phi} \\ \frac{\delta S_i}{\delta I} & \frac{\delta S_i}{\delta \Phi} \end{matrix} \right\| = \frac{1}{2} \tag{7.28}$$

and the joint probability density function can be expressed as:

$$p_{I,\Phi} = p_{S_r,S_i}\left(S_r = \sqrt{I}\cos\Phi\,, S_i = \sqrt{I}\sin\Phi\right)\cdot\frac{1}{2} \tag{7.29}$$

By substituting 7.19 in 7.29 we get:

$$p_{I,\Phi} = \begin{cases} \frac{1}{4\pi\sigma^2}\exp\left(-\frac{I}{2\sigma^2}\right) & I \geq 0, -\pi \leq \Phi < \pi \\ 0 & \text{otherwise} \end{cases} \tag{7.30}$$

We can then integrate over the phase, obtaining

$$p_I(I) = \begin{cases} \frac{1}{2\sigma^2}\exp\left(-\frac{I}{2\sigma^2}\right) & I \geq 0, \\ 0 & \text{otherwise} \end{cases} \tag{7.31}$$

which is defined as the exponential probability density function, which has its maximum value at I=0. The phase is obviously unaffected by the transformation and is still uniformly distributed

on $[-\pi,\pi>$. Note that for the intensity, $\overline{I}=\sigma_I=2\sigma^2$ and $\kappa=1$, a result that seriously complicates imaging with coherent light! The physical interpretation of these results can be summarized as follows: if we have a medium that randomizes the phase of an incident wave to such a degree that the received signal can be represented as the sum of a large number of phasors, the amplitude of the complex scattered field follows a Rayleigh distribution, while the phase is uniformly distributed. The only assumptions we made are: uncorrelated phasor amplitudes and phases, uniformly distributed phases; and large N, which allowed us to apply the central limit theorem that straightforwardly produces the Gaussian circular statistics for the field. Speckle fulfilling these criteria is called "fully-developed", and allows us to describe the underlying physics in a concise manner. A scattered field consisting of few phasors, phasors with non-uniformly distributed phases, or correlated amplitudes, does not obey these simple statistics, as we will show later on in this chapter. Partially developed speckle is commonly encountered in ultrasound imaging. Its analysis is more complex and requires more knowledge about the scattering structure.

7.3.2 Sums of speckle patterns

We mentioned in Section 7.2.1 that speckle is a deterministic random process: the signal scattered by a random structure, probed by a wave of the same frequency content and directionality, will always yield the same speckle pattern. As will become clear in the remainder of this book, many strategies to mitigate the effects of speckle rely on some form of averaging, where one control variable is changed to produce different speckle patterns that can then be summed or compounded.

Consider two random phasor sums, $S_1 = \frac{1}{\sqrt{N}}\sum_{n=1}^{N} a_n e^{i\varphi_n}$ and $S_2 = \frac{1}{\sqrt{M}}\sum_{n=1}^{M} b_n e^{i\vartheta_n}$. If both satisfy the conditions for fully developed speckle, a_n and b_n are uncorrelated random variables, as are the phases φ_n and ϑ_n. The sum of these two fields $S = S_1 + S_2 = \frac{1}{\sqrt{N}}\sum_{n=1}^{N} a_n e^{i\varphi_n} + \frac{1}{\sqrt{M}}\sum_{n=1}^{M} b_n e^{i\vartheta_n}$ can be written as $S = \frac{1}{\sqrt{N+M}}\sum_{n=1}^{N+M} c_n e^{i\gamma_n}$, where $c=a \cup b$ and $\gamma=\varphi \cup \vartheta$. This again has the form of a random phasor sum: it represents a longer random walk. Addition of speckle patterns on a complex amplitude basis does *not* alter the statistics.

If we compute, on the other hand, the incoherent sum of the resultant field, based on the signal envelopes, $A_n=|S_n|$ the distribution does change. The sum of N speckle fields is:

$$A_S = \sum_{n=1}^{N} A_n \qquad 7.32$$

Before going into mathematical detail, the net gain in SNR can be estimated from general results in probability theory. A sum A_s of N real-valued, identically distributed, uncorrelated random variates, each with a mean $\overline{A}$ and standard deviation σ_A, has an expected value $\overline{A}_s=N\overline{A}$ and a standard deviation $\sigma_{A_S}=\sqrt{N}\sigma_A$. The SNR of the summed fields thus scales as $1/\sqrt{N}$; a well-known and commonly applied result.

If α and β are two random variables with probability density functions $p_\alpha(\alpha)$ and $p_\beta(\beta)$, the probability distribution of the sum $\alpha+\beta$ is given by the convolution of their individual distributions, $p_{\alpha+\beta}(\alpha+\beta)=p_\alpha(\alpha)\otimes p_\beta(\beta)$. Hence, for a sum $N=2$ of fully-developed speckles with identical magnitude (same σ), an exact result for the probability distribution of the resulting magnitude can be found from the convolution of a Rayleigh distribution with itself:

$$p_{S,N=2}(A_s) = \frac{A_s}{2\sigma^2} e^{-\frac{A_S^2}{2\sigma^2}} + \frac{\sqrt{\pi}}{4\sigma} e^{-\frac{A_S^2}{4\sigma^2}} \left(\frac{A_S^2}{\sigma^2} - 2\right) \operatorname{erf}\left(\frac{A_s}{2\sigma}\right) \tag{7.33}$$

where $\operatorname{erf}(x) = \frac{2}{\sqrt{\pi}} \int_0^x e^{-t^2}\, dt$ is the error function, and the integration over the phase has been implicitly performed.

The distribution of the sum A_s can be computed for general N, in principle, using the characteristic function. The characteristic function $M_x(\omega)$ of a random variable x is the expectation value of $e^{i\omega x}$, or equivalently, the inverse Fourier transform of its probability density function. It can be found using symbolic manipulation software:

$$\begin{aligned} M_A(\omega) &= \int_0^\infty e^{i\omega A} p_A(A) dA = \frac{1}{2\pi} \int_0^\infty e^{i\omega A} \frac{A}{\sigma^2} e^{-\frac{A^2}{2\sigma^2}} dA \\ &= 1 - \sqrt{2}\sigma\omega D_+\left(\frac{\sigma\omega}{\sqrt{2}}\right) + i\sigma\omega\sqrt{\frac{\pi}{2}} e^{-\frac{\sigma^2\omega^2}{2}}. \end{aligned} \tag{7.34}$$

Here, D_+ is the function known as Dawson's integral, defined as $D_+(x) = e^{-x^2} \int_0^x e^{t^2} dt$. The characteristic function of A_S then is:

$$M_{A,S} = \prod_{n=1}^{N} M_{A,n} = [M_A(\omega)]^N. \tag{7.35}$$

The last equality holds if we assume that all contributing fields have the same mean amplitude (and thus, the same $\sigma_n=\sigma$). We can write the probability distribution of A_s as the Fourier transform of M_S. It turns out, however, that for $N>2$, the analytic form of $p_{S,N}$ cannot be straightforwardly computed, nor is it known in literature. The moments of the distribution can be found by serial differentiation of M_S (from which the probability distribution function itself can be approximated in principle by construction of a moments series). Again, by the central limit theorem, the distribution of magnitudes approaches a Gaussian for $N\to\infty$.

For some applications [124], the statistics of the signal power in a sum of speckles is of interest. The probability distribution function of a sum of intensities:

$$I_S = \sum_{n=1}^{N} I_n = \sum_{n=1}^{N} |A_n|^2 \tag{7.36}$$

can be computed using the characteristic function of the exponentially distributed intensity [118]:

$$M_I(\omega) = \frac{1}{1 - i\omega\bar{I}} \tag{7.37}$$

where $\bar{I}$=$2\sigma^2$ is the average intensity as in defined in Section 7.3.1. As above, $M_{I,S} = \prod_{n=1}^{N} M_{I,n} = [M_I(\omega)]^N$, for an ensemble of speckles with equal mean intensity, which can be Fourier transformed to yield:

$$p_S(I_S) = \frac{I_S^{N-1}}{\Gamma(N)\bar{I}^N} e^{-I_S/\bar{I}} \tag{7.38}$$

where $\Gamma(N)$ is the gamma function and $\bar{I}$ is the mean intensity of each contributing field. For large N, the distribution again tends towards a Gaussian.

7.3.3 Speckle pattern plus a non-random phasor

The preceding sections discussed the case of fully developed speckle, arising when many wavelets with random phase interfere. In practical imaging situations, scattering media are often heterogeneous, containing strongly reflecting boundaries that can be resolved amidst a speckle generate by unresolved, microscopic scattering. The reflections generate a constant background field. The scattered field can now be described as the sum of a random walk and the constant, known phasor. The approach here follows [118]. Aligning the constant phasor A_0 with the real axis, we can add it to the real component of the field in 7.12 to yield

$$p_{S_r S_i}(S_r, S_i) = \frac{1}{2\pi\sigma^2} \exp\left(-\frac{(S_r + A_0)^2 + S_i^2}{2\sigma^2}\right) \tag{7.39}$$

We again perform the transformation of variables 7.15–7.17 and find:

$$p_{A,\Phi}(A, \Phi) = \begin{cases} \dfrac{A}{2\pi\sigma^2} \exp\left(-\dfrac{A^2 + A_0^2 - 2AA_0\cos\Phi}{2\sigma^2}\right) & A > 0\,, -\pi < \Phi \leq \pi \\ 0 & \text{otherwise} \end{cases} \tag{7.40}$$

The probability distribution of the magnitude of the resultant phasor can be obtained by integration of above equation with respect to the phase Φ. Therefore,

$$p_A(A) = \begin{cases} \dfrac{A}{2\pi\sigma^2} e^{-\frac{A_0^2 + A^2}{2\sigma^2}} \displaystyle\int_{-\pi}^{\pi} e^{-\frac{AA_0\cos\Phi}{\sigma^2}} d\Phi = \frac{A}{\sigma^2} e^{-\frac{A_0^2 + A^2}{2\sigma^2}} I_0\left(\frac{A_0 A}{\sigma^2}\right) & A > 0 \\ 0 & \text{otherwise} \end{cases} \tag{7.41}$$

where I_0 is the modified Bessel function of the first kind and order zero. The above expression is known as the Rician density function; Figure 7.8 shows the distribution for a number of different background amplitudes k=A_0/σ. It reduces to the Rayleigh distribution for A_0=0, as expected. The mean and the variance can be calculated from the first two moments of the density function. Thus:

$$\bar{A} = \int_0^\infty \frac{A}{\sigma^2} e^{-\frac{A_0^2+A^2}{2\sigma^2}} I_0\left(\frac{A_0 A}{\sigma^2}\right) dA \qquad 7.42$$

$$= \sqrt{\frac{\pi}{2}}\sigma e^{-\frac{k^2}{4}}\left[\left(1+\frac{k^2}{2}\right) I_0\left(\frac{k^2}{4}\right) + \frac{k^2}{2} I_1\left(\frac{k^2}{4}\right)\right]$$

$$\overline{A^2} = \sigma^2[2+k^2] \qquad 7.43$$

where $I_1$is the modified Bessel function of the first kind and order one.

If k is large, then the density function of the magnitude approximates the Gaussian density function

$$p_A(A) \cong \frac{1}{\sqrt{2\pi}\sigma} e^{-\frac{(A-A_0)^2}{2\sigma^2}} \qquad 7.44$$

with $\overline{A} \cong \overline{A}_0$ and $\overline{A^2} \cong \sigma^2$.

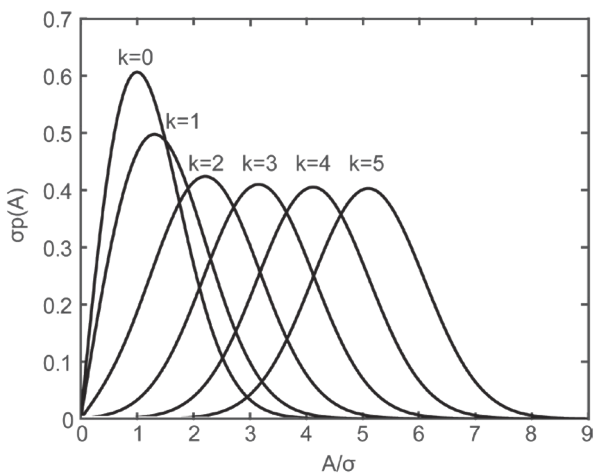

Figure 7.8 The Rician distribution, resulting from a random phasor sum and a constant background. The function is plotted for a number of different ratios $k=A_0/\sigma$ between background phasor amplitude and the standard deviation of the random scattered field. For k=0, the Rayleigh distribution appears, while for k>>1, the curve tends towards a normal distribution.

To find the density function of the phase, we integrate with respect to the magnitude and we obtain

$$p_\Phi(\Phi) = \frac{e^{-\frac{k^2}{2}}}{2\pi} + \frac{k\cos\Phi}{\sqrt{2\pi}} e^{-\frac{k^2 sin^2\Phi}{2}} \left(\frac{1+\mathrm{erf}\left(\frac{kcos\Phi}{\sqrt{2}}\right)}{2}\right) \qquad 7.45$$

for $-\pi<\Phi\leq\pi$.

Note that for k=0 the distribution is uniform, while for $k\to\infty$ the function converges to the delta function at Φ=0. If k is large, the density function of the phase approximates a Gaussian function [118]

$$p_\Phi(\Phi) \cong \frac{k}{\sqrt{2\pi}} e^{-\frac{k^2\Phi^2}{2}} \tag{7.46}$$

with $\overline{\Phi}\cong 0$ and $\Phi^2 \cong \frac{1}{k^2}$the first and second moment, respectively. The variance equals the second moment because $\overline{\Phi}\cong 0$.

7.3.4 Non-uniform phase distribution

Like the constant background phasor presented in the previous sections, deviations from uniform, uncorrelated, isotropic randomness in the scattering structure can give rise to non-uniformly distributed phases of the component phasors; one example in ultrasonic imaging is long-range correlation of scatterer position. If we relax the assumption of uniform phase distribution, there is no general closed from for the amplitude distribution, but maintaining the statistical independence of amplitudes and phases, we can still compute some properties of the scattered field (see [125]; sect 2.9 and Appendix B). We start from equations 7.4 and 7.5:

$$\overline{S_r} = \frac{1}{\sqrt{N}} \sum_{n=1}^{N} \overline{a_n}\ \overline{\cos\varphi_n} \tag{7.47}$$

$$\overline{S_\imath} = \frac{1}{\sqrt{N}} \sum_{n=1}^{N} \overline{a_n}\ \overline{\sin\varphi_n} \tag{7.48}$$

and recognize that the mean trigonometric functions can be expressed in terms of the characteristic function of the phase:

$$\overline{\cos\varphi_n} = \tfrac{1}{2}\left(\overline{e^{\imath\varphi}} + \overline{e^{-\imath\varphi}}\right) = \tfrac{1}{2}\left[M_\varphi(1) + M_\varphi(-1)\right] \tag{7.49}$$

$$\overline{\sin\varphi_n} = \tfrac{1}{2\imath}\left(\overline{e^{\imath\varphi}} + \overline{e^{-\imath\varphi}}\right) = \tfrac{1}{2\imath}\left[M_\varphi(1) - M_\varphi(-1)\right] \tag{7.50}$$

With this result, we can express the mean real and imaginary components of the resultant field as

$$\overline{S_r} = \frac{\sqrt{N}\overline{a}}{2}\left[M_\varphi(1) + M_\varphi(-1)\right] \tag{7.51}$$

$$\overline{S_\imath} = \frac{\sqrt{N}\overline{a}}{2i}\left[M_\varphi(1) - M_\varphi(-1)\right] \tag{7.52}$$

Again using Euler's formulas, the variances and covariance can be written in similar terms:

$$\sigma_r^2 = \overline{S_r^2} - \overline{S_r}^2 = \frac{\overline{a^2}}{4}\left[2 + M_\varphi(2) + M_\varphi(-2)\right] - \frac{\overline{a}^2}{4}\left[2M_\varphi(1)M_\varphi(-1) + M_\varphi^2(1) + M_\varphi^2(-1)\right] \tag{7.53}$$

$$\sigma_i^2 = \overline{S_i^2} - \overline{S}_i^2 = \frac{\overline{a^2}}{4}[2 - M_\varphi(2) - M_\varphi(-2)] - \frac{\overline{a}^2}{4}[2M_\varphi(1)M_\varphi(-1) - M_\varphi^2(1) - M_\varphi^2(-1)] \quad 7.54$$

$$C_{ri} = \overline{S_r S_i} - \overline{S}_r \overline{S}_i = \frac{\overline{a^2}}{4i}[M_\varphi(2) - M_\varphi(-2)] - \frac{\overline{a}^2}{4i}[M_\varphi^2(1) - M_\varphi^2(-1)] \quad 7.55$$

With a few extra assumptions, simpler expressions can be computed. First, in the important special case that $p_\varphi(\varphi)$ is symmetric around φ =0 (and any probability distribution that is symmetric around a central value can be shifted to the origin by a rotation of the coordinate system), the characteristic function is even and real. As a result,

$$\begin{gathered} \overline{S_r} = \sqrt{N}\bar{a}M_\varphi(1) \\ \overline{S_i} = 0 \\ \sigma_r^2 = \tfrac{1}{2}\overline{a^2}\left[1 + M_\varphi(2)\right] - \bar{a}^2 M_\varphi^2(1) \\ \sigma_i^2 = \tfrac{1}{2}\overline{a^2}\left[1 - M_\varphi(2)\right] \\ C_{ri} = 0 \end{gathered} \quad 7.56$$

Inspection of these equations shows that the mean of the real part of the resultant field is now non-zero, and the variances of real and imaginary parts differ. Hence, the scattered field is no longer a circular complex random variable.

More specifically, if the phase is a zero-mean Gaussian variable with a probability density function $p_\varphi(\varphi) = \frac{1}{\sqrt{2\pi}\sigma_\varphi}\exp\left(-\frac{\varphi^2}{2\sigma_\varphi^2}\right)$, , the characteristic function is

$$M_\varphi(\omega) = \exp\left(-\frac{\sigma_\varphi^2\omega^2}{2}\right) \quad 7.57$$

Substitution in the relations above yields

$$\begin{gathered} \overline{S_r} = \sqrt{N}\bar{a}e^{-\frac{\sigma_\varphi^2}{2}} \\ \overline{S_i} = 0 \\ \sigma_r^2 = \tfrac{1}{2}\overline{a^2}\left[1 + e^{-2\sigma_\varphi^2}\right] - \bar{a}^2 e^{-\sigma_\varphi^2} \\ \sigma_i^2 = \tfrac{1}{2}\overline{a^2}\left[1 - e^{-2\sigma_\varphi^2}\right] \\ C_{ri} = 0 \end{gathered} \quad 7.58$$

For $\sigma_\varphi^2 \to \infty$,, the probability density function of the phase approaches a uniform distribution, and we retrieve the familiar means and variances of section 2.3.1.

7.4 SPECKLE IN ULTRASONIC IMAGING

In ultrasound imaging, the signal arises from backscattered waves inside the imaged object. Acoustic heterogeneity gives rise to scattering structures, which in biological tissue span a large range of characteristic length scales; micrometers at the subcellular level to centimeters or decimeters at the organ level. At length scales smaller than the acoustic wavelength, biological tissue can, to a degree, be modeled as a random acoustic medium with a spectrum of correlation lengths, and scattering coefficients that depend on tissue type. Larger structures reflect ultrasound, rather than scatter it, and present as readily recognizable structures (see, for instance, the wire reflections in Figure 7.1(a). As these large structures do not exhibit randomness on the scale of a wavelength, they do not generate speckle.

In the treatment of speckle as an ultrasound scattering phenomenon, we will implicitly depend on the Born approximation, which states that the scattered field is small in comparison to the incident beam. This allows us to neglect multiple scattering and attenuation due to scattering, both reasonably accurate assumptions in most ultrasound imaging applications. Acoustic absorption of course exponentially attenuates the field amplitude, but is not essential for understanding ultrasound speckle, since path length differences contributing to the random interference are small in the single scatter approximation.

7.4.1 Random ultrasound scattering in 1D

The phase randomness that is evident in the Rayleigh-distributed signal distribution arises because of the presence of many scatterers within a resolution cell, the scattered fields of which are added coherently to result in a random local phase. The random phasor sum 7.1 appears straightforwardly if we simplify the ultrasound scattering treatment to a one-dimensional linear systems description. In this framework, the field emitted by a scattering potential Ψ that is insonified with a finite-length pulse can be written as the convolution

$$S = \Psi \otimes h \tag{7.59}$$

Here h is the axial point spread function as determined by the temporal impulse response of the band-limited system, which we write as $h(t)=H(t)e^{i2\pi f_0 t}$, the product of a carrier wave of frequency f_0 and the envelope $H(t)$ that is the Fourier transform of the power spectral density of the pulse. For a single point-like scatterer located at position z_1, $\Psi=\Psi_1\delta(z-z_1)$, and so

$$S_1(t) = \Psi_1 h(t - z_1/c) = \Psi_1 H(t - z_1/c) e^{i2\pi f_0 t} e^{-i2\pi f_0 z_1/c} \tag{7.60}$$

This expression shows that the amplitude response is limited in time by the extent of H, and that it incurs a phase $2\pi f_0 z_1/c$. Figure 7.9(a) shows a graph of the scattered field in response to a two-cycle Gaussian envelope excitation. If we now complicate the scattering structure by adding a few more point-like potentials at random positions, $\Psi = \frac{1}{\sqrt{N}} \sum_{n=1}^{N} \Psi_n \delta(z - z_n)$, then

$$S_N(t) = \frac{1}{\sqrt{N}} \sum_{n=1}^{N} \Psi_n H(t - z_n/c) e^{i2\pi f_0 t} e^{-i2\pi f_0 z_n/c} = \frac{1}{\sqrt{N}} \sum_{n=1}^{N} a_n e^{i\varphi_n} \qquad 7.61$$

The a_n=$\Psi_n H(t-z_n/c)$ form a set of random amplitudes at any given time , and the phase φ_n=$2\pi f_0$ z_n/c. This expression has the exact form of 7.1 if the positions z_n are random. It follows that the scattered field from a random scattering potential is a speckle: it is a random zero-mean circular Gaussian variable. Its amplitude is a random variable that follows a Rayleigh distribution, and the phase is uniformly distributed on $|-\pi,\pi>$, the random phase being a consequence of the random scatterer position. The one caveat is that the density of scatterers *per resolution cell* needs to be large enough for the Rayleigh distribution to emerge, as illustrated by Figure 7.9(c) (d). Sections of S that are separated in time by more than the width of $H(t)$ are uncoupled and have independent statistics. This argument can be expanded to two and three dimensions, as we will do to compute speckle spot size.

Returning to the linear systems formulation of scattering and Fourier transforming it (indicated by hats; $F(\cdot)=\hat{\cdot}$) yields a product in spatial frequency space

$$\hat{S}(k) = \hat{\Psi}(k) \cdot \hat{h}(k) \qquad 7.62$$

The axial width of the point spread function is a consequence of the band limitation of the ultrasound imaging system, which appears here directly as $k_z = \frac{f}{c}$. For frequencies outside the system bandwidth $f_0 \pm \Delta f/2$, the response of the system vanishes. This relation shows that the recorded scattered field S only contains spatial frequencies within the band of $\hat{h}$. By the Wiener-Khinchine theorem, the frequency spectrum of S is the Fourier transform of the autocorrelation function R_S=$<S(z_1)S(z_2)>$=$R_S(\Delta z)$. The scattered field only samples spatial frequencies of the scattering structure in a passband centered $2/\lambda$, with a bandwidth of the order of $2\Delta f/_c$, depending on the shape of the envelope of h [126,127].

Tissues contain a range of randomly arranged scattering structures, ranging in size from vesicles and cells (large spatial frequency) to blood vessels (small spatial frequency). A range of tissue acoustic models exists that predict the frequency dependence of the scattered field, which is to some degree tissue specific. The equivalence of the linear scattering formulation in real space and k-space shows that the randomness of speckle obscuring features of the imaged structure, and the limited sampling of spatial frequency space, are in fact two sides of the same coin.

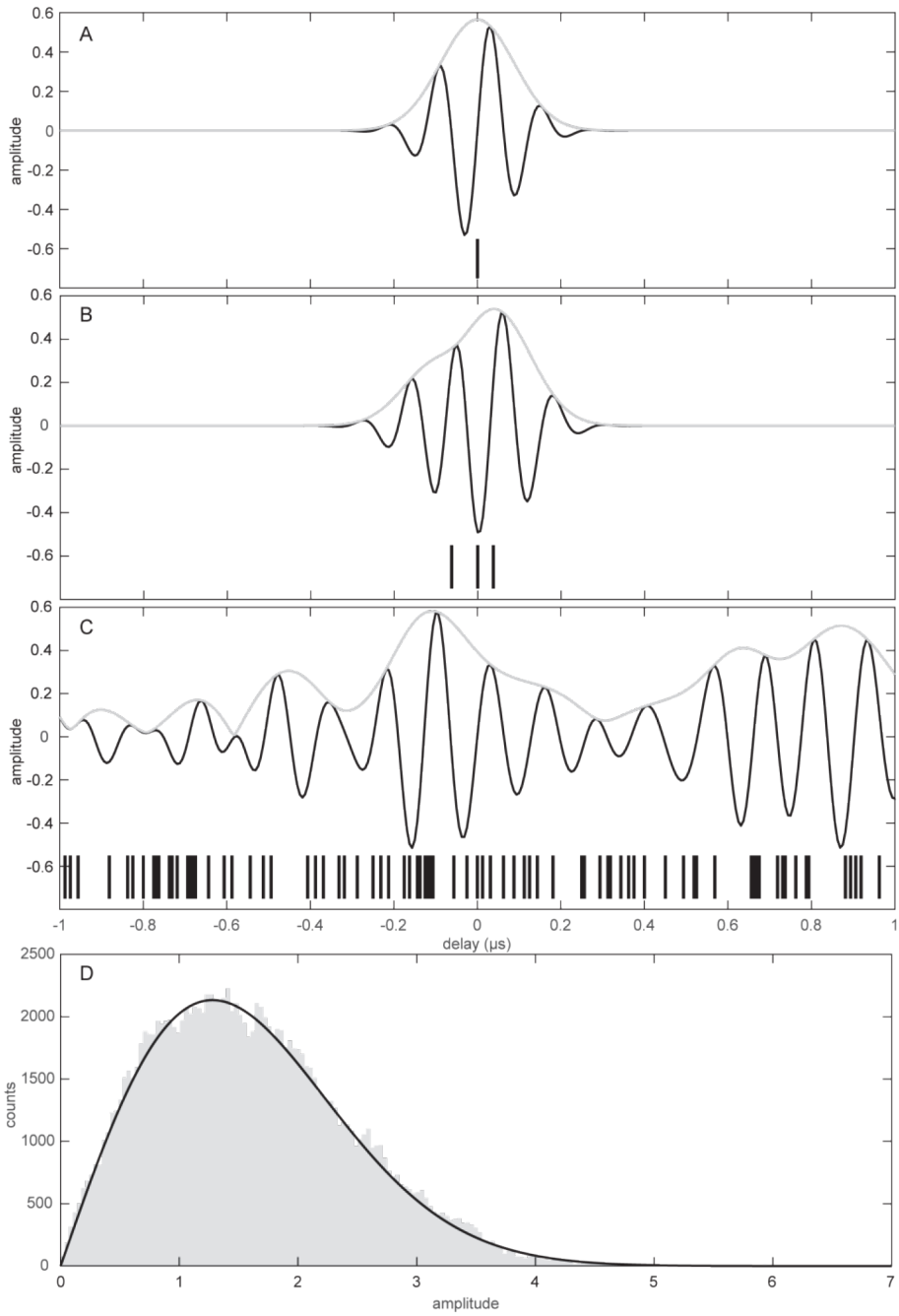

Figure 7.9 Response to a 2-cycle sine wave with a Gaussian envelope, simulated in a linear system as in Eq. (60). (A) Single scatterer (indicated by the vertical line. (B) Three randomly positioned scatterers within one resolution cell affect the amplitude and phase; note the shift of the trough over the centre scatterer. (C) Many scatterers (N=12 per resolution cell) exhibit speckle. (D) Increasing the number of scatterers and the length of the simulated trace yields a Rayleigh distribution of the envelope (simulation parameters are arbitrary).

7.4.2 Second order speckle statistics in ultrasound

The second-order statistics enables to describe the statistical relation between two different pixels in the image. Among many other speckle features, they allow the computation of the speckle spot size, which is an important parameter in determining the degree to which speckle affects the image. To derive the autocorrelation and autocovariance of the complex ultrasound field S, we again adopt the linear systems description of ultrasound scattering [123]. Therefore,

$$S = \int_{-\infty}^{+\infty} \Psi(\mathbf{x} - \mathbf{x}')h(\mathbf{x}')d\mathbf{x}' = \Psi(\mathbf{x}) \otimes h(\mathbf{x}) \tag{7.63}$$

where Ψ is the complex scattering amplitude and h is the point spread function.
The autocorrelation function R_S is:

$$R_s = E[S(\mathbf{x_1})S^*(\mathbf{x_2})] = R_\Psi(\mathbf{x_1}, \mathbf{x_2}) \otimes h(\mathbf{x_1}) \otimes h^*(\mathbf{x_2}) \tag{7.64}$$

Where $R_\Psi(\mathbf{x_1}, \mathbf{x_2}) = E[\Psi(\mathbf{x_1})\Psi^*(\mathbf{x_2})]$ and $E[\cdot]$ denotes the expectation operator. Since the real and imaginary parts of S are uncorrelated Gaussian random variables with zero mean, $C_s = R_s$, where C_s is the autocovariance of the speckle field.

As before, we assume weak interaction between the medium and the ultrasound field, discarding any multiple scattering. Furthermore, the coarse macroscopic scattering strength is slowly varying compared to the correlation of the microstructure. This diagonalizes the scattering amplitude autocovariance R_Ψ [123]:

$$R_\Psi(\mathbf{x_1}, \mathbf{x_2}) = |\Psi(\mathbf{x})|^2 \tag{7.65}$$

with $x_1 = x \cong x_2$ and $\Delta x = x_2 - x_1$.

If the imaging target is a homogenous distribution of scatterers, or, more generally, the macroscopic scattering structure is slowly varying compared to the width of the point spread function, we can write it as a constant locally: $|\Psi(\mathbf{x})|^2 = \Psi_0^2$. This allows us to rewrite

$$C_S(\Delta\mathbf{x}) = \Psi_0^2 h(-\Delta\mathbf{x}) \otimes h^*(\Delta\mathbf{x}) \tag{7.66}$$

From 7.66, we can conclude that, when imaging objects composed of randomly dispersed fine particles, speckle contains information only about the point spread function.

Assuming that we are in the focal region of the ultrasound transducer, the point spread function can be separated along two orthogonal directions: the insonification direction z (longitudinal) and the transverse direction x (lateral) [128]

$$h(x, z) = h_x h_z \tag{7.67}$$

and the covariance matrix can be written as follows:

$$C_S(\Delta x, \Delta z) = C_{Sx}(\Delta x) C_{Sz}(\Delta z) \tag{7.68}$$

Therefore, it is possible to analyze the resulting two covariance functions separately.

For a rectangular transducer the transverse point spread function in the focal plane is defined as:

$$\begin{aligned} h(x) &= B\mathrm{sinc}^2(\pi x \xi_0) \\ \xi_0 &= D/\lambda z_0 \end{aligned} \tag{7.69}$$

with B a normalization factor, D the width of the transducer, λ the wavelength and z_0 the focal zone distance from the transducer. The expression in 7.69 is obtained assuming continuous wave approximation, which can be used as a first order estimate of the spatial response in the focal zone.
The autocovariance matrix in the transverse direction is then:

$$\begin{aligned} C_{S_x}(\Delta x) &= K_x sinc^2(\pi \Delta x \xi_0) \otimes sinc^2(\pi \Delta x \xi_0) \\ &= [K_x/(\pi \Delta x)^2][1 - \mathrm{sinc}(2\pi \Delta x \xi_0)] \end{aligned} \tag{7.70}$$

with K_x a normalization factor.
Regarding the autocovariance along the longitudinal direction, we should first define the longitudinal point spread function. If, for simplicity, we assume the shape of the pulse envelope to be Gaussian $\sim (0, \sigma_z^2)$, then

$$h(z) = \frac{1}{2\pi\sigma_z^2} \exp(-\frac{z^2}{2\sigma_z^2}) \tag{7.71}$$

and the autocovariance becomes

$$C_{Sz}(\Delta z) = K_z \exp\left[-\frac{\Delta z^2}{4\sigma_z^2}\right] \tag{7.72}$$

with K_z a normalization factor.

With the knowledge about the autocovariance matrix in the transverse and longitudinal direction, we can define the speckle spot size [123,128]. In fact, the speckle size along the transverse direction, δ_x, and along the longitudinal direction δ_z, are defined as follows

$$\delta_x = \int_{-\infty}^{+\infty} C_{S_x}(\Delta x)/C_x(0) d(\Delta x) \tag{7.73}$$

$$\delta_z = \int_{-\infty}^{+\infty} C_{S_z}(\Delta z)/C_z(0) d(\Delta z) \tag{7.74}$$

For a rectangular transducer the lateral and axial correlation cell size are [59]

$$\delta_x = \frac{0.87}{\xi_0} \tag{7.75}$$

$$\delta_z = 0.91\ \frac{c}{\Delta f} \tag{7.76}$$

with c the speed of sound and Δf the frequency bandwidth. From 7.75 and 7.76 we can see that the speckle size in the transverse direction is proportional to the beam width, while in the longitudinal direction is inversely proportional to the bandwidth. That means that the speckle size is comparable to the resolution cell size.

The point spread function is not spatially invariant. Far from the focal region, the factorization in 7.67 does not hold, which complicates the detailed mathematical description of the speckle correlation, but not the approximate equality of speckle spot and resolution cell sizes as a result of 7.66.

7.4.3 Partially developed speckle and speckle from few scatterers

Thus far, we assumed that the density of microscopic scattering events was sufficiently high that the phase of the signal was randomized within one resolution cell. In practical ultrasonic imaging applications, this condition is often not met: the speckle is "partially developed." The assumptions of the central limit theorem are not fulfilled any longer, and the real and imaginary parts do not have a Gaussian distribution anymore. Different statistical models have to be applied to describe the signal [129]. One circumstance in which this occurs was discussed in the previous section: presence of strong, resolved reflectors or correlated scattering structures giving rise to a constant phasor background.

We briefly discuss here a few more special cases for which the speckle statistics can be computed.

If we have a finite number of random scatteres, we can consider the problem as an N-dimensional random walk problem, with N a finite number. Assume again that the N phasors have independent phase and amplitude and that the phase is uniformly distributed. Recalling 7.1-7.3, and using the same definitions as before, we can write the complex field S as

$$S = \sum_{n=1}^{N} \alpha_n e^{i\varphi_n} = S_r + iS_i = Ae^{i\Phi} \tag{7.77}$$

The joint characteristic function of S_r and S_i is

$$M_{S_r,S_i}(\omega_1, \omega_2, N) = E\left[e^{i(\omega_1 S_r + \omega_2 S_i)}\right] = \int_0^{\infty}\int_{-\pi}^{\pi} e^{i(\omega_1 S_r + \omega_2 S_i)}\, p_{\alpha_n,\varphi_n} d\,\varphi_n d\alpha_n \tag{7.78}$$

where $p_{\alpha n,\varphi n}$ is the joint probability distribution of the amplitude and the phase of the individual scatterer; since S_r and S_i depend on α_n and φ_n only, the integration over S can be replaced by the phasor variables directly. Note that the characteristic function is a function of the number of scatterers N.

If we define the polar coordinates in the plane $(\omega_1\omega_2)$ through ω_1=$\Omega\cos\chi$ and ω_2=$\Omega\sin\chi$, we can rewrite 7.78 as

$$M_{S_r,S_i}(\omega_1\omega_2, N) = \int_0^{\infty} \prod_{n=1}^{N} J_0(\alpha_n\Omega) p_{\alpha_n}\, d\alpha_n \tag{7.79}$$

with J_0 the Bessel function of the first kind and order zero. Knowing that the scatterer amplitudes are independent and identically distributed, we obtain

$$M_{S_r,S_i}(\omega_1\omega_2, N) = \left[\int_0^{\infty} J_0(\alpha\Omega) p_\alpha d\alpha\right]^N \tag{7.80}$$

From 7.80 we can note that, in order to compute the distributions of the phase and amplitude of the complex field, we need to define the probability density function p_α of the scatterer amplitude α. This dependence arises because for small N we cannot rely on the central limit theorem to produce Gaussian statistics. The interesting consequence of this complication is that for non-Rayleigh-distributed speckle, we can infer properties of the scattering medium from the speckle distribution. It is possible to demonstrate that the K distribution is a suitable model for p_α in many media. It is defined as follows

$$p_\alpha = \frac{2b}{\Gamma(\upsilon + 1)}\left(\frac{b\alpha}{2}\right)^{\upsilon+1} K_\upsilon(b\alpha) \quad with\ \alpha \geq 0, \upsilon \geq -1 \tag{7.81}$$

$$b = 2\sqrt{\frac{N(\upsilon + 1)}{E[\alpha^2]}}$$

where $K_\upsilon(\cdot)$ is the modified Bessel function of the second kind and order υ and $\Gamma(\cdot)$ is the Gamma function. By computing the characteristic function $M_{S_r,S_i}(\omega_1\ \omega_2,N)$ using the K distributed p_α and inverting to get the joint density function of the envelope A and phase Φ, we obtain

$$p_{A,\Phi} = \frac{1}{2\pi}\frac{2b}{\Gamma(Q)}\left(\frac{bA}{2}\right)^{Q} K_{Q-1}(b\alpha)\ \ for\ A > 0 \tag{7.82}$$

where we have substituted Q=$N(1+\upsilon)$, and so $b = 2\sqrt{\frac{Q}{E[A^2]}}$. Computing the marginal densities, we obtain

$$p_A = \frac{2b}{\Gamma(Q)}\left(\frac{bA}{2}\right)^{Q} K_{Q-1}(bA) \qquad \text{for } A > 0 \tag{7.83}$$

$$p_\pi = \frac{1}{2\pi} \qquad -\pi \leq 0 \leq \pi \qquad 7.84$$

Analysis of the parameters of the K distribution can provide information on the number of scatterers and on the scattering section. This is unlike the statistics of fully developed speckle, which only depends on the mean amplitude. The parameter υ represents the skewness of the distribution. For υ approaching infinity, p_α approaches a Rayleigh distribution while for υ approaching -1, p_α approaches a lognormal distribution. Therefore, we can appreciate the generality of the K distribution since, it is possible to change the distribution of the scatterer amplitude by changing υ. Knowing the meaning of the parameter υ, it is possible to understand the physical significance of Q. For υ approaching -1, Q will be very small even if N is very large. Therefore, Q represents the effective number of scatterers per resolution cell. Thus Q is a measure of both the number of scatterers and the variation in scattering cross-section [129]. Figure 7.10 shows plots of the K-distribution for different effective numbers of scatterers Q, demonstrating that for Q>10 the difference with the Rayleigh distribution becomes small.

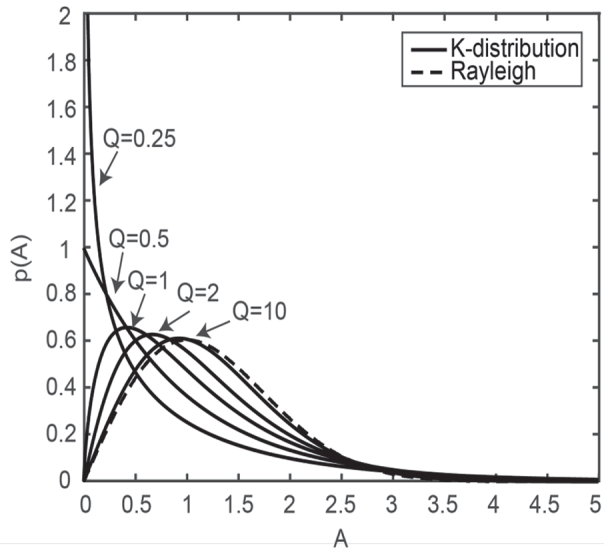

Figure 7.10 K-distribution for different effective number of scatterers .

7.5 EFFECT OF POST-PROCESSING ON FIRST AND SECOND ORDER STATISTICS

In standard B-mode imaging, the ultrasound signal detected by the transducer is usually processed non- linearly in order to compress the incoming signal having wide range into a smaller signal with reduced range. This is done to overcome the problem of displaying a wide range signal using too many gray-scale levels that would not be distinguished by the observer [64]. Therefore, compression is needed in order to be able to display the images on the

commercially available systems. This non-linear postprocessing of the incoming signal will affect its statistics, leading to changes in the probability density functions. It is therefore important to study the effect of these compression mechanisms on the previously derived statistics. The most common way of compressing ultrasound data is to use a logarithmic amplifier. More in detail, the received signal amplitude A will be scaled and shifted according to the following expression:

$$A' = c \ln A + d \tag{7.85}$$

where A' is the post processing amplitude and c and d are constants associated to the dynamic range and the gain setting respectively [130]. If A_{min} and A_{max} are the minimum and maximum respectively of the input A which lead to A'_{min} and A'_{max} and of the output A', then

$$c = \frac{A'_{max} - A'_{min}}{\ln(A_{max} - A_{min})} \tag{7.86}$$

Knowing that the dynamic range is given by

$$DR = 20 \log\left(\frac{A_{max}}{A_{min}}\right) \tag{7.87}$$

We can rewrite 7.86 such that

$$c = \frac{20}{DR \ln(10)}(A'_{max} - A'_{min}) \tag{7.88}$$

Therefore, knowing the input and output dynamic range, it is possible to estimate the logarithmic amplifier parameter c.

To compute the probability density function of we can use the following expression [131]

$$p(A') = p(A)\left(\frac{dA'}{dA}\right)^{-1} \tag{7.89}$$

with the probability density function of A given by 7.20. We then get

$$\frac{dA'}{dA} = \frac{c}{A} = \frac{c}{e^{\left(\frac{A'-d}{c}\right)}} \tag{7.90}$$

And $p(A')$ becomes

$$p(A') = \frac{1}{\beta} e^{(-g-e^{-g})} \tag{7.91}$$

with

$$g = \frac{\alpha - A'}{\beta} \qquad \alpha = \frac{c \log(2\sigma^2)}{2} + d \qquad \beta = \frac{c}{2} \tag{7.92}$$

Equation 7.91 is a double exponential (Fisher-Tippet) [130]. Note that α,c, and d are functions of the standard deviation σ of the Rayleigh distribution. Therefore, we can compute the mean and variance of A' as

$$E[A'] = c\left(\frac{\ln 2}{2} + \ln\sigma - \frac{\gamma}{2}\right) + d \tag{7.93}$$

$$E[(A' - E[A'])^2] = \frac{\pi^2 c^2}{24} \tag{7.94}$$

where γ is the Euler constant ($\gamma \approx 0.5772$). Figure 7.11 shows the effect of log-compression on the Rayleigh distribution.

Knowing the variance of the log compressed data we can derive the values of the parameters c. Assuming the known variance is equal to v, we get:

$$c = \frac{2\sqrt{6}}{\pi}\sqrt{v} \tag{7.95}$$

This means that, for fully developed speckle, we can derive the amplification parameter from the signal statistics (the variance).

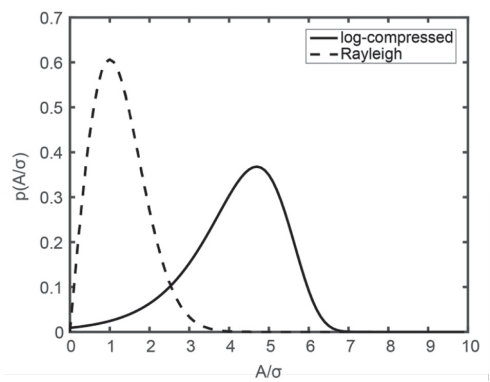

Figure 7.11 Rayleigh distribution and log-compressed distribution with c=2 and d=4.

Acknowledgments

We would like to thank Prof. J.W. Goodman for discussions on the sum of Rayleigh distributed magnitudes and sharing his insights in this problem. GvS acknowledges Prof. D.D. Sampson and the School of Electrical, Electronic and Computer Engineering of the University of Western Australia for hosting him while working on this chapter, supported by a grant from the Raine Foundation. He enjoyed discussions on the finer details of OCT speckle with David Sampson and Andrea Curatolo.

Chapter 8

Structured Ultrasound Microscopy

Based on:

Jovana Janjic, Pieter Kruizinga, Pim van der Meulen, Geert Springeling Frits Mastik, Geert Leus, Johan G. Bosch, Antonius F. W. van der Steen, Gijs van Soest, Structured Ultrasound Microscopy, *submitted to Applied Physics Letters.*

ABSTRACT

We present a new form of acoustic microscopy, called Structured Ultrasound Microscopy (SUM). It creates a volumetric image by recording reflected echoes of ultrasound waves with a structured phase front using a moving single-element transducer and solving an inverse scattering problem. A priori knowledge of the acoustic field produced by the single element allows to relate the received echoes to a 3D scatter map within the acoustic beam itself, leading to an isotropic resolution at all depths. An aberration mask in front of the acoustic element imposes the phase structure, broadening the beam and breaking the spatial coherence between different voxels at equal acoustic propagation delay, increasing the uniqueness of the scattering problem. By translating the transducer across the 3D volume, we synthetically enlarge the imaging aperture by using multiple overlapping and spatially sparsely sampled measurements to solve for the entire image. In this paper we explain the SUM technique and successfully demonstrate microscopic imaging at 20 MHz of a $2.3 \times 2.3 \times 1.2$ mm object in water, with an isotropic resolution below 100 μm. The proposed approach allows for wide-field 3D imaging at isotropic microscopic resolution using a very small unfocused ultrasound sensor and multiple spatially sparsely sampled measurements. This technique may find applications in many other fields where space is constrained, device simplicity is desired, and wide-field isotropic high-resolution imaging is required.

8.1 INTRODUCTION

High-resolution wide-field ultrasound microscopy is of great interest for different applications ranging from non-destructive testing of small electronic components [132] to tissue microscopy [133-136] and intravascular imaging [137-139]. Scanning acoustic microscopy (SAM) enables high resolution imaging using a high frequency, tightly-focused ultrasound transducer. Image data is acquired by scanning the transducer or the object under study in two dimensions while acquiring pulse-echo A-lines [140]. The imaged volume is obtained by mapping the backscattered echoes to a 3D image grid. The lateral resolution depends on the numerical aperture and varies over the depth, with the highest resolution achieved at the focal distance; the axial resolution is proportional to the acoustic bandwidth. The depth-varying, anisotropic resolution, the large number of sampling points needed for full 3D coverage and the complexity of manufacturing high-frequency focused transducers limit the utility of SAM in many practical applications. In this work, we propose Structured Ultrasound Microscopy (SUM), a wide-field imaging technique with isotropic high resolution. SUM exploits the spatial a priori information of a structured ultrasound beam and achieves volumetric imaging with a set of measurements spatially sampled on a sparse grid.

Computational imaging has attracted broad interest recently, as it has enabled simultaneous wide field-of-view and high image resolution, often realized in compact, simple imaging systems. It forms an image by solving an inverse mathematical problem, using a priori knowledge of the imaging system. Some technologies developed in the past decade include synthetic aperture microscopy [141], Fourier ptychographic microscopy [142,143] and lensless imaging [144,145]. Optical synthetic aperture approaches rely on scanning the frequency space [141] using holographic [146] or interferometric [147,148] techniques. A computational step is then employed to reconstruct the image. Synthetic aperture techniques were developed for radar to improve resolution by moving the recording system (e.g. mounted on an airplane) and combining multiple overlapping signals [149]. Image resolution is determined by the compounded aperture, which is wider than the real aperture.

Lensless optical imaging systems achieve high-resolution, wide-field imaging [144,145] by replacing the lens with an aperture mask that modulates the illumination and encodes high-frequency spatial information in the available aperture. The use of aperture masks to encode spatial information has also been considered in ultrasonic imaging [150-152]. The mask scrambles the incident sound field, destroying the spatial coherence, similar to speckle formation. The resulting fine-scale structure in the beam enables enhanced resolution imaging, as in imaging through scattering media [153].

Recently, we showed that knowledge of the complex ultrasound field created by the aperture mask allows 3D imaging using only one sensor [152]. SUM is based on that concept: acoustic microscopy with phase-encoded insonification. It employs a 3D-printed mask to encode 3D

spatial information in the acoustic delay, and inverse modeling of the imaging system to achieve wide-field high-resolution volumetric imaging. In this way, we can overcome the limitations of SAM, where dense sampling is required and high resolution is achieved only at the focal region of the transducer. We also investigate synthetic aperture microscopy with computational reconstruction, without an aperture mask (which we call Reconstructed Ultrasound Microscopy; RUM), to independently assess the benefits of computational reconstruction and beam scrambling.

8.2 METHODS

The mathematical model for computational reconstruction [152] describes the pulse-echo signal for each voxel in the imaging region for a given ultrasound field (with and without the mask), scanned over a sparsely sampled grid. We denote this as the system matrix $\boldsymbol{H}$. Volumetric imaging is achieved by inversion of this model. We denote the measurement vector $\boldsymbol{u}$, and we assume it is linearly related to the image $\boldsymbol{v}$ through the following equation:

$$\boldsymbol{u} = \boldsymbol{H}\boldsymbol{v} + \boldsymbol{n} \tag{8.1}$$

where $\boldsymbol{n}$ is additive noise. The image $\boldsymbol{v}$, containing the scattering amplitude per voxel, can be computed with linear inversion methods, such as regularized least squares inversion using the LSQR algorithm [152].

As shown in Figure 8.1, a custom-built unfocused single-element piezoelectric ultrasound transducer (20 MHz, 1 mm diameter) was mounted on a rigid tube and clamped on a motorized positioning stage (Newport Corporation, CA, USA). The coding mask was fabricated using stereolithography (Nanoscribe, Karlsruhe, Germany). It consisted of square pillars (80 μm sides; comparable to the wavelength in water) with random heights (between 40 and 320 μm). This mask effects local delays of up to several wavelengths to the wave field. The speed of sound in the printed resin is 2500-2700 m/s [154]. The mask was slightly larger than the transducer to facilitate assembly. After mounting the mask on the transducer we covered it with silicone to improve the mechanical stability. The transducer was excited with a 10 ns, 60 V unipolar pulse (Avtech Electrosystems Ltd, USA). After amplification by 40 dB (MITEQ, USA) and bandpass filtering ($10–30$ MHz, 5^{th} order Butterworth), the received echo was digitized at 400 MS/s and 12-bit resolution (Agilent Technologies, USA). A custom-built expander/limiter electrically separated the transmit and the receive signal path. All the measurements were performed in a water tank at room temperature.

The spatiotemporal impulse response of the two transducers (with and without mask) was mapped by first scanning a plane perpendicular to the propagation direction, using a 75 μm needle hydrophone (Precision Acoustics, UK). The spatiotemporal impulses were acquired

on a 4 x 4 mm grid with dense 30 µm spacing at a distance of 900 µm from the transducer. Using the angular spectrum of the measurements in this plane, we then computed the forward field impulse responses of the voxels in any parallel plane [155]. Finally, assuming reciprocity, we autoconvolved the forward field impulse-response of each pixel to get their scattered echo signals. The resulting traces are then used to populate the system matrix $\boldsymbol{H}$. All the signal processing is implemented in Matlab 2016b (The MathWorks, MA, USA). To reduce the computational complexity, we chose a sparse Fourier-domain representation of each voxel signal (bandlimited between 15 and 25 MHz).

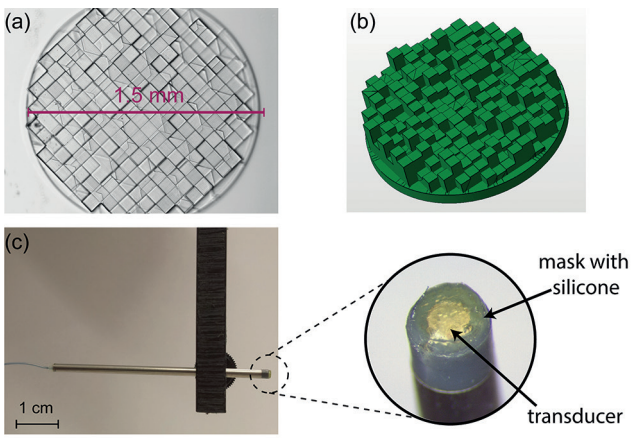

Figure 8.1 (a) Top view of the aperture mask imaged with a microscope, (b) schematic drawing of the aperture mask. (c) transducer with the mask mounted on the translation stage.

8.3 RESULTS

The ultrasound field transmitted by the single element transducer without mask exhibits a mild natural focus at approximately 3 mm (Figure 8.2). When the mask is placed in front of the transducer, the scrambled phase of the ultrasound field leads to a complex interference pattern. This interference pattern reduces the similarity between nearby voxels resulting in pulse-echo signals that are highly uncorrelated (Figure 3(a)), and increases the field-of-view (Figure 8.3(b)). For full volumetric imaging without (RUM) and with mask (SUM), we acquire measurements at different locations, similar to SAM. However, in SAM the width of the focal region determines the lateral resolution in the plane perpendicular to the ultrasound propagation axis (the x,y plane). This means that high lateral resolution is achieved by a narrow beam and a dense spatial sampling. In both RUM and SUM we resolve the x and y components in the beam by exploiting the ultrasound spatial information in the imaging plane, without the need for a tightly focused beam. In SUM, the mask produces a broader beam, and so fewer measurements are required to cover the same area compared to SAM and RUM. Even with sparse spatial sampling, there

is significant overlap between the beams, further reducing the similarity of the voxels (Figure 8.3(c)).

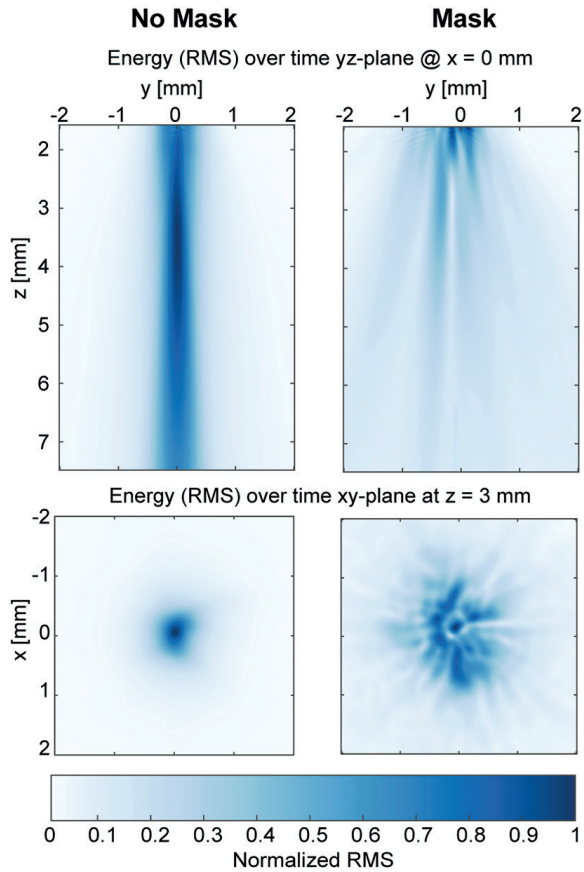

Figure 8.2 Ultrasound field transmitted from the sensor without (left column) and with the aperture mask (right column). Propagating medium is water.

We compute the absolute correlations between the pulse-echo signals $\boldsymbol{H}$ in that correspond to the imaging voxels in a single plane for a given measurement pattern. Figure 8.4(a) shows the correlations between the pulse- echo signal of one voxel (scatterer) and the pulse-echo signals of all other voxels in the analysis plane, with a scanning step size of $300\ \mu\mathrm{m}$ both in x and y directions for both the case without (RUM) and with (SUM) the mask. The correlation is always high for neighboring voxels, making it difficult to resolve two different scatterers, and decreases as one moves further away from the scatterer. We observe that with the mask, high image resolution is achieved by fast decorrelation for increasing distances from the scatterer, at the cost of a slight increase in background clutter. We show the absolute correlation for increasing voxel-to-scatterer distance, averaged in the scan plane, in Figure 8.4(b).

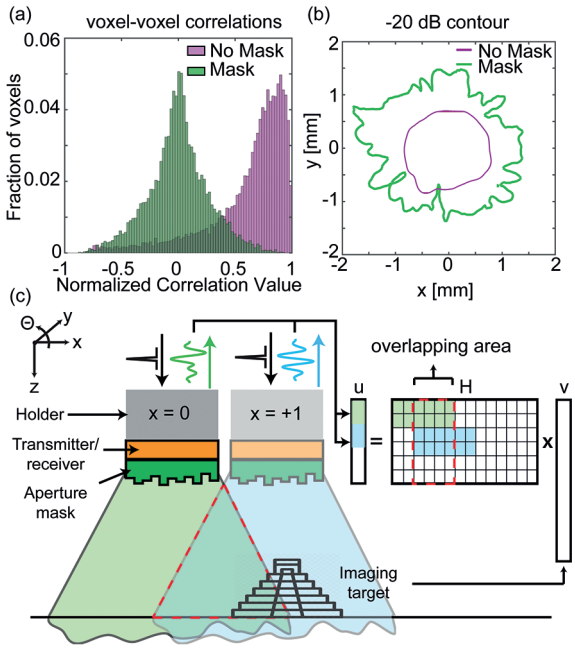

Figure 8.3 (a) voxel-to-voxel correlation distribution between all the voxels in one *x,y* plane and (b) -20dB contour plot of the ultrasound beam in *x,y*-plane for both the case without and with the mask; (c) schematic of the imaging procedure.

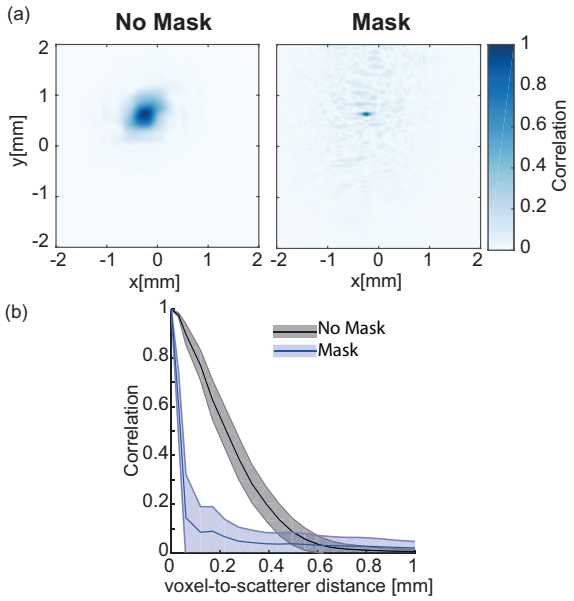

Figure 8.4 Analysis of the in-plane correlation. (a) Correlation of one reference voxel (located at x=-0.5 and y=0.5 mm) for the case without and with the mask, using a scan step size of 300 μm; (b) average of all the voxel correlations versus pixel-to-scatterer distance (mean ± standard deviation).

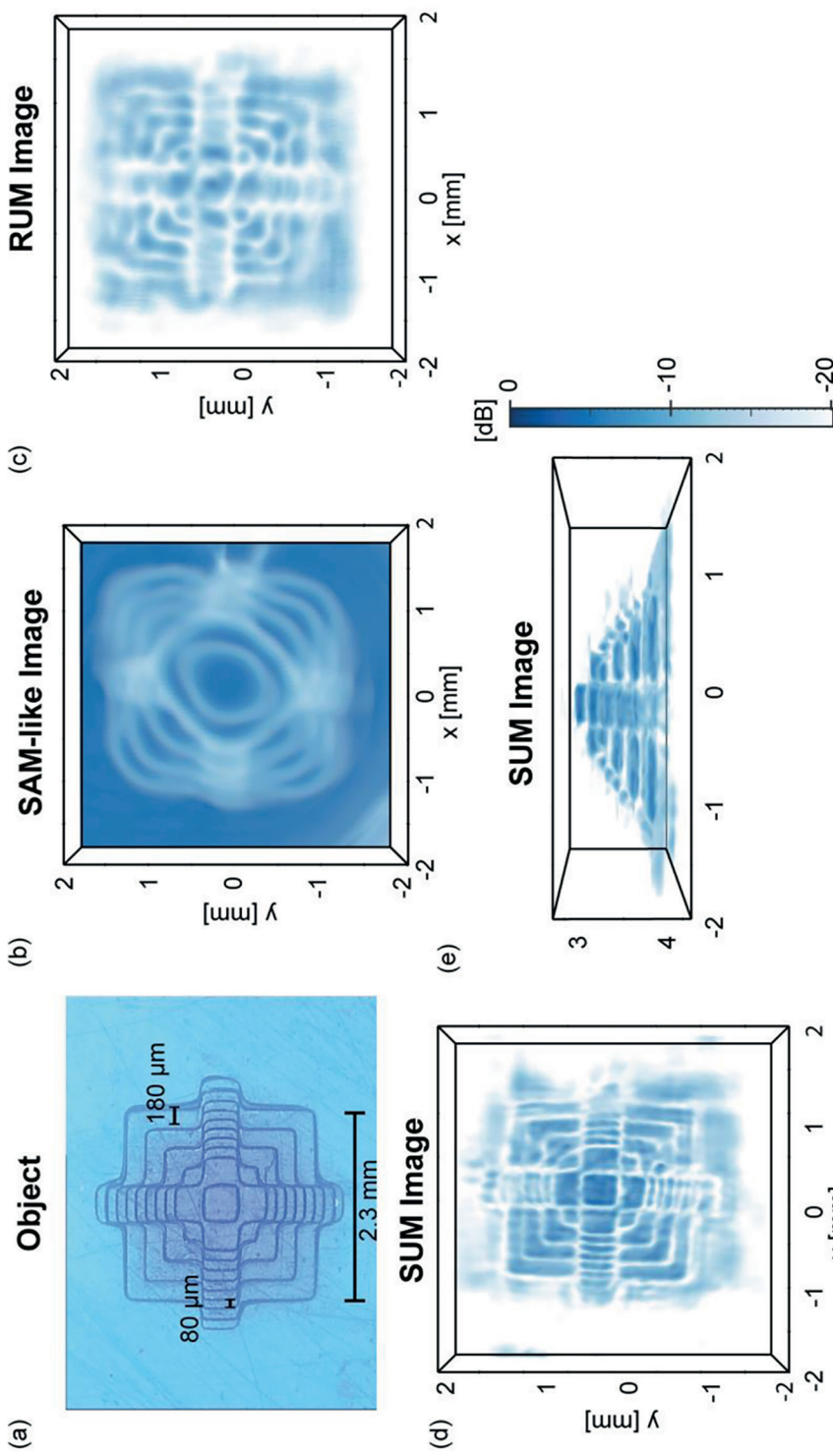

Figure 8.5 (a) top view of the 3D object imaged with a microscope; reconstructed image using (b) conventional SAM-like imaging, (c) RUM and (d)-(e) SUM.

We experimentally demonstrate computational ultrasound for high-resolution wide-field imaging of a 3D printed object with dimensions $2.3\times2.3\times1.2$ mm (Figure 8.5(a)). The object was glued on rubber and submerged in water at 3 mm from the transducer. Reconstruction of the image by mapping the pulse-echo signal envelope to a 3D imaging grid by scanning the region of interest (4×4 mm) with a 30 μm step (SAM-like imaging) results in a poor image (Figure 8.5(b)). Next, we perform a computational reconstruction without and with mask, using a randomly selected subset containing 40% of the densely sampled measurements and using the LSQR algorithm (Figure 8.5(c)-(e)).

Both RUM and SUM result in highly improved resolution. Even without the mask (RUM), the small imperfections in the transducer introduce spatial heterogeneity in the beam allowing reconstruction of the object with recognizable features down to ~150 μm. When the mask is used (SUM), the image fidelity is further improved, with the smallest structures (80 μm) successfully resolved (Figure 8.5(d)-(e)).

8.4 DISCUSSION AND CONCLUSION

This result also demonstrates that exploiting the spatial information of the ultrasound field results in isotropic resolution. Increased resolution and field-of-view are obtained by encoding 3D spatial information on echo delays using an aperture mask. The gain in resolution comes at the expense of a reduction in SNR by approximately 10 dB. We attribute this SNR loss to the acoustic energy being emitted into a larger volume and to the impedance mismatch of the transducer-mask-water interfaces.

Improvement in the SNR can be achieved by optimizing mask materials and geometry. In this work we used a mask that was 3D printed, hence limiting the material choice to resins suitable for the specific printer. Beside the choice of mask material, accurate optimization of the mask geometry should be performed [156]. By optimizing the mask geometry more spatial diversity could be introduced, such that unique signals are associated to each voxel, leading to a model matrix $\boldsymbol{H}$ with highly uncorrelated columns. This will enable recovery of the 3D image with microscopic resolution using fewer measurements. Moreover, if the $\boldsymbol{H}$ matrix is characterized with high accuracy, better image reconstruction can be achieved. The hydrophone used in our measurements had a 75 μm sensor, equal to the wavelength of the 20 MHz acoustic waves in water. Subwavelength sampling of the ultrasound field will lead to a more complete characterization of $\boldsymbol{H}$, improving image resolution.

The imaging method that we propose here could also be applied to irregular scanning patterns if the transducer position is known at every scan. Compact tracking techniques, such as optics-based systems [48,49], may enable the implementation of SUM in minimally-invasive medical imaging devices. Catheter-based imaging has demonstrated to be a powerful tool for guidance

of cardiac and vascular interventions [157], but present-day imaging catheters do not achieve comprehensive, high-resolution microscopy. SUM hardware is small, cheap, simple, and it is compatible with miniature disposable devices.

In conclusion, SUM is a new form of acoustic microscopy that enables wide-field isotropic high-resolution imaging with a simple unfocused ultrasound transducer and a cheap coding mask. This technique may find application in many fields where space is constrained and wide-field high-resolution imaging is required.

Acknowledgement
This research is supported by the NWO Domain Applied and Engineering Sciences (formerly STW) (grant number 12710 and 14926), which is partly funded by the Ministry of Economic Affairs.

We are grateful to Jeroen Mesman at Leiden University for fabricating the acoustic mask.

Chapter 9

Discussion and Conclusion

9.1 OVERVIEW

Minimally invasive interventions are the preferred choice in different medical fields due to the smaller incisions and the quicker recovery time compared to conventional open surgeries. Image guidance during minimally invasive interventions allows the physician to gain information over the working field and the location of the tools with respect to the anatomy. Imaging helps also to monitor the effects of certain procedures such as cardiac transseptal puncture, heart valve replacement and chronic total occlusion (CTO) crossing. Although many solutions have been investigated and some minimally invasive imaging devices have entered the market, minimally invasive forward-looking (FL) devices are still under development.

This thesis proposes several solutions to achieve minimally invasive 3D forward-looking ultrasound imaging focusing on two major approaches. The first approach consists in developing miniaturized multi-element transducers with optimal acoustic design and smart interconnections. The second approach consists in the development of simple single-element transducers that can be easily integrated in minimally invasive devices and that can be used to achieve forward-looking volumetric imaging by combining ultrasound information with steering mechanisms and a shape sensing system. In this chapter we give an overview of the results achieved and we discuss the applicability of the proposed solutions in image guidance of minimally invasive interventions. Some remaining challenges and future work are also discussed.

9.2 TRANSDUCER GEOMETRY OPTIMIZATION

For every ultrasound transducer, independent on its application, geometry is crucial for optimal acoustic performances. The width-to-thickness ratio of a transducer element should be as small as possible for uniform surface motion. However, if the width is too small, poor radiation impedance is obtained. For high frequency transducers, which are usually preferred for image guidance in minimally invasive interventions, it is very difficult to achieve small width-to-thickness ratios, with the result that non-piston like modes can occur. To restore optimal vibration of wide elements, subdicing was investigated through finite element simulations (Chapter 2). Subdicing elements having a width greater than 0.6 times the wavelength improves the radiation impedance, the time and frequency response and the directivity. Moreover, to achieve the most significant improvements it is sufficient to subdice 70% of the total element thickness, hence making the transducer fabrication process mechanically stable. By optimizing transducer geometry, acoustically efficient transducers can be achieved resulting in images with improved signal-to-noise ratio and improved resolution.

9.3 2D MATRIX ARRAY FOR MINIMALLY INVASIVE 3D FORWARD-LOOKING IMAGING

Several multi-element transducer arrays have been investigated for FL imaging, from linear arrays generating 2D images to 2D matrix arrays for volumetric imaging [29-35,38-44]. To electrically address multiple elements within the limited space of a catheter, electronic circuits with pulsers and multiplexers should be considered. In this way the number of cables that need to fit in the catheter shaft is reduced, leaving space for other components such as steering mechanisms, guidewires and other interventional tools. Application specific integrated circuits (ASICs) have been reported in the literature to reduce the cable count in FL devices, but they still require more than 10 connections [42,43,158]. Efforts have been made in modifying commercially available side-looking intravascular catheters to provide forward-looking imaging [34,76], but SNR and power dissipation are of concern, since only a limited aperture consisting of an annulus of array elements is used to achieve volumetric imaging.

In Chapter 3 we propose a 2D matrix array mounted on top of an ASIC that addresses 80 PZT elements with only 4 micro-coaxial cables. We simulated different transducer designs that could fit the limited aperture at the tip of a catheter and we fabricated the final design on a custom designed ASIC. We successfully characterized acoustically the transducer and demonstrated 3D FL imaging with only 4 cables. The chip and the transducer occupy a donut-shape area with an outer diameter of 1.5 mm and an inner lumen of 0.5 mm. These dimensions are suitable for catheter integration with the inner lumen available for a guidewire.

9.4 SINGLE-ELEMENT MINIMALLY INVASIVE 3D FORWARD-LOOKING IMAGING

Besides considering multi-element arrays, in this thesis we investigated approaches where only a single-element transducer is used to achieve 3D FL imaging. It is well known that a single-element transducer can only provide an A-line, hence additional source of information is required to achieve volumetric imaging. To this end, we exploited the combination of steering mechanisms and shape sensing devices together with single-element ultrasound transducers. We envisioned that by combining ultrasound and position information while steering the device, volumetric imaging could be achieved. Smart algorithms and processing methods are required to successfully elaborate the acquired information into volumetric images.

Commercially available minimally invasive instruments are not capable to successfully navigate through complex shapes. Several steerable devices have been proposed in the literature [96,159,160] but they are quite bulky. We therefore considered novel steerable devices and in Chapter 4 we present a novel miniature tip design with 8 Degrees of Freedom (DOF). A prototype of the device having an outer diameter of 2 mm has been manufactured and a single

element transducer together with an optical fiber for shape sensing have been successfully integrated. We demonstrated that, while manually steering the tip, ultrasound and shape data can be acquired simultaneously, providing information over the location of a wire phantom in 3D space. However, since steering is manual and limited by the design of the catheter, sparse and irregularly sampled ultrasound data are obtained. To interpolate the sparse ultrasound data, we implemented adaptive normalized convolution (Chapter 5), an algorithm that employs an anisotropic Gaussian kernel to fill the empty spaces in the sparse image obtained by spatially mapping the received echoes. After optimizing its dimensions, the kernel is rotated according to the local direction of the scanning pattern allowing to reconstruct features that are not recognizable in the sparse images. With this approach we successfully demonstrated FL imaging of the surface of a tissue mimicking phantom and an *ex-vivo* carotid plaque using a clinically available steerable device. The use of a clinically employed steerable device ensures easier translation of the novel imaging concept into the clinics. We further extended the sparse image reconstruction method to 3D by imaging structures in an *ex-vivo* pig heart (Chapter 6). Here the kernel is dynamically changing depending on the spatial density of the information. The resolution of the images depends on the scanning pattern and on the kernel shape and size. The resolution changes spatially, being limited by the smoothing kernel in the sparse areas and by the scanning pattern in the dense areas. The effective resolution is in the range of the kernel dimensions and an analytical description is not possible due to the non-uniform sampling of the data.

A way to improve the resolution is to exploit further the ultrasound beam and relate the received echoes to a 3D scatter map within a structured acoustic beam (Chapter 8), of which speckle is a well-known phenomenon (Chapter 7). By placing a coding mask in front of a single-element transducer, the phase uniformity is lost and unique signals are associated to each imaging voxel. A mathematical model is then developed to exploit the scattering object information in the measurement and the LSQR algorithm is used to solve the problem. By translating the imaging sensor, we can enlarge synthetically the field of view achieving 3D FL imaging with microscopic and isotropic resolution.

9.5 LIMITATIONS AND FUTURE PERSPECTIVES

The solutions proposed in this thesis show the potential of achieving minimally invasive 3D FL ultrasound imaging in several applications.

The 2D matrix transducer presented in Chapter 3 requires only four coaxial cables and has a total outer diameter of 1.5 mm. The small dimensions and reduced cable count will enable easier integration into catheters or other instruments suitable for minimally invasive procedures. Integration of the ultrasound transducer is further simplified in the solutions presented in Chapters 4-6 and 8 where only a single element is employed. Although single-element

transducers require additional sources of information to achieve FL volumetric imaging, this thesis demonstrates that smart designs of novel steering mechanisms and the use of optical shape sensing systems can be used to explore possibilities for devices with small form factors. With future developments towards robust integration, it will be possible to apply the proposed solutions in *in-vivo* settings taking into consideration motion effects and the presence of additional instruments in the imaging field of view, e.g. guidewires.

In prospect, the solutions presented in this thesis may lead to simple and versatile image guidance with steerable catheters that dynamically build up a volumetric image of the working field in real time. FL volumetric imaging could provide accurate representation of the anatomy and generate information regarding the location of therapeutic devices. This will aid the interventionalist to navigate towards the site of intervention while moving the instruments.

The high resolution obtained with SUM in Chapter 8 indicates that accurate representation of the geometry of tiny structures can be achieved. For example, soft spots in a calcified CTO could be visualized and image guidance while maneuvering the guidewire towards it could be achieved.

Moreover, FL ultrasound imaging could be registered to pre-intervention CT scans by exploiting the shape sensing information, hence minimizing the radiation exposure during the intervention.

The efficient device designs and smart algorithms shown in this thesis together with future research and technological development may lead to image guidance in minimally invasive procedures with approaches that, both from the imaging and the technical point of view, look forward.

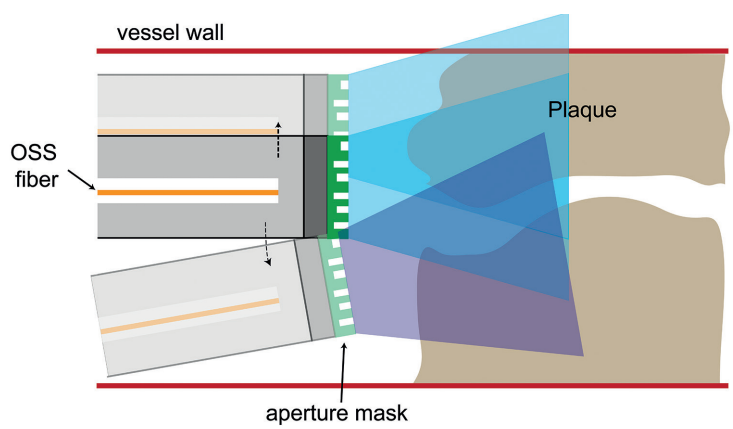

Figure 9.1 Envisioned FL-IVUS with SUM

References

[1] L. H. Cohn, Fifty years of open-heart surgery, *Circulation,* vol. 107, pp. 2168-70, May 6 2003.

[2] A. Diamantis, E. Magiorkinis, and H. Koutselini, Fine-needle aspiration (FNA) biopsy: historical aspects, *Folia Histochem Cytobiol,* vol. 47, pp. 191-7, 2009.

[3] S. D. S. Peter and G. W. Holcomb Iii, History of Minimally Invasive Surgery, *Atlas of Pediatric Laparoscopy and Thoracoscopy,* p. 1, 2008.

[4] S. J. Spaner and G. L. Warnock, A brief history of endoscopy, laparoscopy, and laparoscopic surgery, *Journal of Laparoendoscopic & Advanced Surgical Techniques-Part A,* vol. 7, pp. 369-373, Dec 1997.

[5] R. L. Mueller and T. A. Sanborn, The history of interventional cardiology: cardiac catheterization, angioplasty, and related interventions, *Am Heart J,* vol. 129, pp. 146-72, Jan 1995.

[6] M. Barton, J. Gruntzig, M. Husmann, and J. Rosch, Balloon Angioplasty - The Legacy of Andreas Gruntzig, M.D. (1939-1985), *Front Cardiovasc Med,* vol. 1, p. 15, 2014.

[7] M. A. Cooper, S. Hutfless, D. L. Segev, A. Ibrahim, H. Lyu, and M. A. Makary, Hospital level under-utilization of minimally invasive surgery in the United States: retrospective review, *BMJ,* vol. 349, p. g4198, Jul 8 2014.

[8] C. T. Sherman, F. Litvack, W. Grundfest, M. Lee, A. Hickey, A. Chaux, R. Kass, C. Blanche, J. Matloff, L. Morgenstern, W. Ganz, H.J.C. Swan, J. Forrester, Coronary angioscopy in patients with unstable angina pectoris, *N Engl J Med,* vol. 315, pp. 913-9, Oct 9 1986.

[9] M. J. Suter, S. K. Nadkarni, G. Weisz, A. Tanaka, F. A. Jaffer, B. E. Bouma, G. J. Tearney, Intravascular optical imaging technology for investigating the coronary artery, *JACC Cardiovasc Imaging,* vol. 4, pp. 1022-39, Sep 2011.

[10] G. J. Tearney, E. Regar, T. Akasaka, T. Adriaenssens, P. Barlis, H. G. Bezerra, B. Bouma, N. Bruining, J. Cho, S. Chowdhary, M. A. Costa, R. de Silva, J. Dijkstra, C. Di Mario, D. Dudeck, E. Falk, M. D. Feldman, P. Fitzgerald, H. Garcia, N. Gonzalo, J. F. Granada, G. Guagliumi, N. R. Holm, Y. Honda, F. Ikeno, M. Kawasaki, J. Kochman, L. Koltowski, T. Kubo, T. Kume, H. Kyono, C. C. S. Lam, G. Lamouche, D. P. Lee, M. B. Leon, A. Maehara, O. Manfrini, G. S. Mintz, K. Mizuno, M. Morel, S. Nadkarni, H. Okura, H. Otake, A. Pietrasik, F. Prati, L. Räber, M. D. Radu, J. Rieber, M. Riga, A. Rollins, M. Rosenberg, V. Sirbu, P. W.J.C. Serruys, K. Shimada, T. Shinke, J. Shite, E. Siegel, S. Sonada, M. Suter, S. Takarada, A. Tanaka, M. Terashima, T. Troels, S. Uemura, G. J. Ughi, H. M.M. van Beusekom, A. F.W. van der Steen, G. van Es, G. van Soest, R. Virmani, S. Waxman, N. J. Weissman and G. Weisz, Consensus standards for acquisition, measurement, and reporting of intravascular optical coherence tomography studies: a report from the International Working Group for Intravascular Optical Coherence Tomography Standardization and Validation, *J Am Coll Cardiol,* vol. 59, pp. 1058-72, Mar 20 2012.

[11] F. L. Thurstone and O. T. von Ramm, A New Ultrasound Imaging Technique Employing Two-Dimensional Electronic Beam Steering, in *Acoustical Holography: Volume 5*, P. S. Green, Ed., ed Boston, MA: Springer US, 1974, pp. 249-259.

[12] N. Vitulano, V. Pazzano, G. Pelargonio, and M. L. Narducci, Technology update: intracardiac echocardiography - a review of the literature, *Med Devices (Auckl),* vol. 8, pp. 231-9, 2015.

[13] S. Stec, B. Zaborska, M. Sikora-Frac, T. Krynski, and P. Kulakowski, First experience with microprobe transoesophageal echocardiography in non-sedated adults undergoing atrial fibrillation ablation: feasibility study and comparison with intracardiac echocardiography, *Europace,* vol. 13, pp. 51-56, Jan 2011.

[14] M. Taniguchi, T. Akagi, Y. Kijima, H. Ito, and S. Sano, Transcatheter Closure of a Large Atrial Septal Defect under Microprobe Transesophageal Echocardiographic Guidance, *Echocardiography-a Journal of Cardiovascular Ultrasound and Allied Techniques,* vol. 29, pp. E94-E96, Apr 2012.

[15] N. Bom, C. T. Lancee, and F. C. Van Egmond, An ultrasonic intracardiac scanner, *Ultrasonics,* vol. 10, pp. 72-6, Mar 1972.

[16] Acuson Files for 510(k) Clearance With the FDA for the AcuNav(TM) Diagnostic Ultrasound Catheter That Captures Images From Inside the Heart. (1999, September 21).

[17] Z. M. Hijazi, K. Shivkumar, and D. J. Sahn, Intracardiac Echocardiography During Interventional and Electrophysiological Cardiac Catheterization, *Circulation,* vol. 119, pp. 587-U180, Feb 3 2009.

[18] M. O'Donnell, M. J. Eberle, D. N. Stephens, J. L. Litzza, K. San Vicente, and B. M. Shapo, Synthetic phased arrays for intraluminal imaging of coronary arteries, *IEEE Transactions on Ultrasonics, Ferroelectrics, and Frequency Control,* vol. 44, pp. 714-721, 1997.

[19] H. M. Garcia-Garcia, M. A. Costa, and P. W. Serruys, Imaging of coronary atherosclerosis: intravascular ultrasound, *European Heart Journal,* vol. 31, pp. 2456-2469c, Oct 2010.

[20] D. Wildes, W. Lee, B. Haider, S. Cogan, K. Sundaresan, D. M. Mills, C. Yetter, P.H. Hart, C. R. Haun, M. Concepcion, J. Kirkhorn, M. Bitoun, 4-D ICE: A 2-D Array Transducer With Integrated ASIC in a 10-Fr Catheter for Real-Time 3-D Intracardiac Echocardiography, *IEEE Trans Ultrason Ferroelectr Freq Control,* vol. 63, pp. 2159-2173, Dec 2016.

[21] W. Lee, S. F. Idriss, P. D. Wolf, and S. W. Smith, A miniaturized catheter 2-D array for real-time, 3-D intracardiac echo cardiography, *Ieee Transactions on Ultrasonics Ferroelectrics and Frequency Control,* vol. 51, pp. 1334-1346, Oct 2004.

[22] E. D. Light, S. F. Idriss, P. D. Wolf, and S. W. Smith, Real-time three-dimensional intracardiac echocardiography, *Ultrasound in Medicine and Biology,* vol. 27, pp. 1177-1183, Sep 2001.

[23] G. W. Stone, D. E. Kandzari, R. Mehran, A. Colombo, R. S. Schwartz, S. Bailey I. Moussa, P. S. Teirstein, G. Dangas, D. S. Baim, M. Selmon, B. H. Strauss, H. Tamai, T. Suzuki, K. Mitsudo, O. Katoh, D. A. Cox, A. Hoye, G. S. Mintz, E. Grube, L. A. Cannon, N. J. Reifart, M. Reisman, A. Abizaid, J. W. Moses, M. B. Leon, P. W. Serruys, Percutaneous Recanalization of Chronically Occluded Coronary Arteries, *A Consensus Document: Part I,* vol. 112, pp. 2364-2372, 2005.

[24] J. L. Evans, K. H. Ng, M. J. Vonesh, B. L. Kramer, S. N. Meyers, T. A. Mills, B. J. Kane, W. N. Aldrich, Y. T. Jang, P. G. Yock, Arterial imaging with a new forward-viewing intravascular ultrasound catheter, I. Initial studies, *Circulation,* vol. 89, pp. 712-7, Feb 1994.

[25] K. H. Ng, J. L. Evans, M. J. Vonesh, S. N. Meyers, T. A. Mills, B. J. Kane, W. N. Aldrich, Y. T. Jang, P. G. Yock, M. D. Rold, Arterial imaging with a new forward-viewing intravascular ultrasound catheter, II. Three-dimensional reconstruction and display of data, *Circulation,* vol. 89, pp. 718-23, Feb 1994.

[26] D. H. Liang and B. S. Hu. Forward viewing ultrasonic imaging catheter. U.S. Patent No. 5,651,366. 29 Jul. 1997.

[27] J. H. Rogers, Forward-Looking IVUS in Chronic Total Occlusions, *Cardiac Interventions Today,* June/July 2009.

[28] D. T. Raphael, X. Li, J. Park, R. M. Chen, H. Chabok, A. Barukh, Q. Zhou, M. Elgazery, K. K. Shung, 20 MHz Forward-imaging single-element beam steering with an internal rotating variable-angle reflecting surface: Wire phantom and ex vivo pilot study, *Ultrasonics,* vol. 53, pp. 561-569, Feb 2013.

[29] D. N. Stephens, M. O'Donnell, K. Thomenius, A. Dentinger, D. Wildes, P. Chen, K. K. Shung, J. Cannata, P. Khuri-Yakub, O. Oralkan, A. Mahajan, K. Shivkumar, D. J. Sahn, Experimental studies with a 9F forward-looking intracardiac imaging and ablation catheter, *J Ultrasound Med,* vol. 28, pp. 207-15, Feb 2009.

[30] A. Bezanson, R. Adamson, and J. Brown, Fabrication and performance of a miniaturized 64-element high-frequency endoscopic phased array, *IEEE Trans Ultrason Ferroelectr Freq Control,* vol. 61, pp. 33-43, Jan 2014.

[31] C. Chen, S. B. Raghunathan, Z. Yu, M. Shabanimotlagh, Z. Chen, Z. Y. Chang, S. Blaak, C. Prins, J. Ponte, E. Noothout, H. J. Vos ,J. G. Bosch, M D. Verweij, N. de Jong, M. A. P. Pertijs, A Prototype PZT Matrix Transducer With Low-Power Integrated Receive ASIC for 3-D Transesophageal Echocardiography, *IEEE Trans Ultrason Ferroelectr Freq Control,* vol. 63, pp. 47-59, Jan 2016.

[32] E. D. Light and S. W. Smith, Two dimensional arrays for real time 3D intravascular ultrasound, *Ultrasonic Imaging,* vol. 26, pp. 115-128, Apr 2004.

[33] E. D. Light, J. F. Angle, and S. W. Smith, Real-time 3-D ultrasound guidance of interventional devices, *IEEE transactions on ultrasonics, ferroelectrics, and frequency control,* vol. 55, pp. 2066-2078, 2008.

[34] Y. Wang, D. N. Stephens, and M. O'Donnell, Initial results from a forward-viewing ring-annular ultrasound array for intravascular imaging, *2003 Ieee Ultrasonics Symposium Proceedings, Vols 1 and 2,* pp. 212-215, 2003.

[35] W. C. Black and D. N. Stephens, Cmos Chip for Invasive Ultrasound Imaging, *Ieee Journal of Solid-State Circuits,* vol. 29, pp. 1381-1387, Nov 1994.

[36] B. T. Khuri-Yakub and O. Oralkan, Capacitive micromachined ultrasonic transducers for medical imaging and therapy, *Journal of Micromechanics and Microengineering,* vol. 21, May 2011.

[37] A. F. van der Steen, R. A. Baldewsing, F. Levent Degertekin, S. Emelianov, M. E. Frijlink, Y. Furukawa, D. Goertz, M. Karaman, P. T. Khuri-Yakub, K. Kim, F. Mastik, T. Moriya, Ö. Oralkan, Y. Saijo, J. A. Schaar, P. W Serruys, S. Sethuraman, A. Tanaka, H. J. Vos, R. Witte, M. O'Donnel, IVUS beyond the horizon, *EuroIntervention,* vol. 2, pp. 132-42, May 2006.

[38] F. L. Degertekin, R. O. Guldiken, and M. Karaman, Micromachined capacitive transducer arrays for intravascular ultrasound, *Moems Display and Imaging Systems Iii,* vol. 5721, pp. 104-114, 2005.

[39] F. L. Degertekin, R. O. Guldiken, and M. Karaman, Annular-ring CMUT arrays for forward-looking IVUS: Transducer characterization and imaging, *Ieee Transactions on Ultrasonics Ferroelectrics and Frequency Control,* vol. 53, pp. 474-482, Feb 2006.

[40] C. Tekes, G. Gurun, M. W. Rashid, J. Zahorian, T. B. Xu, J. Hasler,F. L. Degertekin, 3-D Real-Time Volumetric Imaging Using 20 MHz 1.5-mm Diameter Single-Chip CMUT-on-CMOS Array, *2012 Ieee International Ultrasonics Symposium (Ius),* 2012.

[41] D. N. Stephens, U. T. Truong, A. Nikoozadeh, Ö. Oralkan, C. H. Seo, J. Cannata, A. Dentinger, K. Thomenius, A. de la Rama, T. Nguyen, F. Lin, P. Khuri-Yakub, A. Mahajan, K. Shivkumar, M. O'Donnell, D. J. Sahn, First In Vivo Use of a Capacitive Micromachined Ultrasound Transducer Array–Based Imaging and Ablation Catheter, *Journal of Ultrasound in Medicine,* vol. 31, pp. 247-256, 2012.

[42] G. Gurun, C. Tekes, J. Zahorian, T. Xu, S. Satir, M. Karaman, J. Hasler, F. L. Degertekin, Single-chip CMUT-on-CMOS front-end system for real-time volumetric IVUS and ICE imaging, *IEEE Trans Ultrason Ferroelectr Freq Control,* vol. 61, pp. 239-50, Feb 2014.

[43] C. Tekes, T. Xu, T. M. Carpenter, S. Bette, U. Schnakenberg, D. Cowell, S. Freear, O. Kocaturk, R. J. Lederman, F. L. Degertekin, Real-Time Imaging System using a 12-MHz Forward-Looking Catheter with Single Chip CMUT-on-CMOS Array, *2015 Ieee International Ultrasonics Symposium (Ius),* 2015.

[44] M. Pekař, A. F. Kolen, H. Belt, F. van Heesch, N. Mihajlović, I. E. Hoefer, T. Szili-Török, H. J. Vos, J. G. Bosch, G. van Soest, A. F.W. van der Steen, Preclinical Testing of Frequency-Tunable Capacitive Micromachined Ultrasonic Transducer Probe Prototypes, *Ultrasound in Medicine and Biology,* vol. 43, pp. 2079-2085, 2017.

[45] P. D. L. Williams, A review of "Synthetic Aperture Radar—Systems & Signal Processing". J. CURLANDER and R. N. McDONOUGH. (Chichester: John Wiley & Sons Ltd.), *International Journal of Remote Sensing,* vol. 13, pp. 3364-3364, 1992/11/01 1992.

[46] A. Fenster, D. B. Downey, and H. N. Cardinal, Three-dimensional ultrasound imaging, *Phys Med Biol,* vol. 46, pp. R67-99, May 2001.

[47] R. W. Prager, R. N. Rohling, A. H. Gee, and L. Berman, Rapid calibration for 3-D freehand ultrasound, *Ultrasound Med Biol,* vol. 24, pp. 855-69, Jul 1998.

[48] R. G. Duncan, M. E. Froggatt, S. T. Kreger, R. J. Seeley, D. K. Gifford, A. K. Sang, M. S. Wolfe., High-accuracy fiber-optic shape sensing - art. no. 65301S, *Sensor Systems and Networks: Phenomena, Technology, and Applications for NDE and Health Monitoring 2007,* vol. 6530, pp. S5301-S5301, 2007.

[49] M. E. Froggatt, J. W. Klein, D. K. Gifford, and S. T. Kreger, Optical position and/or shape sensing, US 8 773 650, Jul. 8, 2014.

[50] N. de Jong, J. Souquet, G. Faber, and N. Bom, Transducers in medical ultrasound: Part Two. Vibration modes, matching layers and grating lobes, *Ultrasonics,* vol. 23, pp. 176-82, Jul 1985.

[51] A. D. Pierce and R. T. Beyer, *Acoustics: An Introduction to Its Physical Principles and Applications*, 1989 Edition, (1990): 1826-1827.

[52] J. P. Arenas, Numerical computation of the sound radiation from a planar baffled vibrating surface, *Journal of Computational Acoustics,* vol. 16, pp. 321-341, 2008.

[53] M. R. Jennings and R. J. McGough, Using FOCUS to determine the radiation impedance for square transducers, *AIP Conference Proceedings,* vol. 1481, pp. 149-154, 2012.

[54] J. Janjic, M. Shabanimotlagh, M. D. Verweij, G. van Soest, A. F. W. van der Steen, and N. de Jong, "Quantifying the effect of subdicing on element vibration in ultrasound transducers," in *Ultrasonics Symposium (IUS), 2015 IEEE International*, 2015, pp. 1-4.

[55] R. E. McKeighen, Design guidelines for medical ultrasonic arrays, *Ultrasonic Transducer Engineering,* vol. 3341, pp. 2-18, 1998.

[56] W. Qi and W. Cao, Finite element study on 1-D array transducer design, *IEEE Trans Ultrason Ferroelectr Freq Control,* vol. 47, pp. 949-55, 2000.

[57] M. E. Frijlink and L. Spicci, The effect of oblique sub-dicing on acoustic performance, *2012 Ieee International Ultrasonics Symposium (Ius),* pp. 1576-1579, 2012.

[58] W. F. Xia, D. Piras, J. C. G. van Hespen, S. van Veldhoven, C. Prins, T. G. van Leeuwen, W. Steenbergen, S. Manoha, An optimized ultrasound detector for photoacoustic breast tomography, *Medical Physics,* vol. 40, Mar 2013.

[59] T. L. Szabo, *Diagnostic ultrasound imaging: inside out*: Academic Press, 2004.

[60] J. F. Guess, C. G. Oakley, S. J. Douglas, and R. D. Morgan, Cross-talk paths in array transducers, *1995 Ieee Ultrasonics Symposium Proceedings, Vols 1 and 2,* pp. 1279-1282, 1995.

[61] D. T. Blackstock, *Fundamentals of physical acoustics*: John Wiley & Sons, 2000.

[62] K. K. Shung, *Diagnostic Ultrasound: Imaging and blood flow measurements*. 6000 Broken Sound Parkway NW, Suite 300: CRC Press Taylor & Francis Group, 2006.

[63] Y. Zhou, *Principles and Applications of Therapeutic Ultrasound in Healthcare*: CRC Press, 2015.

[64] R. S. C. Cobbold, *Foundations of Biomedical Ultrasound*. New York: Oxford University Press, Inc., 2007.

[65] P. L. van Neer, G. Matte, J. Sijl, J. M. Borsboom, and N. de Jong, Transfer functions of US transducers for harmonic imaging and bubble responses, *Ultrasonics,* vol. 46, pp. 336-40, Nov 2007.

[66] M. D. Verweij, B. E. Treeby, K. W. A. van Dongen, and L. and Demi, Simulation of Ultrasound Fields, in *Comprehensive Biomedical Physics*. vol. 2, B. A., Ed., ed Amsterdam: Elsevier, 2014, pp. 465-500.

[67] "Cardiovascular Diseases (CVDs)," *World Health Organization. World Health Organization, n.d. Web. 28 June 2017.*

[68] R. Ross, Mechanisms of disease - Atherosclerosis - An inflammatory disease, *New England Journal of Medicine,* vol. 340, pp. 115-126, Jan 14 1999.

[69] R. Virmani, F. D. Kolodgie, A. P. Burke, A. Farb, and S. M. Schwartz, Lessons From Sudden Coronary Death, *A Comprehensive Morphological Classification Scheme for Atherosclerotic Lesions,* vol. 20, pp. 1262-1275, 2000.

[70] H. M. Garcia-Garcia, B. D. Gogas, P. W. Serruys, and N. Bruining, IVUS-based imaging modalities for tissue characterization: similarities and differences, *International Journal of Cardiovascular Imaging,* vol. 27, pp. 215-224, Feb 2011.

[71] C. L. de Korte, H. H. Hansen, and A. F. van der Steen, Vascular ultrasound for atherosclerosis imaging, *Interface Focus,* vol. 1, pp. 565-75, Aug 06 2011.

[72] B. K. Courtney, N. R. Munce, K. J. Anderson, A. S. Thind, G. Leung, P. E. Radau, S. Foster I. A. Vitkin, R. S. Schwartz, A. J. Dick, G. A. Wright, B. H. Strauss, Innovations in imaging for chronic total occlusions: a glimpse into the future of angiography's blind-spot, *Eur Heart J,* vol. 29, pp. 583-93, Mar 2008.

[73] R. Chen, N. E. Cabrera-Munoz, K. H. Lam, H. S. Hsu, F. Zheng, Q. Zhou, K. K. Shung, PMN-PT single-crystal high-frequency kerfless phased array, *IEEE Trans Ultrason Ferroelectr Freq Control,* vol. 61, pp. 1033-41, Jun 2014.

[74] O. Oralkan, A. S. Ergun, J. A. Johnson, M. Karaman, U. Demirci, K. Kaviani, T. H. Lee, B. T. Khuri-Yakub, Capacitive micromachined ultrasonic transducers: Next-generation arrays for acoustic imaging?, *Ieee Transactions on Ultrasonics Ferroelectrics and Frequency Control,* vol. 49, pp. 1596-1610, Nov 2002.

[75] A. S. Ergun, G. G. Yaralioglu, and B. T. Khuri-Yakub, Capacitive micromachined ultrasonic transducers: Theory and technology, *Journal of Aerospace Engineering,* vol. 16, pp. 76-84, Apr 2003.

[76] Y. Wang, D. N. Stephens, and M. O'Donnell, Optimizing the beam pattern of a forward-viewing ring-annular ultrasound array for intravascular imaging, *Ieee Transactions on Ultrasonics Ferroelectrics and Frequency Control,* vol. 49, pp. 1652-1664, Dec 2002.

[77] J. Janjic, F. Mastik, M. D. Leistikow, J. G. Bosch, G. Springeling, A. F. W. van der Steen, G. van Soest, Sparse Ultrasound Image Reconstruction from a Shape-Sensing Single-Element Forward-Looking Catheter, *IEEE Transactions on Biomedical Engineering,* vol. PP, pp. 1-1, 2018.

[78] M. Tan, C. Chen, Z. Chen, J. Janjic, V. Daeichin, Z. Chang, E. Noothout, G. van Soest, M. Verweij, N. de Jong and M. Pertijs, A front-end ASIC with high-voltage transmit switching and receive digitization for forward-looking intravascular ultrasound. *Custom Integrated Circuits Conference (CICC)*, 2017 IEEE. IEEE, 2017.

[79] J. A. Jensen, Field: A program for simulating ultrasound systems, in *10th nordicbaltic conference on biomedical imaging, vol. 4, supplement 1, part 1: 351--353*, 1996.

[80] J. A. Jensen and S. I. Nikolov, Fast simulation of ultrasound images, *2000 Ieee Ultrasonics Symposium Proceedings, Vols 1 and 2,* pp. 1721-1724, 2000.

[81] J. A. Jensen and N. B. Svendsen, Calculation of pressure fields from arbitrarily shaped, apodized, and excited ultrasound transducers, *IEEE transactions on ultrasonics, ferroelectrics, and frequency control,* vol. 39, pp. 262-267, 1992.

[82] A. Ramalli, E. Boni, A. S. Savoia, and P. Tortoli, Density-tapered spiral arrays for ultrasound 3-D imaging, *IEEE Trans Ultrason Ferroelectr Freq Control,* vol. 62, pp. 1580-8, Aug 2015.

[83] N. N. Abboud, G. L. Wojcik, D. K. Vaughan, J. Mould, D. J. Powell, and L. Nikodym, Finite Element Modeling for Ultrasonic Transducers (Preprint), Weidlinger Associates, new York, 1998.

[84] K. W. Hollman, K. W. Rigby, and M. O'Donnell, Coherence factor of speckle from a multi-row probe, *1999 Ieee Ultrasonics Symposium Proceedings, Vols 1 and 2,* pp. 1257-1260, 1999.

[85] J. G. Knight and F. L. Degertekin, Fabrication and characterization of cMUTs for forward looking intravascular ultrasound imaging, *2003 Ieee Ultrasonics Symposium Proceedings, Vols 1 and 2,* pp. 1175-1178, 2003.

[86] O. Oralkan, S. T. Hansen, B. Bayram, G. G. Yaralioglu, A. S. Ergun, and B. T. Khuri-Yakub, CMUT ring arrays for forward-looking intravascular imaging, in *IEEE Ultrasonics Symposium, 2004*, 2004, pp. 403-406 Vol.1.

[87] A. Nikoozadeh, I. O. Wygant, D. S. Lin, O. Oralkan, A. S. Ergun, D. N. Stephens, K. E. Thomenius, A. M. Dentinger, D. Wildes, G. Akopyan, K. Shivkumar, A. Mahajan, D. J. Sahn, B. T. Khuri-Yakub, Forward-looking intracardiac ultrasound imaging using a 1-D CMUT array integrated with custom front-end electronics, *IEEE Trans Ultrason Ferroelectr Freq Control,* vol. 55, pp. 2651-60, Dec 2008.

[88] J.-F. Gelly, D. M. Mills, F. Lanteri, C. E. Baumgartner, and S. G. Calisti, Method for optimized dematching layer assembly in an ultrasound transducer, U.S. Patent No 7,621,028, 2009.

[89] G. W. Stone, N. J. Reifart, I. Moussa, A. Hoye, D. A. Cox, A. Colombo, D. S. Baim, P. S. Teirstein, B. H. Strauss, M. Selmon, G. S. Mintz, O. Katoh, K. Mitsudo, T. Suzuki, H. Tamai, E. Grube, L. A. Cannon, D. E. Kandzari, M. Reisman, R. S. Schwartz, S. Bailey, G. Dangas, R. Mehran, A. Abizaid, J. W. Moses, M. B. Leon, P. W. Serruys, Percutaneous recanalization of chronically occluded coronary arteries: a consensus document: part II, *Circulation,* vol. 112, pp. 2530-7, Oct 18 2005.

[90] D. T. Yeh, O. Oralkan, I. O. Wygant, M. O'Donnell, and B. T. Khuri-Yakub, 3-D ultrasound imaging using a forward-looking CMUT ring array for intravascular/intracardiac applications, *IEEE Trans Ultrason Ferroelectr Freq Control,* vol. 53, pp. 1202-11, Jun 2006.

[91] U. Demirci, A. S. Ergun, O. Oralkan, M. Karaman, and B. T. Khuri-Yakub, Forward-viewing CMUT arrays for medical imaging, *IEEE Trans Ultrason Ferroelectr Freq Control,* vol. 51, pp. 887-95, Jul 2004.

[92] P. Breedveld and J. S. Scheltes, Instrument for Fine-Mechanical or Surgical Applications, U.S. Patent No 9,138,133, 2015.

[93] P. Breedveld, J. Sheltes, E. M. Blom, and J. E. Verheij, A new, easily miniaturized steerable endoscope, *IEEE engineering in medicine and biology magazine,* vol. 24, pp. 40-47, 2005.

[94] P. Breedveld. (2011). *MultiFlex – Tentacle from Steel*. Available: https://www.bitegroup.nl/maneuverable-devices/the-multiflex/

[95] E. A. Arkenbout, P. W. J. Henselmans, F. Jelínek, and P. Breedveld, A state of the art review and categorization of multi-branched instruments for NOTES and SILS, *Surgical Endoscopy,* vol. 29, pp. 1281-1296, 2015.

[96] P. L. Anderson, R. A. Lathrop, and R. J. Webster Iii, Robot-like dexterity without computers and motors: a review of hand-held laparoscopic instruments with wrist-like tip articulation, *Expert Review of Medical Devices,* vol. 13, pp. 661-672, 2016/07/02 2016.

[97] V. Vitiello, S.-L. Lee, T. P. Cundy, and G.-Z. Yang, Emerging robotic platforms for minimally invasive surgery, *IEEE reviews in biomedical engineering,* vol. 6, pp. 111-126, 2013.

[98] R. G. Duncan, M. E. Froggatt, S. T. Kreger, R. J. Seeley, D. K. Gifford, A. K. Sang, M. S. Wolfe, High-accuracy fiber-optic shape sensing, in *The 14th International Symposium on: Smart Structures and Materials & Nondestructive Evaluation and Health Monitoring*, 2007, pp. 65301S-65301S-11.

[99] C. Fan, D. Dodou, and P. Breedveld, Review of manual control methods for handheld maneuverable instruments, *Minimally Invasive Therapy & Allied Technologies,* vol. 22, pp. 127-135, 2013.

[100] G. W. Stone, N. J. Reifart, I. Moussa, A. Hoye, D. A. Cox, A. Colombo, D. S. Baim, P. S.Teirstein, B. H. Strauss, M. Selmon, G. S. Mintz, O. Katoh, K. Mitsudo, T. Suzuki, H. Tamai, E. Grube, L. A. Cannon, D. E. Kandzari, M. Reisman, R. S. Schwartz, S. Bailey, G. Dangas, R. Mehran, A. Abizaid, J. W. Moses, M. B. Leon, P. W. Serruys. Percutaneous recanalization of chronically occluded coronary arteries - A consensus document - Part II, *Circulation,* vol. 112, pp. 2530-2537, Oct 18 2005.

[101] M. R. Jongbloed, M. J. Schalij, K. Zeppenfeld, P. V. Oemrawsingh, E. E. van der Wall, and J. J. Bax, Clinical applications of intracardiac echocardiography in interventional procedures, *Heart,* vol. 91, pp. 981-90, Jul 2005.

[102] B. Funaki, Transjugular intrahepatic portosystemic shunt, *Semin Intervent Radiol,* vol. 25, pp. 168-74, Jun 2008.

[103] Y. Goykhman, M. Ben-Haim, G. Rosen, M. Carmiel-Haggai, R. Oren, R. Nakache, O. Szold, J. Klausner, I. Kori, Transjugular intrahepatic portosystemic shunt: current indications, patient selection and results, *Isr Med Assoc J,* vol. 12, pp. 687-91, Nov 2010.

[104] J. Janjic, M. D. Leistikow, A. Sakes, F. Mastik, N. de Jong, J. G. Bosch, A. F. W van der Steen, G. Van Soest, 3D Imaging with a Single-Element Forward-Looking Steerable IVUS Catheter: initial testing, *2016 Ieee International Ultrasonics Symposium (Ius),* 2016.

[105] J. Janjic, F. Mastik, M. Leistikow, J. G. Bosch, A. F. W. van der Steen, G. van Soest, Imaging with a single-element forward-looking steerable IVUS catheter using optical shape sensing (Conference Presentation), Proc. SPIE 10135, Medical Imaging 2017: Image-Guided Procedures, Robotic Interventions, and Modeling, 101350Z (26 April 2017);

[106] J. D. Scargle, Studies in Astronomical Time-Series Analysis .3. Fourier-Transforms, Auto-Correlation Functions, and Cross-Correlation Functions of Unevenly Spaced Data, *Astrophysical Journal,* vol. 343, pp. 874-887, Aug 15 1989.

[107] D. S. Early and D. G. Long, Image reconstruction and enhanced resolution imaging from irregular samples, *Ieee Transactions on Geoscience and Remote Sensing,* vol. 39, pp. 291-302, Feb 2001.

[108] J. G. Bosch, M. van Stralen, M. M. Voormolen, B. J. Krenning, C. T. Lancee, J. H. C. Reiber, A.F.W. van der Steen and N. de Jong, Improved spatiotemporal voxel space interpolation for 3D echocardiography with irregular sampling and multibeat fusion, *2005 IEEE Ultrasonics Symposium, Vols 1-4,* pp. 1232-1235, 2005.

[109] H. Knutsson and C. F. Westin, Normalized and Differential Convolution - Methods for Interpolation and Filtering of Incomplete and Uncertain Data, *1993 Ieee Computer Society Conference on Computer Vision and Pattern Recognition : Proceedings,* pp. 515-523, 1993.

[110] T. Q. Pham and L. J. van Vliet, Normalized averaging using adaptive applicability functions with applications in image reconstruction from sparsely and randomly sampled data, *Image Analysis, Proceedings,* vol. 2749, pp. 485-492, 2003.

[111] V. Argyriou, T. Vlachos, and R. Piroddi, Gradient-Adaptive Normalized Convolution, *IEEE Signal Processing Letters,* vol. 15, pp. 489-492, 2008.

[112] M. Sezgin and B. Sankur, Survey over image thresholding techniques and quantitative performance evaluation, *Journal of Electronic Imaging,* vol. 13, pp. 146-168, Jan 2004.

[113] J. W. Goodman, Some Fundamental Properties of Speckle, *Journal of the Optical Society of America,* vol. 66, pp. 1145-1150, 1976.

[114] K. Exner, Ueber das Funkeln der Sterne und die Scintillation überhaupt, *Annalen der Physik,* vol. 253, pp. 305-322, 1882.

[115] J. W. Goodman, Statistical properties of laser speckle patterns, in *Laser speckle and related phenomena*, ed: Springer, 1975, pp. 9-75.

[116] L. Mandel and E. Wolf, *Optical Coherence and Quantum Optics*. Cambridge: Cambridge University Press, 1995.

[117] C. B. Burckhardt, Speckle in Ultrasound B-Mode Scans, *Ieee Transactions on Sonics and Ultrasonics,* vol. 25, pp. 1-6, 1978.

[118] J. W. Goodman, *Speckle phenomena in optics: theory and applications*: Roberts and Company Publishers, 2006.

[119] D. Huang, E. A. Swanson, C. P. Lin, J. S. Schuman, W. G. Stinson, W. Chang, M. R. Hee, T. Flotte, K. Gregory, C. A. Puliafito, and J. G. Fujimoto, Optical coherence tomography, *Science,* vol. 254, pp. 1178-81, Nov 22 1991.

[120] J. M. Schmitt, S. H. Xiang, and K. M. Yung, Speckle in optical coherence tomography, *J Biomed Opt,* vol. 4, pp. 95-105, Jan 1999.

[121] B. Karamata, K. Hassler, M. Laubscher, and T. Lasser, Speckle statistics in optical coherence tomography, *J Opt Soc Am A Opt Image Sci Vis,* vol. 22, pp. 593-596, Apr 2005.

[122] A. Curatolo, B. F. Kennedy, D. D. Sampson, and T. R. Hillman, *Speckle in optical coherence tomography*: Taylor & Francis, 2013.

[123] R. F. Wagner, S. W. Smith, J. M. Sandrik, and H. Lopez, Statistics of Speckle in Ultrasound B-Scans, *Ieee Transactions on Sonics and Ultrasonics,* vol. 30, pp. 156-163, 1983.

[124] F. L. Lizzi, S. K. Alam, S. Mikaelian, P. Lee, and E. J. Feleppa, On the statistics of ultrasonic spectral parameters, *Ultrasound Med Biol,* vol. 32, pp. 1671-85, Nov 2006.

[125] J. W. Goodman, *Statistical Optics*: Wiley, 1985.

[126] T. Hellmuth, Contrast and resolution in optical coherence tomography, *Optical Biopsies and Microscopic Techniques, Proceedings Of,* vol. 2926, pp. 228-237, 1996.

[127] F. L. Lizzi, M. Greenebaum, E. J. Feleppa, M. Elbaum, and D. J. Coleman, Theoretical Framework for Spectrum Analysis in Ultrasonic Tissue Characterization, *Journal of the Acoustical Society of America,* vol. 73, pp. 1366-1373, 1983.

[128] R. F. Wagner, M. F. Insana, and S. W. Smith, Fundamental Correlation Lengths of Coherent Speckle in Medical Ultrasonic Images, *Ieee Transactions on Ultrasonics Ferroelectrics and Frequency Control,* vol. 35, pp. 34-44, Jan 1988.

[129] P. M. Shankar, A Model for Ultrasonic Scattering from Tissues Based on the K-Distribution, *Physics in Medicine and Biology,* vol. 40, pp. 1633-1649, Oct 1995.

[130] D. Kaplan and Q. G. Ma, On the Statistical Characteristics of Log-Compressed Rayleigh Signals - Theoretical Formulation and Experimental Results, *Ieee 1993 Ultrasonics Symposium Proceedings, Vols 1 and 2,* pp. 961-964, 1993.

[131] J. M. Thijssen, B. J. Oosterveld, and R. F. Wagner, Gray Level Transforms and Lesion Detectability in Echographic Images, *Ultrasonic Imaging,* vol. 10, pp. 171-195, Jul 1988.

[132] M. Y. Mehr, A. Bahrami, H. Fischer, S. Gielen, R. Corbeij, W. D. v. Driel, G.Q. Zhang, An overview of scanning acoustic microscope, a reliable method for non-destructive failure analysis of microelectronic components, in *2015 16th International Conference on Thermal, Mechanical and Multi-Physics Simulation and Experiments in Microelectronics and Microsystems*, 2015, pp. 1-4.

[133] A. F. W. Van Der Steen, C. L. De Korte, and J. M. Thijssen, Ultrasonic spectroscopy of the porcine eye lens, *Ultrasound in Medicine & Biology,* vol. 20, pp. 967-974, 1994/01/01/ 1994.

[134] C. L. De Korte, A. F. W. van der Steen, and J. M. Thijssen, Acoustic velocity and attenuation of eye tissues at 20 MHz, *Ultrasound in Medicine & Biology,* vol. 20, pp. 471-480, 1994/01/01/ 1994.

[135] F. S. Foster, C. J. Pavlin, K. A. Harasiewicz, D. A. Christopher, and D. H. Turnbull, Advances in ultrasound biomicroscopy, *Ultrasound in Medicine & Biology,* vol. 26, pp. 1-27, 2000/01/01/ 2000.

[136] K. Kumagai, H. Koike, R. Nagaoka, S. Sakai, K. Kobayashi, and Y. Saijo, High-Resolution Ultrasound Imaging of Human Skin in Vivo by Using Three-Dimensional Ultrasound Microscopy, *Ultrasound in Medicine and Biology,* vol. 38, pp. 1833-1838, Oct 2012.

[137] C. Chandrana, J. Talman, T. Pan, S. Roy, and A. Fleischman, Design and analysis of MEMS based PVDF ultrasonic transducers for vascular imaging, *Sensors (Basel),* vol. 10, pp. 8740-50, 2010.

[138] F. Guo, C. Liu, Y. Yang, L. Sun, B. Yang, Y. Chen, J. Dai, Devolopment of focused IVUS transducer using PMN-PT single crystal in *Ultrasonics Symposium (IUS), 2014 IEEE International*, 2014, pp. 97-100.

[139] P. D. Corl, Focused rotational ivus transducer using single crystal composite material, U.S. Patent Application No 14/137,465, 2014.

[140] R. A. Lemons and C. F. Quate, Acoustic Microscopy: Biomedical Applications, *Science,* vol. 188, pp. 905-911, 1975.

[141] T. Turpin, L. Gesell, J. Lapides, and C. Price, Theory of the synthetic aperture microscope, *Advanced Imaging Technologies and Commercial Applications,* vol. 2566, pp. 230-240, 1995.

[142] G. Zheng, R. Horstmeyer, and C. Yang, Wide-field, high-resolution Fourier ptychographic microscopy, *Nat Photonics,* vol. 7, pp. 739-745, Sep 1 2013.

[143] X. Ou, R. Horstmeyer, C. Yang, and G. Zheng, Quantitative phase imaging via Fourier ptychographic microscopy, *Opt Lett,* vol. 38, pp. 4845-8, Nov 15 2013.

[144] J. K. Adams, V. Boominathan, B. W. Avants, D. G. Vercosa, F. Ye, R. G. Baraniuk, J. T. Robinson, and A. Veeraraghavan, Single-frame 3D fluorescence microscopy with ultraminiature lensless FlatScope, *Sci Adv,* vol. 3, p. e1701548, Dec 2017.

[145] N. Antipa, G. Kuo, R. Heckel, B. Mildenhall, E. Bostan, R. Ng, L. Waller, DiffuserCam: lensless single-exposure 3D imaging, *Optica,* vol. 5, pp. 1-9, 2018/01/20 2018.

[146] S. A. Alexandrov, T. R. Hillman, T. Gutzler, and D. D. Sampson, Synthetic aperture fourier holographic optical microscopy, *Physical Review Letters,* vol. 97, Oct 20 2006.

[147] C. J. Schwarz, Y. Kuznetsova, and S. R. J. Brueck, Imaging interferometric microscopy, *Optics Letters,* vol. 28, pp. 1424-1426, 2003/08/15 2003.

[148] T. S. Ralston, D. L. Marks, P. S. Carney, and S. A. Boppart, Interferometric synthetic aperture microscopy, *Nat Phys,* vol. 3, pp. 129-134, Feb 1 2007.

[149] K. Tomiyasu, Tutorial Review of Synthetic-Aperture Radar (Sar) with Applications to Imaging of Ocean Surface, *Proceedings of the Ieee,* vol. 66, pp. 563-583, 1978.

[150] K. Melde, A. G. Mark, T. Qiu, and P. Fischer, Holograms for acoustics, *Nature,* vol. 537, pp. 518-22, Sep 22 2016.

[151] M. D. Brown, D. I. Nikitichev, B. E. Treeby, and B. T. Cox, Generating arbitrary ultrasound fields with tailored optoacoustic surface profiles, *Applied Physics Letters,* vol. 110, Feb 27 2017.

[152] P. Kruizinga, P. van der Meulen, A. Fedjajevs, F. Mastik, G. Springeling, N. de Jong, G. Leus, Compressive 3D ultrasound imaging using a single sensor, *Sci Adv,* vol. 3, p. e1701423, Dec 2017.

[153] I. M. Vellekoop and A. P. Mosk, Focusing coherent light through opaque strongly scattering media, *Optics Letters,* vol. 32, pp. 2309-2311, Aug 15 2007.

[154] NDT Resource Center. Available: https://www.nde-ed.org/GeneralResources/MaterialProperties/UT/ut_matlprop_plastics.htm

[155] P. R. Stepanishen and K. C. Benjamin, Forward and Backward Projection of Acoustic Fields Using Fft Methods, *Journal of the Acoustical Society of America,* vol. 71, pp. 803-812, 1982.

[156] P. Van der Meulen, P. Kruizinga, J. G. Bosch, and G. Leus, Spatial Compression in Ultrasound Imaging, in *Signals, Systems and Computers, Fifty-First Asilomar Conference on. IEEE*, 2017.

[157] G. S. Mintz and G. Guagliumi, Intravascular imaging in coronary artery disease, *Lancet,* vol. 390, pp. 793-809, Aug 19 2017.

[158] G. Gurun, P. Hasler, and F. L. Degertekin, Frontend Receiver Electronics for High Frequency Monolithic CMUT-on-CMOS Imaging Arrays, *Ieee Transactions on Ultrasonics, Ferroelectrics, and Frequency Control,* vol. 58, pp. 1658-1668, 2011.

[159] Y. Hirano, N. Ishikawa, and G. Watanabe, Suture damage after grasping with EndoWrist of the da Vinci Surgical System, *Minim Invasive Ther Allied Technol,* vol. 19, pp. 203-6, Aug 2010.

[160] J. Catherine, C. Rotinat-Libersa, and A. Micaelli, Comparative review of endoscopic devices articulations technologies developed for minimally invasive medical procedures, *Applied Bionics and Biomechanics*, vol. 8, pp. 151-171, 2011.

Summary

Minimally invasive procedures are increasingly replacing traditional open surgeries due to their shorter recovery time, reduced patient pain, reduced risk of infection and less trauma. However, since the physician has no direct view of the working field, visualization of these complex interventions is critical for success. Forward-looking (FL) ultrasound image guidance can aid minimally invasive procedures providing visual feedback of the working field, instrument location and treatment progress. Currently there are no clinically available devices that can provide minimally invasive 3D FL imaging.

In this thesis we explored several innovative solutions towards miniaturized 3D FL imaging. We looked into methods to solve both hardware and image-related challenges resulting in mainly two approaches. The first approach consists in the realization of a complex multi-element transducer with an optimized design and an efficient interconnection and integration scheme. The second approach consists in the use of simple single-element transducers combined with steering catheters, optical shape sensing systems (OSS) and coding masks to achieve 3D FL imaging.
After introducing the importance of FL image guidance for minimally invasive procedures in **Chapter 1**, in **Chapter 2** we focused on the effects of element geometry on the vibration mode and radiation impedance of a 1D transducer array. We demonstrated, through finite element simulations, that subdicing elements having a width greater than 0.6 times the wavelength improves the acoustic performance. This is an important result for high frequency transducers (>10 MHz) since for those transducers small width-to-thickness ratios are difficult to achieve and non-piston like modes are more likely to occur. In the same chapter we also demonstrated that subdicing only 70% of the total element thickness is already enough to achieve optimal acoustic behavior.

In **Chapter 3** we described a 2D matrix transducer with an aperture size of 1.5 mm consisting of 80 elements interfaced with a front-end ASIC that requires only 4 micro-coaxial cables, making possible integration in intravascular catheters. We investigated optimal transducer design in simulations, we evaluated the effects of a practical implementation and we fabricated and tested the final design. Acoustical characterization and initial imaging results demonstrated the potential of the proposed device to achieve 3D FL imaging.

In the effort of reducing the hardware complexity of the ultrasound device, we moved towards investigation on how to perform 3D FL imaging using a single-element transducer. Since a single-element transducer provides only a single A-line, additional source of information is required to achieve volumetric imaging. We propose to combine the single-element transducer with an OSS system in a steerable device. The idea is to acquire multiple A-lines while steering

the device and to find an appropriate algorithm to combine them using the position information from OSS.

In **Chapter 4** we described a novel device with a steerable tip having 8 degrees of freedom. A prototype was manufactured with a single-element ultrasound transducer and an OSS fiber integrated at the tip. We demonstrated the feasibility of combining ultrasound A-lines and OSS position information while manually steering the device to reconstruct in 3D targets located ahead of the device tip.

Since steering of minimally devices is performed manually by the physician during the procedure and it is limited to specific patterns depending on the catheter design, sparse and irregularly sampled ultrasound data are acquired. To interpolate these sparse data we introduced in **Chapter 5** adaptive normalized convolution. We tested the method using a clinically available steerable catheter that was modified to accommodate a single element transducer and the OSS fiber. We successfully reconstructed the image of the surface of a phantom and an *ex-vivo* human carotid plaque. We extend the same method to 3D to reconstruct volumetric images of structures within an *ex-vivo* pig heart using a novel multi-steerable catheter designed for cardiac applications (**Chapter 6**).

In the effort of further improving the image resolution, we investigated and exploited the spatial information within a structured ultrasound beam. Speckle is a well-known phenomenon resulting from distorting an incident coherent wave until all spatial coherence is lost. The basic physics of this phenomenon was reviewed in **Chapter 7**. In this chapter we introduced the concept of speckle and showed that the magnitude of a random phasor sum can be statistically described with a Rayleigh distribution. We also statistically described the scattered field with a constant background and non-uniform phase distribution. In addition, we described the second-order statistics, that relates the speckle size to the resolution cell dimension, and the effect of dynamic range compression on speckle statistics.

In **Chapter 8** we explored the concept of structured ultrasound microscopy, where 3D forward-looking imaging is achieved by solving an inverse scattering problem. To make the scattering problem better posed, we placed a coding mask in front of a single-element transducer, hence destroying the phase uniformity within the beam and resulting in a unique signal for each imaging voxel. We synthetically enlarged the imaging aperture by translating the transducer across the 3D volume allowing for wide-field 3D imaging at isotropic microscopic resolution using a very small unfocused ultrasound sensor and sparse spatial sampling.

In **Chapter 9** we summarized the achieved results and we discussed limitations and future work needed to successfully implement minimally invasive FL imaging in clinical practice.

Samenvatting

Minimaal invasieve interventies vervangen steeds meer de traditionele chirurgisch ingrepen door de vele voordelen die hieraan verbonden zijn, zoals kortere hersteltijd, minder pijn voor de patiënt, een verminderde kans op infecties en minder schade. Het nadeel van zo'n procedure is echter dat de chirurg slechter zicht heeft tijdens de operatie. Een oplossing hiervoor zou een voorwaarts kijkende ultrageluid transducent kunnen zijn. Zo'n transducent kan tijdens een minimaal invasieve interventie visuele feedback geven over het weefsel, informatie geven over positionering van de instrumentatie, en de vorderingen tijdens de procedure. Op dit moment is er geen hulpmiddel beschikbaar in de kliniek wat in 3D en voorwaartse (3D FL) beeldvorming kan verzorgen tijdens minimaal invasieve procedures.

In dit proefschrift verkennen we meerdere innovatieve oplossing die kunnen leiden naar een 3D FL katheter. We hebben gekeken naar methoden om problemen omtrent de hardware en de beeldvorming op te lossen, wat heeft geresulteerd in twee benaderingen. De eerste benadering is gericht op het maken van een complexe multi-element transducent, waarbij we het ontwerp hebben geoptimaliseerd, efficiënte schakeling hebben ontworpen en het geheel hebben geïntegreerd. De tweede benadering is een katheter bestaande uit een bestuurbare transducent bestaande uit maar een element, gecombineerd met optische vorm waarneming (OSS) en een coderen masker over het element voor een 3D beeld.

In **hoofdstuk 1** wordt het belang van een 3D FL beeldvorming voor minimaal invasieve procedures verder toegelicht. Waarna in **hoofdstuk 2** het effect van de geometrie van een 1D multi-element transducent ontwerp werd getoetst aan de hand van de vibratiemodus en de stralingsimpedantie. Doormiddel van een eindige-elementenmethode laten we zien dat het opdelen van de transducent in elementen die groter zijn dan 0.6 keer de golflengte van het ultrageluid de akoestische prestaties verbetert. Dit is gunstig voor transducenten voor hoog frequent ultrageluid (>10MHz) omdat voor dit type transducenten geldt dat het lastig is om een kleine verhouding tussen de breedte en de dikte van de elementen te krijgen, wat en voor kan zorgen dat er meer vibraties ontstaan dan alleen een enkele vibratie over de dikte van het elementen. Daarnaast laten we ook zien dat het opdelen van de elementen maar over 70% van de dikte van het element hoeft te gebeuren om goede akoestische eigenschappen te krijgen.

In **hoofdstuk 3** beschrijven we een 2D matrix transducent met een apertuur grootte van 1.5mm bestaande uit 80 elementen verbonden met een toepassing specifieke geïntegreerde schakeling(ASIC). Deze ASIC heeft maar 4 micro coaxiale kabels nodig waardoor dit ontwerp kan worden geïntegreerd in een intravasculaire katheter. We onderzoeken het optimale ontwerp van een dergelijke transducent met behulp van simulaties. Hierbij hebben we gekeken naar de praktische implementatie en hebben we het uiteindelijke ontwerp geproduceerd en getest.

De akoestische eigenschappen en de eerste beelden laten zien dat dit ontwerp mogelijk kan worden toegepast voor 3D FL beeldvorming.

In een poging om het ontwerp vanuit een hardware oogpunt simpeler te maken hebben we gekeken naar de mogelijkheid om 3D FL beeldvorming te doen met een transducent met een enkel element. Een enkel element geeft maar een A-lijn, waardoor een andere bron van informatie nodig is om een volume in beeld te kunnen brengen. Daarom hebben we een transducent met een element gecombineerd met een OSS systeem en de katheter stuurbaar gemaakt. Het idee hierachter is dan we meerdere A-lijnen kunnen meten terwijl de katheter wordt gestuurd en zo met behulp van de informatie van de OSS een beeld kunnen reconstrueren.

In **hoofdstuk 4** laten we een ontwerp zien van een systeem met een stuurbare kop met 8 vrijheidsgraden. Een prototype van de systeem is ontwikkeld met daarbij een enkel element transducent en het OSS systeem in de kop geïntegreerd. We laten zien dat het mogelijk is om hiermee op de hierboven beschreven manier een 3D beeld te kunnen reconstrueren. Tijdens die experimenten werd de transducent kop met de hand gestuurd.

Het met de hand sturen van de transducent en de gelimiteerde bewegingsvrijheid van het ontwerp zorgen ervoor dat de data dun en onregelmatig verdeeld is over het volume. Om deze data te kunnen interpoleren introduceren we in **hoofdstuk 5** adaptieve genormaliseerde convolutie. We hebben dit getest met behulp van een klinische beschikbare stuurbare katheter die we hebben aangepast zodat het mogelijk was om de transducent en de OSS fiber te integreren. Hiermee hebben we laten zien dat het mogelijk is om succesvol het oppervlak van een humane carotide plaque in beeld te brengen. We hebben deze methode uitgebreid naar 3D en daarmee structuren in een ex-vivo varkenshart in beeld gebracht, **hoofdstuk 6**.

In een poging om de beeldresolutie te verbeteren hebben we gekeken naar de mogelijkheid om de spatiele informatie van een gestructureerde ultrageluid bundel te gebruiken. Speckle is een bekend fenomeen wat voortkomt uit vervormingen in een coherente golf totdat alle spatiele cohesie verdwenen is. De fysica hiervan is uiteengezet in **hoofdstuk 7**. In dit hoofdstuk introduceren we het concept en laten we zien dat de grootte van de som van een willekeurig fasor statistisch kan worden beschreven met een Rayleigh verdeling. Ook beschrijven we statistisch het verstrooide veld met een constante achtergrond en een niet uniforme fase verdeling. Daarnaast vervaardigen we ook de tweede orde statisiek, welke de speckle grootte relateert aan de pixel grootte. en het effect van het dynamische bereik compressie op de speckle statistiek.

In **hoofdstuk 8** onderzoeken we de mogelijkheid om gebruik te maken van een gestructureerd geluidsveld, waarbij we 3D beeldvorming bewerkstelligen door de inverse van een verstrooiings-probleem oplossen. We noemen dit concept gestructureerde geluidsveld microscopie. We versimpelen het verstrooiingsprobleem door gebruik te maken van een masker wat op een

transducent met een enkel element wordt geplaatst. Door dit masker krijgt het geluidsveld een uniek signaal in elke voxel. Daarnaast verplaatsen we de transducent over een dun verdeeld en niet uniform raster waardoor de hoek van de beeldvorming wordt vergroot. De combinatie van het bewegen en het masker zorgen ervoor dat we een 3D beeld kunnen krijgen met een isotrope en microscopische resolutie terwijl we verder alleen maar gebruik te maken van een piepkleine onfocuste sensor en weinig datapunten.

In **hoofdstuk 9** worden alle resultaten samengevat en bespreken we de beperking en grenzen van het onderzoek. We sluiten af met de stappen die nodig zijn om dit onderzoek verder te brengen naar een succesvolle implementatie in minimaal invasie voorwaarts kijkende katheter voor klinische toepassingen.

Publications

Peer-reviewed Papers

Jovana Janjic, Maysam Shabanimotlagh, Gijs van Soest, Antonius F.W. van der Steen, Nico de Jong, Martin D. Verweij, "Improving the Performance of a 1-D Ultrasound Transducer Array by Subdicing", *IEEE Trans Ultrason Ferroelectr Freq Control. 2016 Aug; 63(8):1161-71*.

Jovana Janjic, Frits Mastik, Merel D. Leistikow, Johan G. Bosch, Geert Springeling, Antonius F. W. van der Steen, Gijs van Soest, "Sparse Ultrasound Image Reconstruction from a Shape-Sensing Single-Element Forward-Looking Catheter", *IEEE Trans. On Biomedical Engineering* (*accepted*).

Aimee Sakes, Awaz Ali**, Jovana Janjic**, Paul Breedveld, "Novel Miniature Tip Design for Enhancing Dexterity in Minimally Invasive Surgery", *Journal of Medical Devices* (*accepted*).

Mingliang Tan, Chao Chen, Zhao Chen, **Jovana Janjic**, Verya Daeichin, Zu-yao Chang, Emile Noothout, Gijs van Soest, Martin D. Verweij, Nico de Jong, and Michiel A. P. Pertijs, "A Front-End ASIC with High-Voltage Transmit Switching and Receive Digitization for 3D Forward-Looking Intravascular Ultrasound Imaging" (*IEEE Journal of Solid State Circuits, accepted*).

Jovana Janjic, Pieter Kruizinga, Pim van der Meulen, Geert Springeling, Frits Mastik, Geert Leus, Johan G. Bosch, Antonius F. W. van der Steen, Gijs van Soest, "Structured Ultrasound Microscopy" (*submitted to Applied Physics Letters*).

Papers in Preparation

Jovana Janjic, Mingliang Tan, Emile Noothout, Chao Chen, Zhao Chen, Zu-yao Chang, Robert H.S.H. Beurskens, Gijs van Soest, Antonius F. W. van der Steen, Martin Verweij, Michiel A. P. Pertijs, Nico de Jong, "A 2D Ultrasound Transducer with Front-End ASIC and Low Cable Count for 3D Forward-Looking Intravascular Imaging: Performance and Characterization".

Maysam Shabanimotlagh, Shreyas B. Raghunathan, **Jovana Janjic**, Verya Daeichin, Emile Noothout, Michiel A.P. Pertijs, Johan G. Bosch, Nico de Jong, Martin D. Verweij, "Effect of Subdicing on Performance of an Ultrasound Matrix Transducer for Carotid Imaging: Numerical and Experimental Study".

Douwe van Willigen, Michiel Pertijs, **Jovana Janjic**, Eunchul Kang, Mingliang Tan, Zu-Yao Chang, Emile Noothout, Martin Verweij and Nico de Jong, "A Transceiver ASIC for a Single-Cable 64-Element Intra-Vascular Ultrasound Probe".

Conference Proceedings

Jovana Janjic, Maysam Shabanimotlagh, Martin D. Verweij, Gijs van Soest, Antonius F.W. van der Steen, Nico de Jong, "Quantifying the effect of subdicing on element vibration in ultrasound transducers", *Proc. IEEE International Ultrasonics Symposium (IUS), Oct. 2015, pp 1-4*.

Jovana Janjic, Merel D. Leistikow, Aimee Sakes, Frits Mastik, Nico de Jong, Johan G. Bosch, Antonius F.W. van der Steen, Gijs van Soest, "3D Imaging with a single-element forward-looking steerable IVUS catheter: initial testing," *2016 IEEE International Ultrasonics Symposium (IUS)*, Tours, 2016, pp. 1-4.

Maysam Shabanimotlagh, **Jovana Janjic**, Shreyas Raghunathan, Michiel Pertijs, Nico de Jong and Martin Verweij, "The role of sub-dicing in the acoustical design of an ultrasound matrix transducer for carotid arteries imaging," *2016 IEEE International Ultrasonics Symposium (IUS)*, Tours, 2016, pp. 1-4.

Mingliang Tan, Chao Chen, Zhao Chen, **Jovana Janjic**, Verya Daeichin, Zu-yao Chang, Emile Noothout, Gijs van Soest, Martin Verweij, Nico de Jong and Michiel Pertijs "A front-end ASIC with high-voltage transmit switching and receive digitization for forward-looking intravascular ultrasound," *2017 IEEE Custom Integrated Circuits Conference (CICC)*, Austin, TX, 2017, pp. 1-4.

Book Chapter

Jovana Janjic and Gijs van Soest, Speckle Physics, in *Handbook of Speckle Filtering and Tracking in Cardiovascular Ultrasound Imaging and Video*, Loizou, Christos P.; Pattichis, Constantinos S; D'hooge, Jan, The Institution of Engineering and Technology, London (UK), 2018, pp. 25-54.

Curriculum vitae

Jovana Janjic was born in Banja Luka (Bosnia and Herzegovina) on April 1989.

With the start of the war in former Yugoslavia she and her family moved first to Belgrade and one year later to Italy, in Caorle, a small coastal town north of Venice.

She received the B.Sc. in Information Engineering in 2011 and the M.Sc. in Bioengineering in 2013 from The University of Padova, Italy. She was selected within the Erasmus Programme as an exchange student at the Royal Institute of Technology (KTH), Stockholm, Sweden, from August 2012 until June 2013. At KTH she completed her Master thesis on sonothrombolysis using contrast agents. In 2013 she joined the department of Biomedical Engineering at Erasmus University Medical Center, where she conducted the research that led to this PhD thesis.

PhD Portfolio

Jovana Janjic

Courses	year	ECTS
IVUS, Virtual Histology & FFR, Theory & Practice	2013	0.6
Pathophysiology of Ischemic Heart Disease	2014	1.5
Micromachined Ultrasonics Transducers, Danish Technical University, Copenhagen, Denmark	2014	3.5
Verasonics course, Taipei, Taiwan	2015	0.2
Cardiovascular Imaging and Diagnostic	2015	1.5
English biomedical writing and communication	2015	4
Signal Processing and System-on-Chip Designs for Ultrasonic Imaging, Detection and Estimation Application, IEEE Taipei, Taiwan	2015	0.2
Advanced Ultrasound Imaging, Danish Technical University, Copenhagen, Denmark	2015	2.5
Microultrasound Transducers – Materials, Instrumentation and Performance, IEEE, Tours, France	2016	0.2
Elasticity Imaging: Methods and Applications, IEEE, Washington D.C., USA	2017	0.2
High-Performance Computing for Medical Imaging on Programmable Graphics Hardware (GPU)	2017	0.2
Workshops and Seminars		
Seminar: New imaging strategies for the detection of atherosclerosis	2014	0.2
Seminar: Current cardiac and vascular aging research at EMC	2014	0.2
NVMU Autumn meeting, Maastricht	2013	0.15
NVMU Spring meeting, Enschede	2014	0.15
NVMU Autumn meeting, Delft	2014	0.15
NVMU Autmn meeting, Eindhoven, (Oral)	2015	0.2
Workshop: Photoshop and Illustrator CS5	2015	0.3
iMIT meeting, Delft (Oral)	2013	0.6
iMIT meeting, Eindhoven (Oral)	2014	0.6
iMIT meeting, Rotterdam (Oral)	2017	0.6
COEUR PhD-day 2014	2014	0.6
COEUR PhD-day 2015	2015	0.6

International conferences

IEEE International Ultrasonic Symposium, Taipei, Taiwan (Poster)	2015	1.8
SPIE Medical Imaging, Orland, Florida, USA (Oral)	2017	2.1
IEEE International Ultrasonic Symposium, Washington D.C., USA (Oral)	2017	2.1
International Conference on Ultrasonic Biomedical Microscanning, Kralendijk, Bonaire, The Netherlands (Oral)	2016	2.1
International Conference on Ultrasonic Biomedical Microscanning, Edinburgh, Scotland, UK (Oral)	2014	2.1
Artimino Conference, Helsinborg, Sweden (Oral)	2015	2.1
Design of Medical Devices, Delft, The Netherlands (Poster)	2014	1.2
Design of Medical Devices, Delft, The Netherlands (Oral)	2016	1.5
Design of Medical Devices, Delft, The Netherlands (Oral)	2017	1.5
Optics in Cardiology (Poster)	2017	0.9
Optics in Cardiology	2015	0.6
Ultrasound Contrast Imaging Symposium, Rotterdam, The Netherlands	2014-2018	2.7
	TOT	**39.65**

Acknowledgment

First of all, I would like to express my deep gratitude to Ton and Nico, my promotors. Ton, thank you for giving me a PhD position in the BME group. It has been fantastic to work in such an inspiring environment with so much knowledge and great colleagues. Thank you for always making time to discuss problems and issues and thank you for supporting me throughout all these years. Nico, I am honored to have you as my promotor. I have been always impressed by your passion for ultrasound transducers and I have enjoyed discussing with you different designs and technical solutions.

I would also like to thank Gijs, my co-promotor, for all the supervision throughout these years and the help in improving my "wordy" writing skills. I admire your sharp eye for details and your broad knowledge on different subjects. I can always come to you with a problem and you will be proposing solutions and improvements way ahead from where I left it.

I want to thank Hans for the nice discussions on normalized convolution, Kalman filtering and compressive sensing and for the supervision during the months that Gijs was in Australia. I am impressed on how many projects you are involve with and the passion you devote to all of them.

Writing the result section of any paper would have been impossible without Frits, Robert and Geert. Frits, thank you for all the times you helped me with the programming and the image processing until late in the evening. It is so great and unique to have the possibility to discuss about IVUS imaging with an expert that has worked with this technology from its early developments. I also want to thank you for the great technical and human support during the experiments at Philips: your help has been fundamental for me. And sorry for making you run to catch the bus while carrying the pulser.
Robert(o), you are not only an electronic engineer with amazing debugging skills, you are also the most patient listener of PhD's problems and most of all, you have the best supply of cookies and chocolate of the department. Thank you for teaching me a bit of soldering, for transporting my equipment to Philips and for helping with the job search of Enrico.
Thank you to Geert and to all the technicians from the workshop for all the help with every set-up and transducer integration. You are always available to discuss crazy ideas and with your expertise and skilled hands every wish comes true.
Gerard, software installations and back-ups have never been a problem with you around and I really enjoyed listening to your curious stories about your diving adventures.

Within the time frame of this PhD I also had the chance to collaborate with different departments and groups and I have learned a lot from all of them.

I want to thank the group from the Laboratory of Acoustical Wavefield Imaging in Delft for all the valuable input and great help. Martin Verweij, the paper presented in Chapter 2 of this thesis would have not been accepted in such a short time (only two weeks!!) without your analytical and critical comments and your deep understanding of theoretical modeling and numerical simulation of ultrasound transducers. Maysam, I really enjoyed our endless discussions about PZFlex simulations and transducer measurements. Emile, thank you for all the effort in building the transducers. I know that cleaning those bond pads has been a nightmare, but you did an amazing job in that tiny space. Verya, I enjoyed listening to your "home-made" music when you were in our group and I admire your constant calm attitude in the lab.
I owe thanks to the Electronic Instrumentation Laboratory in Delft for the great team effort in developing all the integrated circuitry for the 2D matrix transducers. Michiel Pertijs, thank to you and to your great group for always being available to discuss and to explain patiently (over and over again) the ASIC components and functionalities. Mingliang, Douwe, Chao and Zu-yao, it has been really fun running experiments in your lab even if we had to work until late in the evening to meet the deadlines.
A great thank goes to the Philips Research group in Eindhoven and particularly to René Aarnink, Michel van Bruggen and Merel Leistikow for providing me with all the support during my experiments with the optical shape sensing system.
I also would like to thank the BioMechanical Engineering Department of Delft and in particular Paul Breedveld, Aimee, Awaz and Remi. It has been really nice collaborating with you on the integration of our ultrasound transducers in your multisteerable catheters.
I want to thank Jenny Donkelman for managing the iMIT collaboration. I really enjoyed the meetings and the interaction with the other iMIT projects.

Special thanks go to my office mates for all the great time we had together. Muthu thank you for the help with the Belastingdienst in my first years. Tianshi, I really enjoyed the spicy dinners with you and your wife. Min, thank you for helping me in the lab with my very first experiments and thank you for taking care of me in Taiwan: with you by my side all the doctors and nurses left their patients to assist me. Martin, thank you for the nice and fun moments during conferences and summer schools all around the world. Sophi, you are such a kind-hearted person and I have been very lucky having you as my desk-mate. But to me you are more than that: you are a good friend, always there to comfort me in the difficult moments and always bearing my moodiness. Mirjam, you are a very strong girl that knows what she wants and I have really enjoyed having you as a colleague. Reza, thank you for the nice chats in the "cave" and the ginger remedy for the cold. Leo, è bello sapere che un po' di spirito italiano continuerà ad esserci nel lab; in bocca al lupo per il tuo dottorato!
Thank you to Pieter and Pim, the computational imaging guys that have been fundamental in achieving the results presented in Chapter 8. Pieter, my dear non-friend-only-colleague Pietro, I forgive you for misspelling my name in the acknowledgment of your PhD thesis and I thank you for all the great discussions about science and life in general. Pim, from the beginning it was clear to me that you are a very smart guy, but I did not realize how fun you could be until

the trip to Washington. I still can't stop laughing when I think about "hitting on girls with the Pokemon collection".

Gracia and Rita, thank you for arranging all the papers when I joined the department. Sharon, thank you for taking care of my reimbursements and for the help with the PhD forms.

Rik, Klazina, Tom, Ying, Jacopo, Alex, Raja, Lana, Mehdi, Ines, Kirby, Merel, Simone and Sara, thank you for the good atmosphere within the department and the constant positive attitude. Jason and Jenna, it has been really fun attending all the running events with you and I hope to see you this summer in Venice. Deep, thank you for all the nice time we had at the summer schools and for always being in a party mood. Ilya, thank you for the cakes and the "delicatessen" from Belgrade. Thank you to all the other members of the BME group for all the help and the nice moments shared throughout these years.

Come non ringraziare tutti gli amici che hanno contribuito a farmi sentire a casa anche se lontano dall'Italia. Fede e Ale, grazie per averci introdotto al giro degli Italiani, per le serate insieme ad Amersfoort e per lasciarci strapazzare Mattia ogni volta. Jessica e Thomas, grazie per le ospitate a Friburgo e a Palma, per le flammkuchen ed i gin tonic. Flavia e Simone, grazie per le prelibatissime cene a casa vostra e le serate di compagnia quando Enri era in Italia. Luca, grazie per esserti preso cura di Enri durante le uscite "only boys". Andrea ed Isa, siete sempre disponibili e gentili ed il vostro mix di spirito romano e valtellinese mette sempre di buon umore. Franco, grazie per averci accolto tutti questi anni nel tuo ristorante.

Nienke and Koen, you are truly the dearest Dutch friend we have. Thank you for all the fun we had together at the successful (and unsuccessful) music festivals.

Irma, Norbert and Vita, we are very glad to have you as our neighbors. You are so friendly and always willing to help.

Gabriele e Giulietta, grazie per le serate insieme e tutti i consigli sul lavoro.

Dimitri, Nella and Walter, thank you for making me feel part of the dental lab family.

Lejla, thank you for the help and the advices you gave me when I just moved to the Netherlands. Dragi Mirsade, Vido i Tomo, zahvaljujem vam na velikoj pomoći i podršci koju ste mi dali na početku ove moje avanture.

Anna e Franco, grazie per avermi accolto come una figlia fin da subito. Entrambi avete un cuore davvero grande e non potró mai dirvi grazie abbastanza per tutto quello che avete fatto e fate per me.

Mama, Tata, hvala sto ste mi dali korijen i krila: korijen da znam gdje mi je kuća, a krila da odletim i pokažem šta ste me naučili. Hvala vam na razumijevanju i bezgraničnoj ljubavi. Uvjek ste vjerovali u mene i moj uspejh i kad ni sama nisam.

Je, sorellina cara, senza il tuo sostegno e la tua grinta non sarei mai stata capace di prendere certe decisioni che poi si sono rivelate un successo. Grazie di esserci sempre e grazie a Marco che ti/ci sopporta.

Enrico, grazie per avermi seguito in questa avventura e per essermi sempre stato a fianco. Ci sono stati momenti difficili, ma con la tua calma ed il tuo sorriso tutto si è sempre risolto. Come dici tu "è una ruota che gira", prima o poi arriva la svolta che ti porta alla vittoria inaspettata come il Barcellona alla Champions contro il PSG. Grazie di esserti preso cura di me durante il periodo intenso di scrittura della tesi e grazie per tutti quei momenti di felice evasione: io e te, davanti ad un bicchiere di vino a fantasticare sui notri prossimi viaggi in giro per il mondo.

Sponsoring

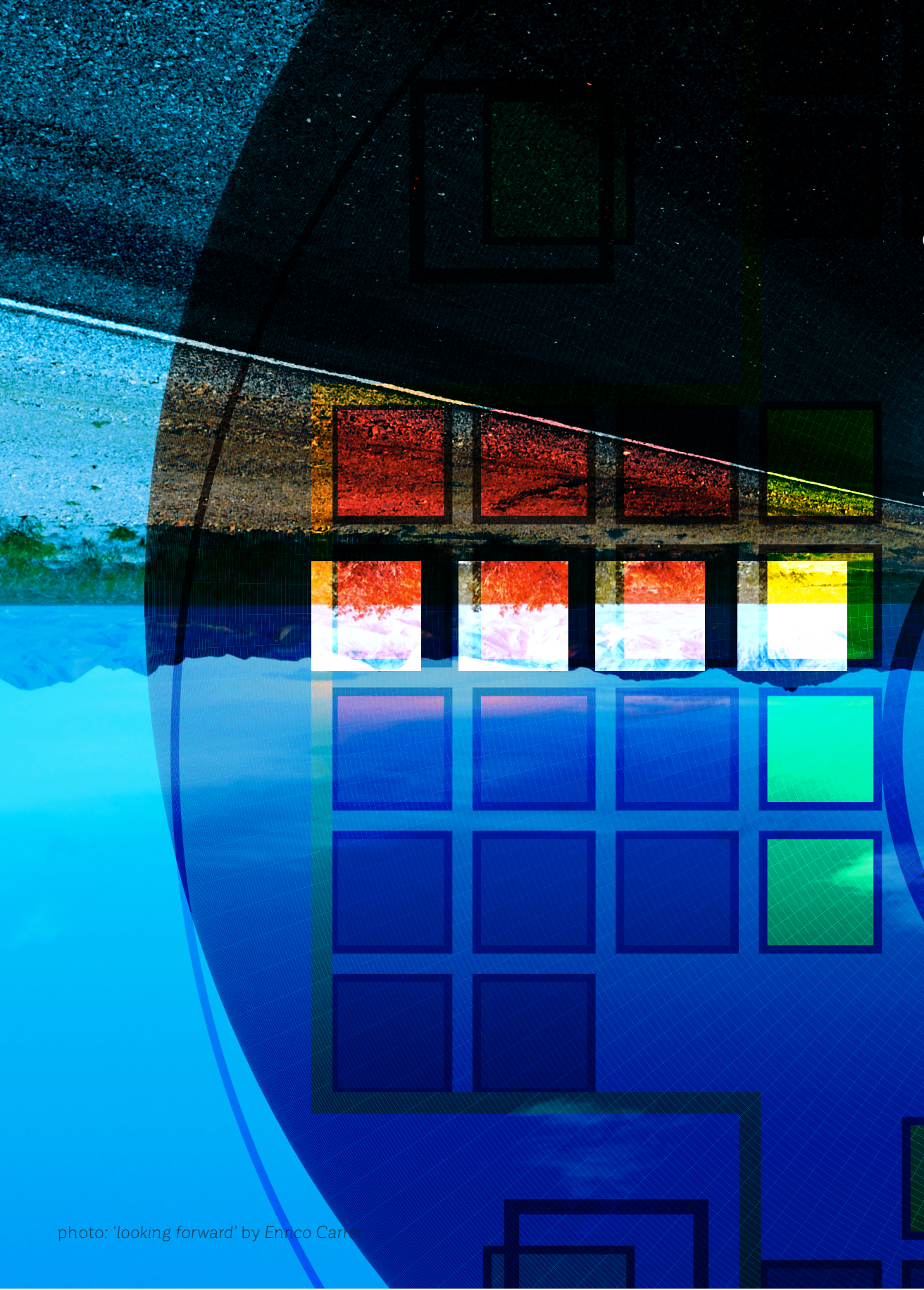

photo: *'looking forward'* by *Enrico Carrer*